Micro-Levitated Electromechanics

Ren, Yugang

Awarding institution:
King's College London

Micro-Levitated Electromechanics

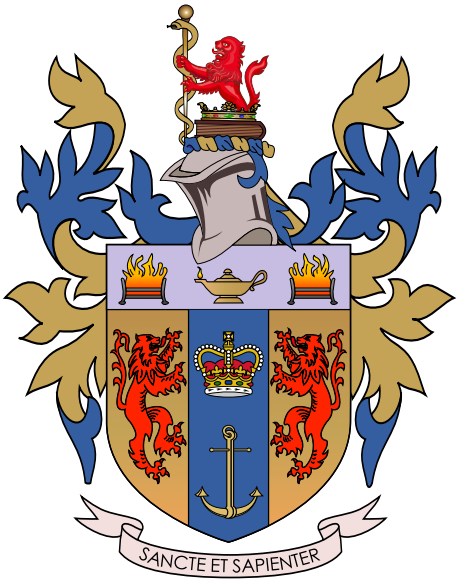

Yugang Ren

Supervisor: Prof. James Millen
Prof. Mark Green

The Department of Physics
King's College London

This dissertation is submitted for the degree of
Doctor of Philosophy

November 2023

Declaration

I hereby declare that except where specific reference is made to the work of others, the contents of this dissertation are original and have not been submitted in whole or in part for consideration for any other degree or qualification in this, or any other university. This dissertation is my own work and contains nothing which is the outcome of work done in collaboration with others, except as specified in the text and Acknowledgements. This dissertation contains fewer than 65,000 words including appendices, bibliography, footnotes, tables and equations and has fewer than 150 figures.

Yugang Ren
November 2023

List of Publications

Yugang Ren, Muddassar Rashid, *et al*. and James Millen. "Linear feedback cooling of an array of levitated microparticles." Manuscript in preparation.

Yugang Ren, Muddassar Rashid, *et al*. and James Millen. "Electric detection of particle motion." Manuscript in preparation.

Yugang Ren, Enrique Benedetto, Harry Borrill, Yelizaveta Savchuk, Katie O'Flynn, Muddassar Rashid, and James Millen. "Event-based imaging of levitated microparticles." Applied Physics Letters 121, 113506 (2022).

Acknowledgements

It is really a long journey to come to the end of my PhD study, during which I received not only obstacles and frustrations but also support and encouragements. I have profound appreciation to my esteemed doctoral supervisor Prof. James Millen. I still remember on the first day of my PhD study he told me "It's your PhD." This made me realize I was the owner of my PhD, but at the same time he has always provided me ample assistance and freedom requisite for my scholarly exploration. I also feel grateful for Dr. Muddassar Rashid who spent time discussing intricate technical challenges. I am thankful for my other colleagues within our group: Dr. Maryam Nikkhou, Dr. Katie O'Flynn, Dr. Yanhui Hu, James Sabin, Molly Message and Zhenan Chen, thank you all for your assistance and for creating a friendly work atmosphere.

I will express my gratitude to my fiancé, Dr. Xuyang Ren, thank you for your unwavering companionship. I know I am not good enough, but you always trust me I could be good enough. I will convey my appreciation to my dad Min Ren, my mom Jianqiong Feng and my brother Sheng Ren for all of their love to me. I am extremely fortunate to have you as my family.

Last but not least, to my valuable friends and colleagues, thank you for your collaboration and assistance which have greatly contributed to both my professional endeavors and personal well-being.

Abstract

Levitation of mesoscopic particles in high vacuum provides a promising platform to investigate nanoscale thermodynamics and the boundary between the classical and quantum worlds. By using a microfabricated Paul trap, charged particles with a wide range of sizes and materials can be coupled to the electrodes of the trap, enabling all-electrical levitation and cooling. With this two-way interaction between mesoscopic particles and the trapping electrodes, detection and control of particle motion can be realized. Through passive resistive cooling or active feedback cooling, high precision force detection will be achieved, and there is even the potential to reach the quantum regime. Simulations of the Paul trap using SIMION are conducted. An experimental microfabricated Paul trap has been designed and assembled. In this context, an innovative event-based imaging scheme is introduced to monitor the motion of microparticles, which enables the tracking of multiple particles at higher speed than conventional cameras. In consonance with this methodology, a Field Programmable-Gate-Array(FPGA)-based system is employed to output the detection signal from an event-based imaging scheme in real time. A cooling process based on cold damping is then carried out to reduce the temperature by 4 times at 2×10^{-2} mbar. A cooling phenomenon is evident in a specific mode during the cooling process of a pair of levitated particles. Furthermore, an electric detection of particle motion is also explored to get a minimum $(1.1 \pm 0.2) \times 10^{-12}$ A image current detection. Further improvement of the electric detection is suggested.

Table of contents

List of figures

List of tables

Nomenclature

Acronyms / Abbreviations

ACF	autocorrelation function
AC	alternating current
CD	contrast detector
CoM	centre of mass
DC	direct current
EBC	event-based camera
EBI	event-based imaging
FPGA	field programmable gate array
GTA	generic tracking algorithm
GWB	gain bandwidth product
LIAD	laser-induced acoustic desorption
LIA	lock-in amplifier
NV	nitrogen vacancy
PCB	printed-circuit-board
PSD	power spectral density
QPD	quadrant photodiode
ROI	region of interest
SNR	signal-to-noise ratio
VPP	peak-to-peak voltage

Chapter 1

Introduction

1.1 Mesoscopic particles in physics and technology

The control of mesoscopic particles is of great importance in many fields, such as the study of viruses [1], protein identification [2], astrophysics [3] and precise force detection [4]. Levitation allows the centre-of-mass (CoM) motion of particles to be isolated from the ambient environment. Confinement of levitated particles in harmonic potentials produces oscillators with a high-quality factor [5], which is essential for force sensitivity [6–8] and to prepare long coherence times in quantum experiments [9–11]. It is predicted that the motion of nanoparticles can be controlled at the quantum level, with the first demonstration of ground-state cooling in a levitated optomechanical system in 2020 [12], which will enable the study of macroscopic quantum physics and advance quantum technologies [13–16].

Optical traps are most commonly used for levitation, due to our ability to precisely control optical fields, and the relatively high trapping frequencies in the resulting harmonic potential, which avoids low-frequency (environmental) noise. The optical control of the mechanical motion of an object is known as "optomechanics", and the motion of optically trapped objects is therefore specifically referred to as "levitated optomechanics". However, optical traps are limited by shallow depths (about 1 eV [17] or 23200 K with $E = \frac{1}{2}k_BT$) leading to instability at low pressures where motional damping due to gas is no longer present. Low pressures are essential to achieve high-quality factor oscillations for sensitive force sensing and to avoid heating and decoherence when cooling particles towards the quantum ground state.

If an object oscillates with a frequency ω_0 , the momentum transfer from a photon to the object will add quanta $\hbar\omega_0$ to the oscillator's energy in a process called photon recoil heating [18]. Optical traps suffer from unavoidable heating due to photon recoil, which

will limit the coherence time in a quantum optomechanical system and force sensitivity at low pressures.

Here we are using a different trapping technology. Radiofrequency quadrupole traps, also known as Paul traps, will be utilized. Although optical traps have high trapping frequencies which can avoid environmental low-frequency noise, the stability of Paul traps (trap depths much greater than 1 keV [19], or 2.32×10^7 K) allows for straightforward operation in a high vacuum. Paul traps also have an extended trapping region to enable straightforward trap loading (about 1 cm^3 in general, as for the optical trap the trapping region is about $10\,\mu m^3$) [17]. Besides, the potential is extremely low noise due to the absence of photon recoil.

In this thesis, the investigation will center on the manipulation of levitated microparticles in vacuum. Compared to nanoparticles, microparticles have higher charge-to-square-root-of-mass ratio $Q/\sqrt{m}$ [20]. I will describe the work to trap charged microparticles in microfabricated Paul traps, detect the particle motion, conduct feedback cooling to the centre-of-mass motion of levitated particles and try to recover the particle motion by coupling to electronic circuitry. This will create a compact platform for the manipulation of charged microparticles, for applications in force sensing, studies in nanothermodynamics, and exploration of macroscopic quantum physics.

1.2 Mesoscopic particles in Paul traps

A Paul trap makes a quadrupole potential to capture charged particles. Because of Gauss' law, four poles cannot create a stable trapping region. A time-varying electric field is thus used to produce an approximate harmonic potential and a resultant 3D linear restoring force. Paul traps come in many geometries. Figure 1.1 shows a diagram of a linear Paul trap. The structure consists of four rods which confine charged particles along a line and two endcap electrodes for confinement in the remaining dimension. Two rods are connected to alternating current (AC) voltage and two rods are connected to direct current (DC) voltage. Endcap electrodes with a separation of d are usually connected to DC voltage as well.

Paul traps are mainly used in the study of atomic or sub-atomic particles [21–23]. In 1986, S. Arnold *et al.* used a Paul trap to capture microparticles containing organic laser dyes and acquire their fluorescence spectrum [24]. In 1991, H.Winter *et al.* set up a Paul trap to store a single anthracene dust particle for over two months [25]. In 2001, S. Schlemmer *et al.* trapped nanoparticles in a Paul trap and achieved an absolute mass determination of the charged particle [26].

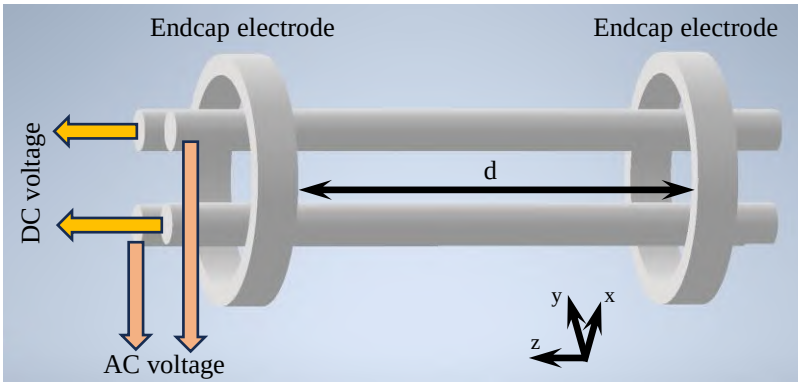

Fig. 1.1 Diagram of a Paul trap. In this structure, two rods are connected to AC voltage and two rods are connected to DC voltage. Two rings around the four rods are called endcap electrodes.

Because Nitrogen vacancy (NV) defect centres in diamond nanocrystals have optical and electronic properties which can be utilized in quantum optics and quantum information experiments [27, 28], some groups including O. Benson's group [29] in Humboldt Universität zu Berlin and G. Hétet's group [30, 31] in Laboratoire de Physique de l'ENS began to use Paul traps to levitate diamond particles. In 2014, O. Benson's group observed nitrogen vacancy fluorescence in a diamond cluster levitated in a linear ion trap [29]. In 2018, this group presented a linear, segmented Paul trap with electrodes printed on two printed-circuit-board (PCB) fiberglass boards to capture nanocrystals with a simple and inexpensive construction [32]. In 2020, G. Hétet's group observed a spin-dependent torque and spin-cooling of the motion of a trapped microdiamond, illustrating coupling between the macroscopic motion of the microdiamond and the microscopic spin contained within it [33].

It is also possible to levitate graphene nanoplatelets in a Paul trap. Since its discovery in 2004, graphene has received much attention for its unique behavior and potential applications. A Paul trap provides a good way to investigate graphene behaviors in isolation due to its large trapping region compared to optical traps. B. E. Kane's group at the University of Maryland carried out much work on graphene nanoplatelet levitation [34], cooling [35] and rotation frequency stabilization [36] in a Paul trap.

P. F. Barker's group at University College London use Paul traps to explore the dynamics of levitated nanoparticles. In 2014, they introduced a hybrid electro-optical trap, in which a Paul trap is used to trap 400 nm nanoparticles and a cavity is adopted to cool the center-of-mass temperature of by 100 times [37]. Via the hybrid electro-optical trap, this group introduced an experimental way to explore continuous spontaneous localization on the mesoscale by using a cavity-cooled, single-charged nanosphere levitated within a Paul trap [38]. This group proposed a super-resolution imaging technique to detect the charged

particle motion within a Paul trap [39] and characterized the frequency and temperature stability, charges and mass of levitated particles in Paul trap [40]. They measured the linewidth of the nano-oscillator to be $81 \pm 23\,\mu$Hz and placed new bounds on two wave-function collapse models [41]. They also compared the parametric and velocity feedback damping methods in Paul traps to show velocity damping is more resilient to imperfect experimental conditions [42].

T. E. Northup's group at the University of Innsbruck have conducted work on silica microparticles levitated in a Paul trap, with the ultimate aim of coupling their motion to atomic ions. In 2019, they demonstrated a technique which combines laser-induced acoustic desorption (LIAD) of nanoparticles from a metallic foil and temporal control of the Paul trap potential to load nanoparticles under ultra-high vacuum into a Paul trap. Experiments show the method has high efficiency, with more than 50 percent of loading events leading to capture in as short as a few milliseconds [43]. With this loading method, the group trapped a charged silica sphere with 300 nm diameter and used a cold cathode/Pirani combination gauge to control the electric charge of the particle, which can tune the oscillation frequency and enable a precise measurement of the mass [44]. They also proposed a self-interference method to detect the motion of levitated particles [45]. Meanwhile, they introduced laser cooling of the particle in Paul trap to cool the secular motion of a silica nanoparticle below 1 K [46]. Electrical feedback cooling is conducted to cool the particle motion to a few tens of mK from room temperature [17]. With ground state temperatures of a few μK there is still a long distance to cool the nanoparticles into the quantum regime, and this forms part of the motivation for this thesis.

Therefore, D. Goldwater *et al.* proposed an all-electrical levitation, detection and cooling scheme in a Paul trap for charged mesoscopic particles [20]. Such fully electrical control over the mechanical motion of a levitated object was dubbed "levitated electromechanics". Simulations show that the particle temperature reaches sub-Kelvin in a room temperature environment via all-electrical feedback cooling, with ground-state cooling possible in cryogenic environments. Later on, L. Martinetz *et al.* proved that a nanoparticle in a Paul trap can interface with the discrete level structure of a superconducting qubit. An all-electrical pulsed measurement scheme is introduced to generate and readout motional quantum superpositions and entanglement of levitated nanoparticles [47]. This thesis presents initial work that moves towards the achievement of all-electrical cooling of microparticles to sub-Kelvin temperatures.

1.3 Cooling and quantum physics in a Paul trap

In 1953, Wolfgang Paul *et al.* proposed a trap in which a time-dependent electrical field in the radio-frequency domain is used to confine atomic ions [48]. Because of this superb invention, Wolfgang Paul shared the Nobel Prize for the development of the ion trap technique. With this technique, studies of atomic ion and electron dynamics progressed with surprising speed [49, 50]. Laser cooling was first used to bring a trapped $^{198}Hg^{+}$ ion to the ground state of the harmonic potential provided by a Paul trap in 1989 by the National Institute of Standards and Technology (NIST) group [51]. With the advent of laser cooling techniques [52], Paul traps have enabled researchers to create high fidelity quantum entanglement [53], and this architecture is one of the most promising for creating practical quantum computers [54].

Laser cooling is not available for mesoscopic particles, due to their lack of closed optical transitions. Instead, cooling methods rely on radiation pressure, the optical dipole force, or exerting electrical forces on charged objects.

1.3.1 Cooling in optical traps

Cooling techniques for mesoscopic particles in optical traps include four types of methods, which are radiation pressure cooling, parametric feedback cooling, cold damping and optical cavity cooling. They have different principles and research developments.

Radiation pressure cooling

The instantaneous velocity of the particle can be calculated according to the position signals detected from system detectors. The velocity signal is then fed-back to modulate the optical power of one or more cooling beams. A scattering force opposite to the velocity direction is thus applied to the particle. T Li *et al.* cooled three centre-of-mass modes of a microsphere from room temperature to millikelvin temperatures using this method [55]. F Monteiro *et al.* demonstrated a cooling of the motion of a $10\,\mu$m-diameter sphere to $50 \pm 22\,\mu$K via minimizing the pointing noise of the trapping laser [56]. However, this cooling is only effective for relatively large particles, because the scattering force decreases rapidly with particle size and the laser pointing stability is hard to overcome.

Parametric feedback cooling

The method of parametric feedback cooling was used by J. Gieseler *et al.* to cool the centre-of-mass motion of an optically levitated nanoparticle by four orders of magnitude [57]. Unlike Radiation pressure cooling, only one laser is used for both trapping and

cooling. The motional signal of the particle is frequency doubled, with an appropriate phase shift, to generate the feedback signal. This signal is used to modulate the intensity of the trapping beam, so as the particle moves away from the centre of the trap, the optical trap is stiffened. Thus, the particle has to do additional work to climb the potential, whilst as the particle moves towards the centre of the trap, the optical trap is loosened ensuring less gain in energy. The cumulative consequence of this is that the particle loses energy and its motion is cooled. With this method, V. Jain *et al*. realized the centre-of-mass temperature to be $T_{\mathrm{CoM}} = (450.5 \pm 33.1)\,\mu\mathrm{K}$ [18]. Then this was later improved to $145\,\mu\mathrm{K}$ [58]. This technique is good for small particles, but becomes challenging at low particle temperatures, since the non-linear nature of the method requires a feedback gain proportional to the amplitude of the particle motion.

Cold damping

In cold damping, the positional information of a charged particle is collected and then used to generate a feedback signal proportional to the particle's velocity, which is applied via a Coulomb force to the charged particle. F. Tebbenjohanns *et al*. used cold damping to cool an optically levitated nanoparticle from room temperature to $100\,\mu\mathrm{K}$ at a pressure of 10^{-8} mbar [59]. Based on the method, a silica sphere with a diameter of 136 nm is cooled close enough to the ground state (a phonon occupation number of $n_{\mathrm{phonon}} = 4$) such that quantum effects are evident in the particle motion [60] and then they cool a nanoparticle to an average occupancy of 0.65 ± 0.43 [14]. G. P. Conangla *et al*. introduced a machine learning algorithm to optimize cold damping feedback gains and achieved cooling times a factor of 10–600 faster [10]. More elaborate feedback schemes, such as a Kalman filter, can also be used to cool to the quantum state with a mean occupation of 0.56 ± 0.02 [61].

Optical cavity cooling

Optical cavity cooling includes cavity-assisted resolved-sideband cooling and cavity cooling via coherent scattering. In cavity-assisted resolved-sideband cooling, the motion of a particle is coupled to an optical cavity and will cause the cavity frequency to shift. The cavity field itself can be used to levitate the particle. This generates sidebands at the motional frequency of the particle, corresponding to the oscillator (levitated nanoparticle) either losing or gaining energy. The cavity resonance makes it possible to preferentially scatter into one of these sidebands, cooling the particle [62]. Using this method, in a hybrid electro-optical trap, J. Millen *et al*. cooled a nanoparticle to 0.3 K [37, 63]. In the coherent scattering technique, the particle is levitated in an optical trap within, but separate to, the optical cavity field. The scattering of light from the optical trap by the particle is used to drive the cavity, enabling a strong exchange of energy between the particle and the cavity

field. The scheme was introduced by U. Delić *et al* [64]. In 2020, they realized the cooling of a nanoparticle, which comprises 10^8 atoms, to ground state of an optical potential in a room temperature environment [12].

In summary, Figure 1.2 is listed to show the latest research results with the four cooling methods.

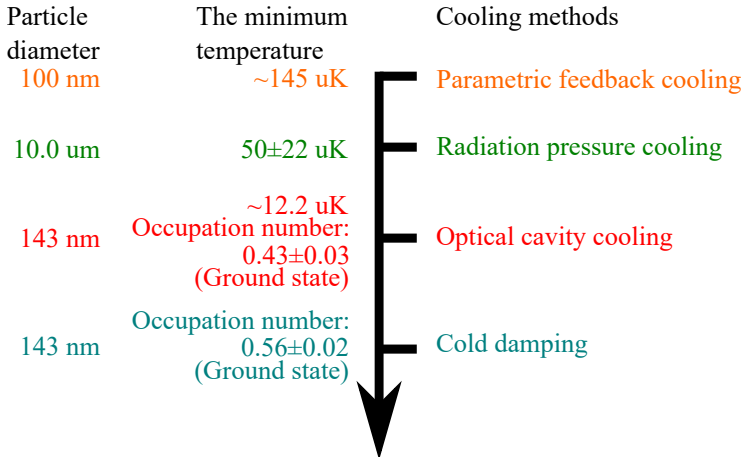

Fig. 1.2 Summary of cooling development for mesoscopic particles in optical traps. The left two column values indicate the particle diameter and related minimum centre-of-mass temperatures based on the four types of cooling methods labelled on the right column. The lowest temperature value based on cold damping is not given in the publication but an occupation number is listed to indicate that the cooled particle reaches the ground state. The relationship between the centre-of-mass temperature and the mean phonon occupation number is $k_B T_{\mathrm{CoM}} = (n_{\mathrm{phonon}} + \frac{1}{2})\hbar\omega_0$.

1.3.2 Cooling in Paul traps based on optical detection

Here, three cooling methods will be introduced: optical feedback cooling, cavity cooling and cold damping.

Optical feedback cooling

This technique is identical to the parametric feedback cooling mentioned above, except the levitating field is now the Paul trap and feedback signal is to modulate the amplitude of provided AC voltage to the Paul trap. R. Quidant *et al.* levitated a nanodiamond hosting a single nitrogen-vacancy center in a Paul trap and optically measured the nanodiamond's center-of-mass motion. Feedback cooling realized temperature reduction by a factor of 4 at 5×10^{-1} mbar to enbale the interrogating and characterizing the emitter response [65, 66]. Similarly, P. Nagornykh *et al.* cooled graphene nanoplatelets levitated in a quadrupole ion trap to 20 K at 4×10^{-7} Torr and cooling of motion along three axes was observed [35].

Cavity cooling

J. Millen *et al*. were the first to propose cavity cooling for charged particles in Paul trap with the goal to investigate the macroscopic quantum behavior. This method removed the need for the optical field to both levitate and cool the particle, and avoids instabilities at low pressures for optical traps. They realized a factor of 100 reduction in temperature for 400 nm diameter silica spheres [37]. Later on, this group demonstrated a greater than 1000-fold reduction in temperature and reached about 0.3 K at steady state with this method [63].

Cold damping

With this technique, T. E. Northup *et al*. recently used optical detection to generate electrical feedback cooling, as in the cases described above. Three motional modes of a charged nanoparticle in Paul trap are cooled to temperatures of a few mK [17]. Y. Minowa *et al*. then demonstrated a camera-based feedback cooling scheme to cool a charged nanoparticle to minimum temperature 5.8 K at 8×10^{-5} mbar [67].

All electric cooling

When the endcap electrodes are connected to an RLC circuit, the motion of the levitated charged particle will induce an image current to the circuit. The current in the circuit will dissipate and damp the motion of the particle, which is called passive resistive cooling. Resistive cooling can pre-cool massive particles of which the initial energy is far above room temperature due to their method of injection into the trap. If we can detect the particle motion via the induced current, it is possible to feedback the signal onto the endcap electrodes to control the dynamics of the charged particles, which is called active feedback cooling. Compared to optical feedback cooling, cavity cooling and cold damping via optical detection, an all electrical cooling can avoid motional heating due to the scattering of photons and will enable both passive and active cooling of mesoscopic particles towards the quantum regime by coupling their motion to an RLC circuit [20]. Such methods have been used to cool electrons and protons in Penning traps [68–70] but have not been explored at mesoscopic scale.

In conclusion, we have Figure 1.3 below which indicates the recent research work on Paul trap cooling for mesoscopic particles.

1.3.3 Structure of this thesis

This thesis will introduce Micro-Levitated Electromechanics. In Chapter 2, the Paul trap theories and simulations of two Paul traps (a Macro-Paul trap and a Micro-Paul trap)

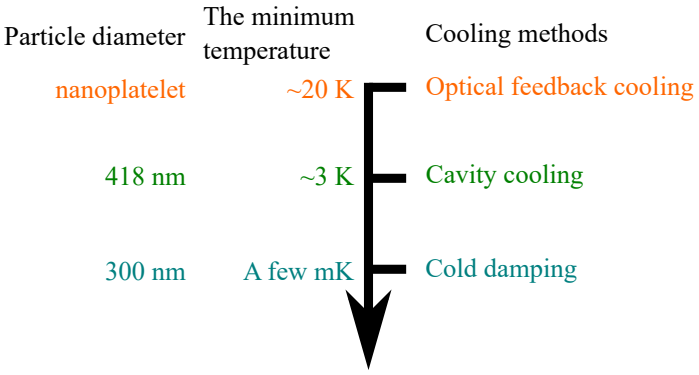

Fig. 1.3 Summary of cooling development for mesoscopic particles in Paul traps. The left two column values indicate the particle diameter and related minimum centre-of-mass temperatures based on the three types of cooling methods labelled on the right column. The particle size value based on optical feedback cooling is not listed but a nanoplatelet structure is mentioned in the publication. Phonon numbers are not given since these temperatures are far from quantum state.

based on SIMION are firstly introduced. Experimental Micro-Paul trap system is designed and assembled. In chapter 3, an event-based imaging technique is proposed to detect the motion of levitated microparticles. This method offers the prospect of simultaneous motion tracking for both individual and multiple particles, maintaining a high bandwidth. In chapter 4, a linear feedback cooling (or cold damping) according to the imaging detection is carried out to cool the centre-of-mass motion of trapped microparticles. Chapter 5 explains an electric detection method of particle motion and Chapter 6 gives a summary of the work throughout the thesis and outlines the next steps of future work.

Chapter 2

Design of Paul trap and Micro-Paul trap

In this chapter, we aim to design and assemble a Micro-Paul trap. To reach the goal, Paul trap theory, simulations and the Micro-Paul trap setup are introduced. Techniques of particle loading, motion detection and calibration are also supplemented.

2.1 Paul trap theory

2.1.1 Equations of motion

The motion of a charged particle in the quadrupole field can be expressed by the solutions to the Mathieu equation [71]. According to Mathieu's mathematical description, these solutions are separated into regions of stability and instability, which can be used to define the trajectories of captured particles to be stable or unstable. Assume two dimensionless stability parameters a_i and q_i, the Mathieu equation can be written as

$$\frac{d^2u_i}{d\xi^2} + [a_i - 2q_i\cos(2\xi)]\,u_i = 0, \tag{2.1}$$

where u_i is the particle position along one of the three axes and i represents x, y and z because the motion of the three axes is uncoupled in the approximately harmonic potential created by the quadrupole field. ξ is a dimensionless parameter and $\xi = \Omega_{RF}t/2$. Ω_{RF} with unit rad/s is the frequency of AC voltage applied to the electrodes of the Paul trap. So we can obtain

$$\frac{d^2u_i}{dt^2} = \frac{\Omega_{RF}^2}{4}\frac{d^2u_i}{d\xi^2}. \tag{2.2}$$

Substituting Equation 2.2 into Equation 2.1 and multiplying by the particle mass, the expression is shown as

$$m\frac{d^2u_i}{dt^2}+m\frac{{\Omega_{RF}}^2}{4}\left[a_i-2q_i\cos\left(\Omega_{RF}t\right)\right]u_i=0. \tag{2.3}$$

The first term of the left-hand side is the force working on the charged particle. Take a force in z axis F_z for example, the force is

$$F_z=m\frac{d^2z}{dt^2}=-Q\frac{dV}{dz}, \tag{2.4}$$

here Q is the charge of the particle, z is the particle position along z axis, V is the pseudopotential at one point in this field. The expressions of the forces along x and y axes are similar to Equation 2.4. For a point (x,y,z) in the quadrupole potential, the pseudopotential can be described as [72]

$$V(x,y,z)=\frac{V_{RF}\cos\left(\Omega_{RF}t\right)}{2r^2}\left(\alpha_x x^2+\alpha_y y^2+\alpha_z z^2\right)+\frac{4U_{DC}}{d^2}\left(\beta_x x^2+\beta_y y^2+\beta_z z^2\right), \tag{2.5}$$

where $V(x,y,z)$ is the pseudopotential at the point (x,y,z) in the electric field, V_{RF} is the amplitude of the added AC voltage to the Paul trap, α_i and β_i ($i=\{x,y,z\}$) are six weighting constants (or geometric factors) for the x, y and z coordinates, r represents the distance from trap centre to the surface of the electrodes, U_{DC} is the DC voltage of the two endcap electrodes and d indicates the separation between the two endcap electrodes. By substituting Equation 2.5 to Equation 2.4, the motion of the particle along z axis is given

$$m\frac{d^2z}{dt^2}+\left[\frac{8QU_{DC}\beta_z}{d^2}+\frac{\alpha_z QV_{RF}\cos\left(\Omega_{RF}t\right)}{r^2}\right]z=0. \tag{2.6}$$

Comparing Equation 2.6 and Equation 2.3, a_z and q_z are as follows

$$a_z=\frac{32QU_{DC}\beta_z}{md^2\Omega_{RF}^2},\quad q_z=\frac{-2QV_{RF}\alpha_z}{mr^2\Omega_{RF}^2}. \tag{2.7}$$

Similarly, the expressions for a_x, a_y, q_x, q_y are

$$a_x=\frac{32QU_{DC}\beta_x}{md^2\Omega_{RF}^2},\quad q_x=\frac{-2QV_{RF}\alpha_x}{mr^2\Omega_{RF}^2}. \tag{2.8}$$

$$a_y=\frac{32QU_{DC}\beta_y}{md^2\Omega_{RF}^2},\quad q_y=\frac{-2QV_{RF}\alpha_y}{mr^2\Omega_{RF}^2}. \tag{2.9}$$

The values of a_i and q_i must be chosen so that Equation 2.1 has stable solutions. Usually when we set $U_{DC}=0\,\mathrm{V}$, $a_i=0$ and q_i has to be below 0.91 for stable trapping.

The frequencies of the particle motion are given by [50]

$$\omega_i = \frac{1}{2}\Omega_{RF}\sqrt{a_i + \frac{1}{2}{q_i}^2}. \tag{2.10}$$

Therefore, the expressions of frequencies in three axes can be achieved as

$$\omega_x = \sqrt{\left(\frac{Q}{m}\right)^2 \frac{V_{RF}^2}{2\Omega_{RF}^2 r^4}\alpha_x^2 + \frac{8QU_{DC}\beta_x}{md^2}}, \tag{2.11}$$

$$\omega_y = \sqrt{\left(\frac{Q}{m}\right)^2 \frac{V_{RF}^2}{2\Omega_{RF}^2 r^4}\alpha_y^2 + \frac{8QU_{DC}\beta_y}{md^2}}, \tag{2.12}$$

$$\omega_z = \sqrt{\left(\frac{Q}{m}\right)^2 \frac{V_{RF}^2}{2\Omega_{RF}^2 r^4}\alpha_z^2 + \frac{8QU_{DC}\beta_z}{md^2}}. \tag{2.13}$$

where the unit of ω_i ($i = \{x, y, z\}$) is rad/s.

2.1.2 Power spectral density

Because levitated particles are oscillators, a position autocorrelation function (ACF) is a useful tool to analyze their motion. Take the one-dimensional motion along z axis as an example, we get

$$\langle z(t)z(0)\rangle = \frac{k_B T_{\mathrm{CoM}}}{m\omega_z^2} - \frac{1}{2}{\sigma_z}^2(t), \tag{2.14}$$

where $z(t)$ is the particle position along the z axis, $z(0)$ is the initial position, k_B is the Boltzmann constant, ${\sigma_z}^2(t)$ is the position variance and T_{CoM} is the centre-of-mass temperature.

The power spectral density (PSD) is the Fourier transform of the position ACF $S_{zz}(\omega) = \frac{1}{2\pi}\int_{-\infty}^{\infty}\langle z(t)z(0)\rangle e^{-i\omega t}dt$, which provides a way to study the motion in the frequency domain and the expression of the PSD is

$$S_{zz}(\omega) = \frac{2k_B T_{\mathrm{CoM}}\Gamma_0/m}{\left(\omega^2 - {\omega_z}^2\right)^2 + {\Gamma_0}^2\omega^2}, \tag{2.15}$$

where Γ_0 is the damping rate determined by random collisions between the particle and ambient gas. Via obtaining the $S_{zz}(\omega)$ from experimental data and fitting it with the Equation 2.15, the values of T_{CoM}, Γ_0 and ω_z can be extracted.

Table 2.1 The fitting results of potential distributions from Macro-Paul trap.

κ_{1x}	κ_{2x}	κ_{3x}	κ_{1y}	κ_{2y}	κ_{3y}	κ_{1z}	κ_{2z}	κ_{3z}
63.6	0.1	32.2	102.5	0.1	32.2	-126.7	1.7×10^{-4}	32.1

2.2 Paul trap simulation with SIMION

SIMION is a software package which is primarily used to calculate the 2D/3D electric field distribution and the trajectories of charged particles within these fields, based on finite difference. In SIMION, geometry structures and voltages of electrodes are user-defined and the initial state of particles can also be given.

We have two Paul traps in the lab, a "Macro-trap" which has cm scale arrangement of AC electrodes to explore the dynamics of levitated microparticles in vacuum, and a "Micro-trap" has few-mm scale arrangement of AC electrodes to couple charged microparticle motion to nearby electrodes. Simulations of the Macro-trap were carried out to both verify the validity of the simulations, and to provide useful geometric information for ongoing experiments in that system. The simulations could then be confidently be applied to predict particle behaviour in the Micro-trap.

2.2.1 Simulation of the Macro-Paul trap

Figure 2.1 shows the geometry of the Macro-Paul trap electrodes. The structure has four electrode rods with 3 mm diameter (the distance from the centre of the trap to the surface of the rods is $r = 3.45$ mm), in which two opposite electrodes are connected with the AC voltage of frequency Ω_{RF} and amplitude V_{RF}, with the values matching experiment, and the remaining two are connected to DC voltage. Two endcap electrodes separated by 1 mm ($d = 1$ mm) have the DC voltage ($U_{DC} = -4$ V) and the two shields around the endcap electrodes are grounded to minimize the impact of external electric fields.

From SIMION, static electric potential distributions at $t = 0$ s, along three axes can be obtained, which are depicted in Figure 2.2. It appears that the potential around the centre of the trapping region is parabolic in all three axes, which would lead to a harmonic potential, but we must characterize how close to parabolic the potential actually is. A strongly non-harmonic potential would lead to a sharing of energy between different motional modes.

To test harmonicity, we look into the potentials in a central 200-micron cube. In the experiment, a trapped particle occupies a space much smaller than this ($\leq 20\mu$m). Here each grid cell of the electric field is $50\,\mu$m, so the spatial resolution is $50\,\mu$m. We use a quadratic equation $V = \kappa_{1i}{u_i}^2 + \kappa_{2i}u_i + \kappa_{3i}$ to fit the potential distribution, where V is the potential and i can be x, y and z with all lengths in mm. Table 2.1 lists the fitting results.

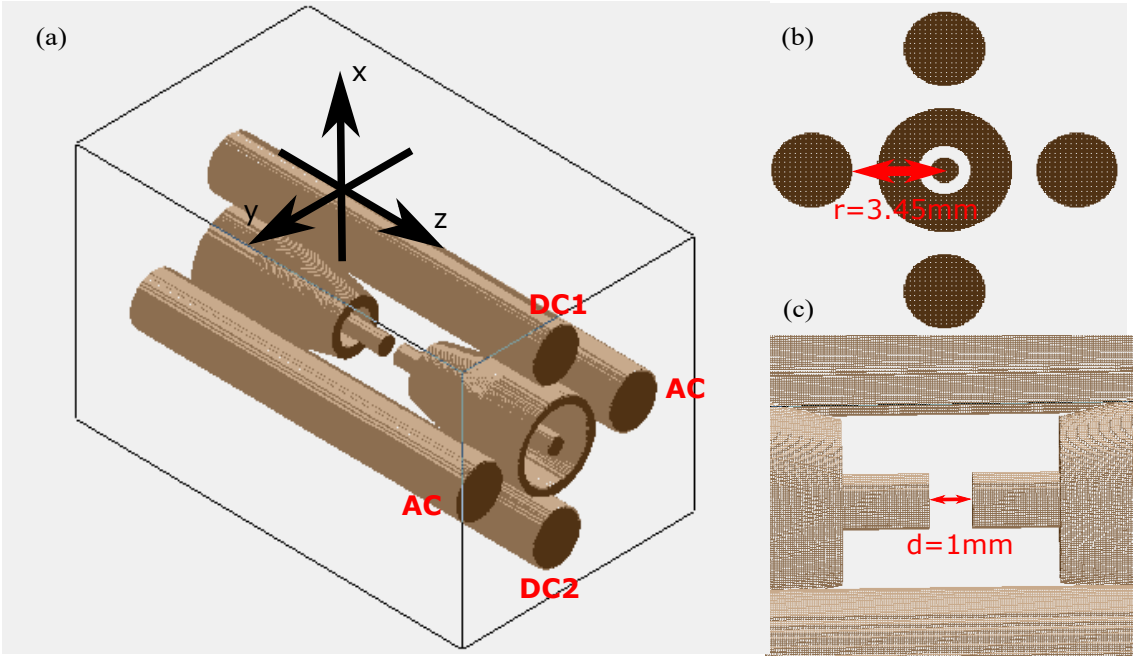

Fig. 2.1 The structure of the Macro-Paul trap. It consists of four rods and two endcap electrodes forming the quadrupole potential. The endcap electrodes are isolated with grounded shields to prevent them from picking up the AC voltage.

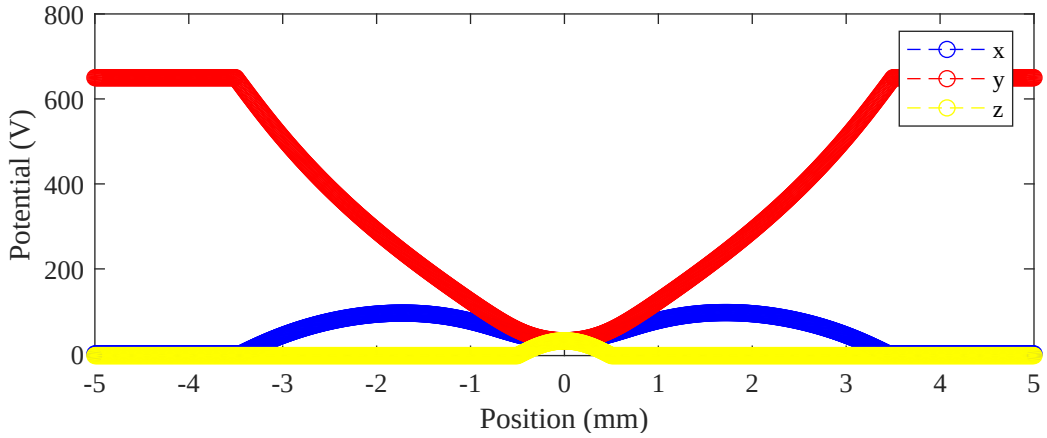

Fig. 2.2 Potential distributions along x, y and z axis in Macro-Paul trap, which are indicated with blue, red and yellow dots respectively. The taken data is limited in a central 5 mm-cube region.

Compared with κ_{1i}, κ_{2i} $(i = x, y, z)$ can be negligible, which means the distributions of potentials in three directions are harmonic. Ignoring the values of κ_{2i} and using $V = \kappa_{1i}u_i{}^2 + \kappa_{3i}$ to fit the potentials, we get the fitting results shown in Figure 2.3. The curve direction in Figure 2.3(c) is different from the direction in Figure 2.3(a) and Figure 2.3(b)), an illustration of Gauss' Law, showing why we need to use time varying electrical fields.

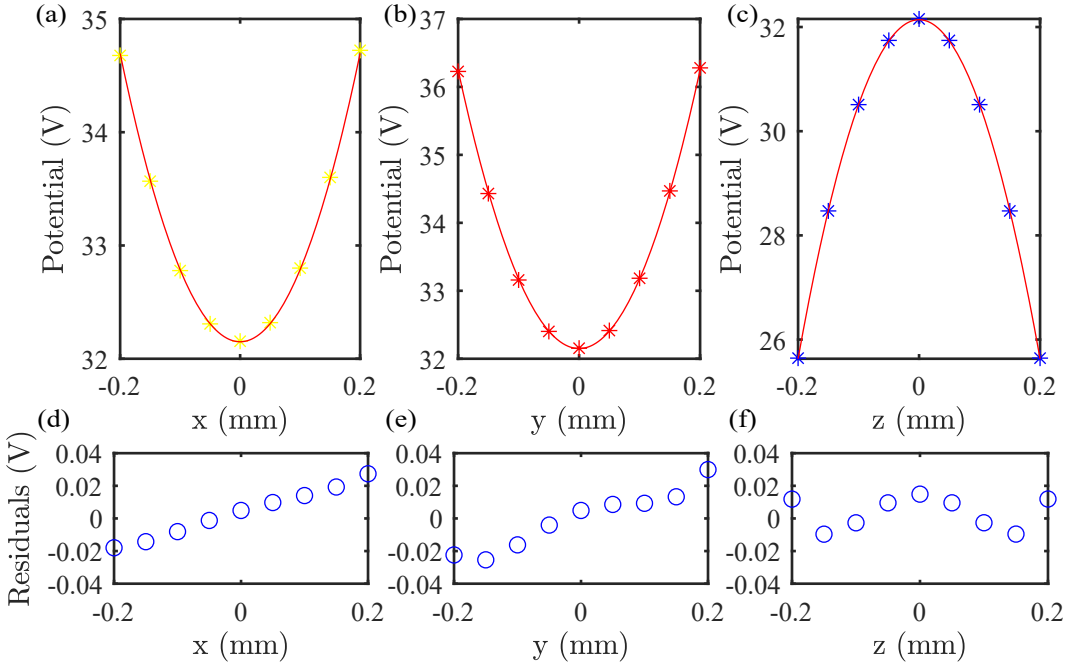

Fig. 2.3 Potential distribution fittings and potential residuals along three axes. (a) Potential distribution fittings along x axis. (b) Potential distribution fittings along y axis. (c) Potential distribution fittings along z axis. (d) Potential residuals along x axis. (e) Potential residuals along y axis. (f) Potential residuals along z axis.The fittings are limited in a central 200-micron cube. Fitting curves are indicated with red lines, matching well with potential data dots.

Table 2.2 Geometric factors obtained from SIMION numerical simulation of our Paul Trap.

	x	y	z
α	$(22.79 \pm 0.02) \times 10^{-1}$	3.70 ± 0.01	-5.86 ± 0.02
β	$(-8.89 \pm 0.02) \times 10^{-2}$	$(-8.89 \pm 0.02) \times 10^{-2}$	$(17.42 \pm 0.07) \times 10^{-2}$

According to Equation 2.10, in order to obtain the oscillation frequencies of the charged particle, six weighting constants (or geometric factors) α_i and β_i ($i = \{x, y, z\}$) need to be calculated firstly. Via setting the DC voltage to be $U_{DC} = 0$ V, the AC voltage to be $V_{RF}\cos(\Omega_{RF}) = 650\,\mathrm{V}$ and using Equation 2.5 to fit the potential, the values of α_i are obtained. Then replace the AC voltage $V_{RF}\cos(\Omega_{RF}t) = 0\,\mathrm{V}$ and set the DC voltage $U_{DC} = -4\,\mathrm{V}$ to obtain the values of β_i. Table 2.2 lists the fitting results and all the weighting constants are dimensionless. The values of β_x and β_y are equal which is reasonable due to the symmetry of the DC electric field.

In the experiment, silica particles of diameter 5μm (mass $m = 8.02 \times 10^{13}$ amu) and charge $q = 16000\,\mathrm{e}$ are trapped. The charge of the levitated particle is derived from detecting particle motion frequency and is not controllable. When the DC voltage $U_{DC} = -4\,\mathrm{V}$ and the AC voltage with frequency $\Omega_{RF} = 2\pi \times 800\,\mathrm{rad\,s^{-1}}$ and amplitude $V_{RF} =$

650 V, the expected oscillation frequencies with unit rad/s are calculated via Equation 2.10. Divided by 2π, the frequencies with unit Hz are obtained, which is expressed in the following

$$f_x = 38.6 \text{ Hz}, \tag{2.16}$$

$$f_y = 78.8 \text{ Hz}, \tag{2.17}$$

$$f_z = 147.3 \text{ Hz}. \tag{2.18}$$

Meanwhile, the trajectories of the trapped particle are able to be exported from SIMION. Figure 2.4 shows the power spectral densities of a trapped particle position which indicate the particle mechanical frequencies in the three axes are $f_x' = 40.0$ Hz, $f_y' = 80.9$ Hz and $f_z' = 157.6$ Hz.

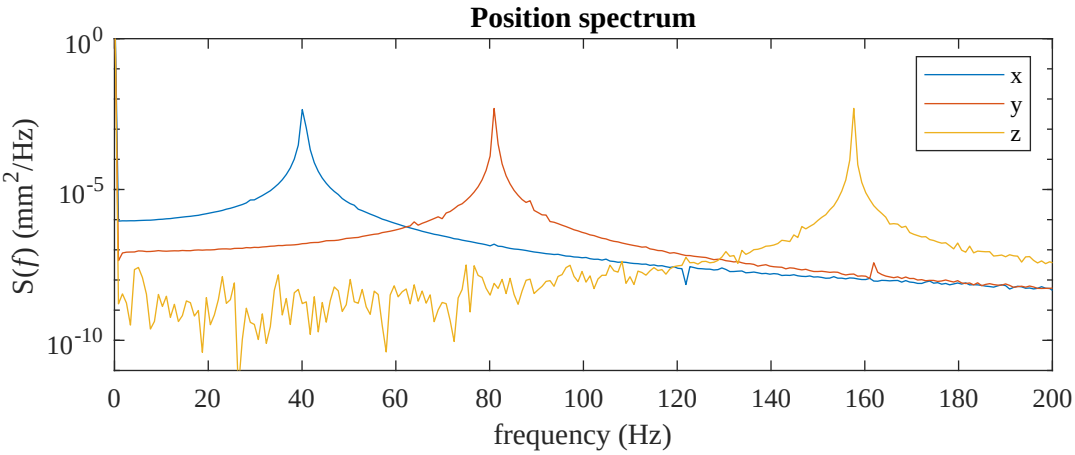

Fig. 2.4 The PSDs of a levitated particle position along three axes from SIMION simulation. The blue, red and yellow curves correspond to the PSDs of the levitated particle motion along x, y and z axes. From the obtained PSDs, we can the oscillation frequencies are $f_x' = 40.0$ Hz, $f_y' = 80.9$ Hz and $f_z' = 157.6$ Hz.

Two calculation results from Equation 2.10 and SIMION give the following relative errors:

$$\left|\frac{f_x' - f_x}{f_x}\right| = \left|\frac{40.0 - 38.6}{38.6}\right| = 3.6\%, \tag{2.19}$$

$$\left|\frac{f_y' - f_y}{f_y}\right| = \left|\frac{80.9 - 78.8}{78.8}\right| = 2.7\%, \tag{2.20}$$

$$\left|\frac{f_z' - f_z}{f_z}\right| = \left|\frac{157.6 - 147.3}{147.3}\right| = 7.0\%. \tag{2.21}$$

Table 2.3 The fitting results of potential distributions from Micro-Paul trap.

κ_{1x}	κ_{2x}	κ_{3x}	κ_{1y}	κ_{2y}	κ_{3y}	κ_{1z}	κ_{2z}	κ_{3z}
63.9	1.0	96.3	349.0	-2.3×10^{-2}	96.3	-487.1	9.4×10^{-4}	96.4

The two results are very close to each other with all relative errors below 10%, which gives us confidence in the next simulation with the Micro-Paul trap based on SIMION. Because the analytic model (Equation 2.10) can never fully capture the geometry of the Paul trap, there is still a difference between the two results.

To summarise, we have used SIMION to numerically simulate the motion of a charged particle in the Macro-Paul trap, yielding frequencies f_i', and compared these to the theoretical model which yields frequencies f_i. The agreement means we can both trust our SIMION simulation, and also can use the simple theoretical model to make predictions in different parameter regimes.

2.2.2 Simulation of the Micro-Paul trap

Compared to the Macro-Paul trap, the distances between the electrodes are greatly reduced so that the charged particle can be strongly coupled to the trap electrodes. The Micro-Paul trap will provide a two-way interaction between mesoscopic particles and the trapping electrodes. By adjusting electrode voltages, the motion of the particle is controlled. Through the current induced in the electrodes by the motion of the particle, the motion of the particle is measured (More information can be found in Chapter 5).

Figure 2.5 shows the geometry of the Micro-Paul trap structure. The trap has four electrode rods (the distance from the centre of the trap to the surface of the rods is $r = 1.15$ mm), in which two opposite electrodes are connected with the AC voltage of frequency Ω_{RF} and amplitude V_{RF} and the other two are connected to DC voltage. Two endcap electrodes separated by 0.8 mm ($d = 0.8$ mm) have the DC voltage ($U_{DC} = 0.1$ V).

With a similar method, we can extract the static electric potential distribution along three axes from a SIMION simulation at $t = 0$ s. Figure 2.6 gives the potential distributions of the three directions. It can be observed that the central potential distribution is parabolic in all three axes leading to a harmonic potential. To further characterize the harmonicity of the potential distribution, a fitting based on a quadratic equation $V = \kappa_{1i}{u_i}^2 + \kappa_{2i}u_i + \kappa_{3i}$ is carried out. Here V is the potential and i can be x, y and z with all lengths in mm. Table 2.3 depicts the fitting results of the potential distributions.

From Table 2.3, we can notice that in comparison to κ_{1i}, κ_{2i} ($i = x, y, z$) can be negligible indicating the distributions of potentials in three directions are harmonic. If we ignore the values of κ_{2i} and adopt $V = \kappa_{1i}{u_i}^2 + \kappa_{3i}$ to fit the potentials, fitting results of the three

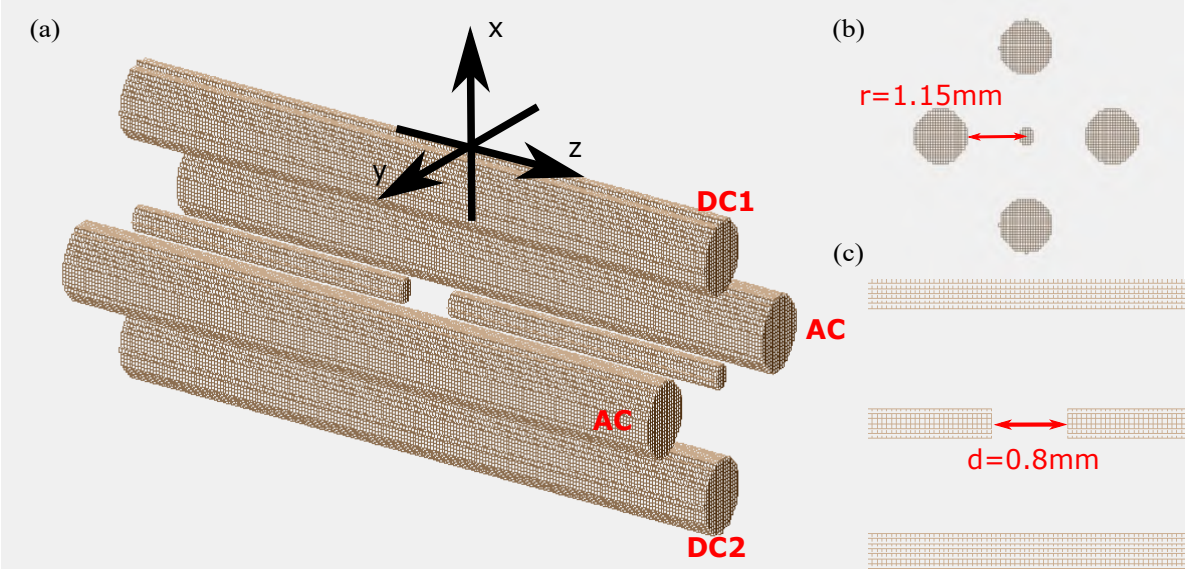

Fig. 2.5 The structure of the Micro-Paul trap. Similar to Macro-Paul trap, it consists of four rods and two endcap electrodes. The endcap electrodes are 0.8 mm separated.

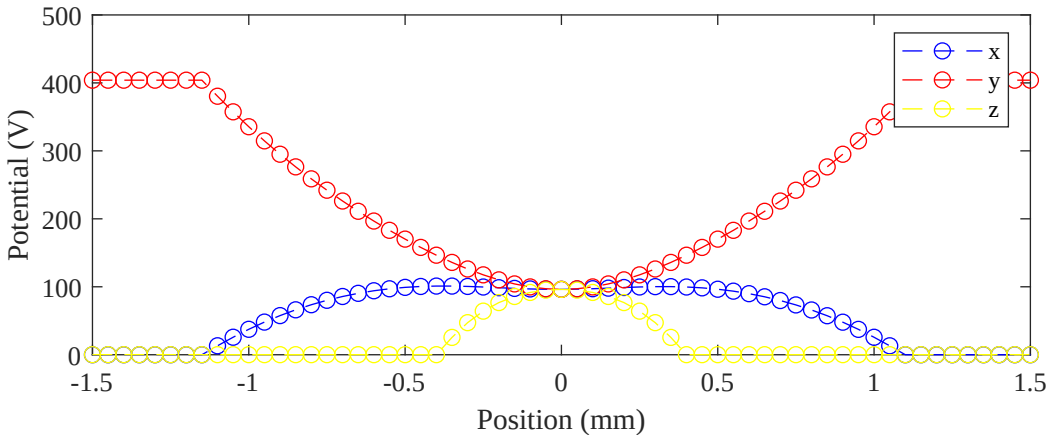

Fig. 2.6 Potential distributions of Micro-Paul trap along x, y and z axis in Micro-Paul trap, which are indicated with blue, red and yellow dots respectively. The taken data is limited in a central 1.5 mm-cube region.

direction can be shown in Figure 2.7. The curve direction in Figure 2.7(c) is also different from the direction in Figure 2.3(a) and Figure 2.3(b)).

We then set the DC voltage to be $U_{DC} = 0$ V, the AC voltage to be $V_{RF}\cos(\Omega_{RF}t) = 404$ V and using Equation 2.5 to fit the potential, the values of α_i are acquired. Then, we replace the AC voltage $V_{RF}\cos(\Omega_{RF}t) = 0$ V and set the DC voltage $U_{DC} = 1$ V to obtain the values of β_i. Table 2.4 lists the fitting results and all the Geometric factors are dimensionless. The values of β_x and β_y are still the same to each other which is reasonable due to the symmetry of the DC electric field.

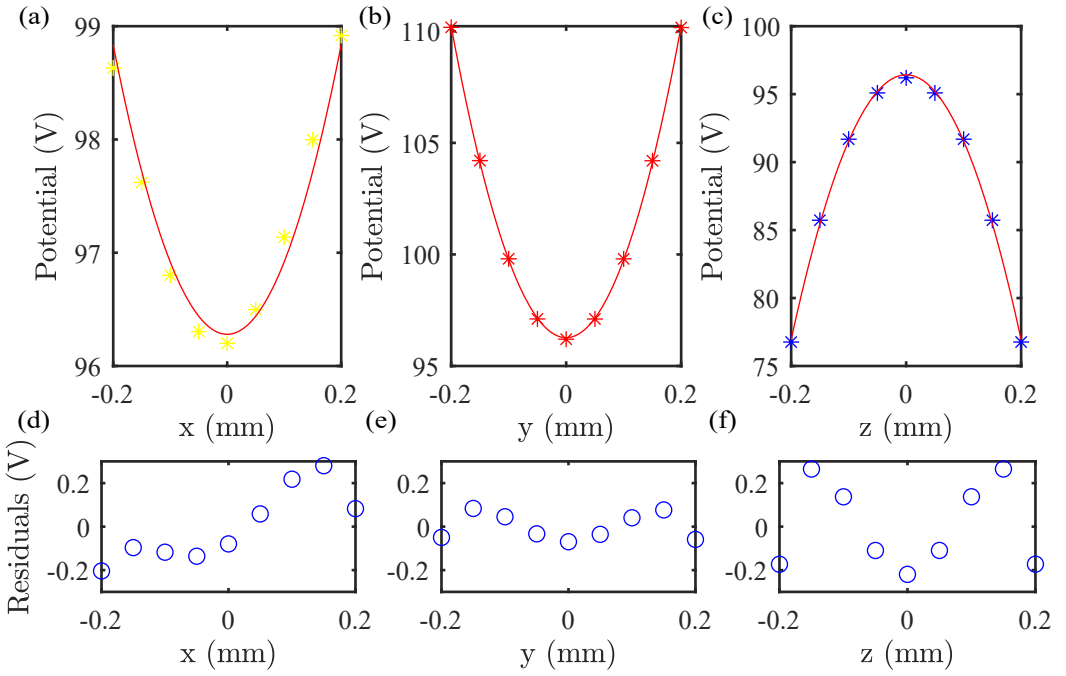

Fig. 2.7 Potential distribution fittings and potential residuals of Micro-Paul trap along three axes. (a) Potential distribution fittings along x axis. (b) Potential distribution fittings along y axis. (c) Potential distribution fittings along z axis. (d) Potential residuals along x axis. (e) Potential residuals along y axis. (f) Potential residuals along z axis. The fittings are limited in a central 200-micron cube. Fitting curves are indicated with red lines, matching well with potential data dots.

Then we begin to set properties of a trapped particle which has mass $m = 8.02 \times 10^{13}$ amu and charge $q = 4300$ e. In general, the charge of trapped particles usually range from 2×10^3 e to 2×10^4 e in our experiments. The related voltage setting are with DC voltage $U_{DC} = 0.1$ V and the AC voltage with frequency $\Omega_{RF} = 2\pi \times 1100\,\mathrm{rad\,s^{-1}}$ and amplitude $V_{RF} = 404$ V. According to Equation 2.10, three oscillation motion frequencies can be obtained

$$f_x = 7.9 \text{ Hz}, \tag{2.22}$$

$$f_y = 57.3 \text{ Hz}, \tag{2.23}$$

$$f_z = 86.7 \text{ Hz}. \tag{2.24}$$

After exporting particle position data from SIMION, we can derive the power spectral densities of the trapped particle shown in Figure 2.8 from which we can observe the particle mechanical frequencies in the three axes are $f'_x = 9.0$ Hz, $f'_y = 61.0$ Hz and $f'_z = 75.4$ Hz.

Table 2.4 Geometric factors obtained from SIMION numerical simulation of our Micro-Paul Trap.

	x	y	z
α	0.37 ± 0.04	2.24 ± 0.03	-3.36 ± 0.11
β	$(-1.61 \pm 0.05) \times 10^{-1}$	$(-1.58 \pm 0.04) \times 10^{-1}$	0.41 ± 0.01

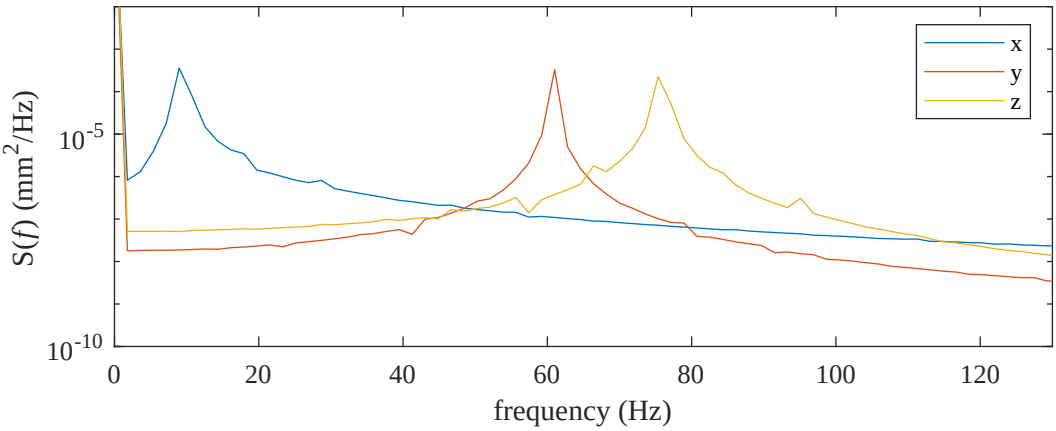

Fig. 2.8 The PSDs of a levitated particle position along three axes in the Micro-Paul trap from SIMION simulation. The blue, red and yellow curves correspond to the PSDs of the levitated particle motion along x, y and z axes. From the obtained PSDs, we can the oscillation frequencies are $f_x' = 9.0$ Hz, $f_y' = 61.0$ Hz and $f_z' = 75.4$ Hz.

In comparison to the extracted frequencies from Equation 2.10, we can derive relative errors as following

$$\left|\frac{f_x' - f_x}{f_x}\right| = \left|\frac{9.0 - 7.9}{7.9}\right| = 13.9\%, \tag{2.25}$$

$$\left|\frac{f_y' - f_y}{f_y}\right| = \left|\frac{61.0 - 57.3}{57.3}\right| = 6.5\%, \tag{2.26}$$

$$\left|\frac{f_z' - f_z}{f_z}\right| = \left|\frac{75.4 - 86.7}{86.7}\right| = 13.0\%. \tag{2.27}$$

The two results are very close to each other with all relative errors below 15%, which might be due to the analytic model (Equation 2.10) not fully capturing the geometry of the Paul trap and verifies we can use SIMION and the simple theoretical model to make predictions in different parameter regimes.

2.3 Paul trap fabrication

Based on the structure size in the simulation of the Micro-Paul trap in Section 2.2.2, we then begin to fabricate an experimental Micro-Paul trap. A linear Paul trap system with 1 mm diameter endcap is initially designed and tested before scaling down to conduct research explorations which is shown in Figure 2.9(a). The trap consisted of six electrodes and the two middle rods work as endcap electrodes. The distance from trap centre to the surface of electrodes is $r = 1.15\,\text{mm}$. The diameter of all holes on two plate pieces is 1 mm. The plate pieces are manufactured with ceramics and 5 mm-long on each side. The plate pieces are 1 mm thick. Figure 2.9(b) illustrates a fabricated Micro-Paul trap based on the design. Two endcap electrodes are with 1 mm diamter and are separated by $300\,\mu\text{m}$.

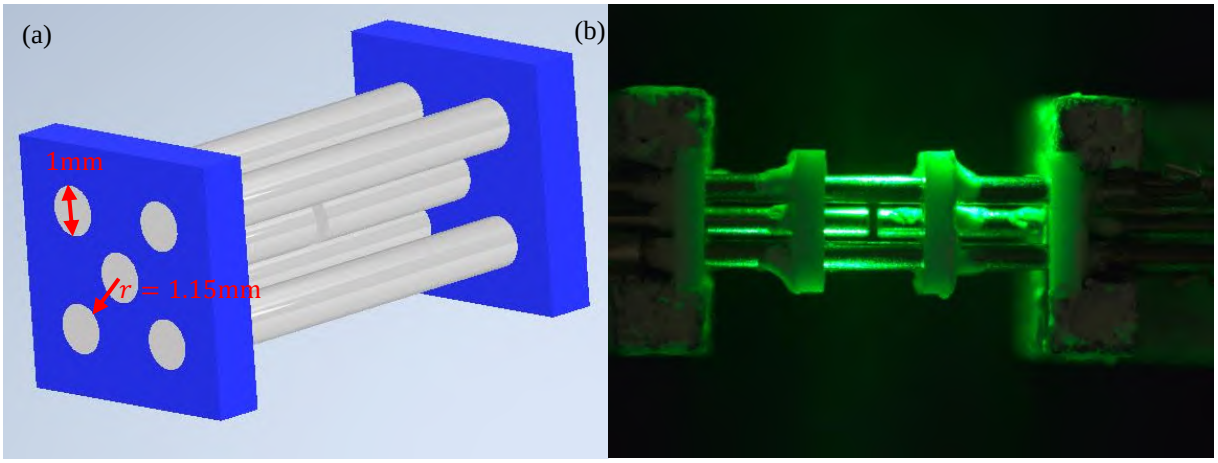

Fig. 2.9 (a) Designed Paul trap geometry. The distance from trap centre to the surface of electrodes is $r = 1.15\,\text{mm}$. All the hole diameters on the Paul trap holder are 1 mm. (b) Fabricated Micro-Paul trap. Two endcap electrodes have 1 mm diameter and the separation between them is $300\,\mu\text{m}$.

When we put the Micro-Paul trap in Figure 2.9(b) to conduct particle trapping, it is difficult to get trapped particles close to the trap centre. Instead, the trapped particles are usually located in a middle region between the trap centre and a nearby electrode, which is shown in Figure 2.10.

In accordance to SIMION simulation, we could get a potential distribution along three axes at the trap central region and the middle region between the trap centre and a nearby DC electrode respectively. Therefore, the geometric parameters of the Micro-Paul trap in Figure 2.9(b) are input to SIMION simulation model. Figure 2.11 gives a comparison of Potential distributions of the two points with DC voltage $U_{DC} = 1\,\text{V}$ and AC voltage $V_{RF}\cos(\Omega_{RF}t) = 200\,\text{V}$. Figure 2.11(a) shows the potential distributions of trap centre and Figure 2.11(b) is the potential distributions of a middle point between the trap centre and a nearby DC electrode. We use a green dot to denote the locations of the two distinct points

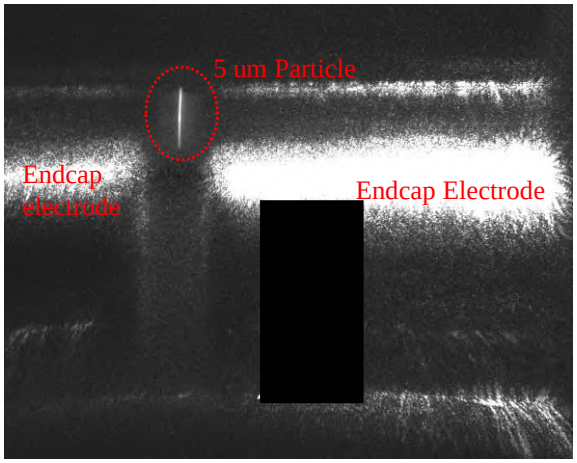

Fig. 2.10 The Micro-Paul trap with trapped particle not in the trap centre. The trapped particle is with 5 μm diameter and located in a middle region between the trap centre and a nearby electrode. The black rectangular region in the image is an area with a part of camera pixels destroyed by our pulsed laser.

individually on the upper-left trap symbol within the two sub-figures. Here we can observe that the distributions of the middle point is close to parabolic and have larger potential gradient in comparison to the distributions of the trap centre. This could explain why the trapped particles mainly locate at the middle point.

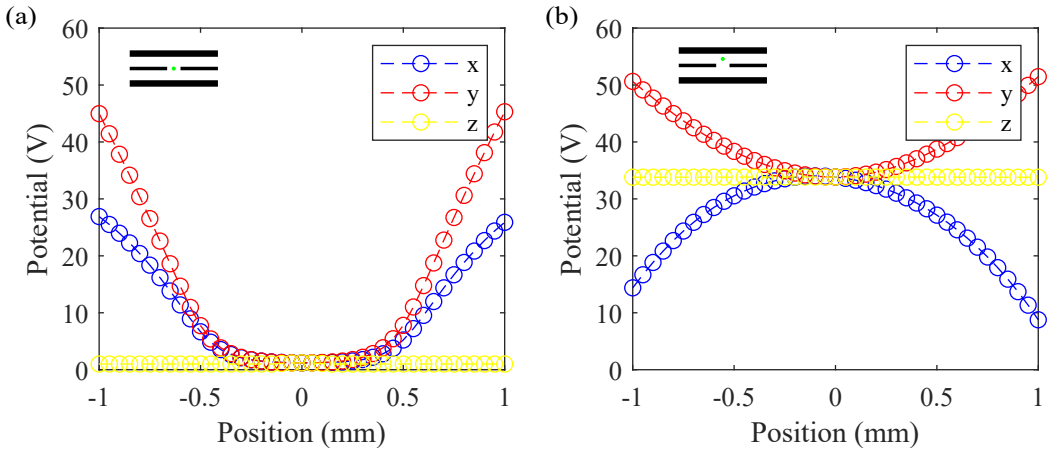

Fig. 2.11 Potential distribution comparison. (a) Potential distributions of trap centre whose location is indicated by the green dot on the upper-left trap symbol. (b) Potential distributions of a middle point between the trap centre and a nearby DC electrode whose location is indicated by the green dot on the upper-left trap symbol.

To further analyze the potential distributions of trap centre, more simulations with various endcap separations and endcap diameters are conducted. Figure 2.12(a)-(c) shows the potential distributions of trap centre when the distances between the two endcap

electrodes are $d = 300\,\mu$m, $d = 500\,\mu$m, $d = 1000\,\mu$m respectively. The diameter of the endcap rods is 1 mm.

To have a clear understanding of the trend of potential distribution with the endcap distance, the potential gradient distributions along three axes are plotted. Figure 2.12(d)-(f) shows that the potential gradient distributions along three axes increases with the endcap distance changes from $300\,\mu$m to $1000\,\mu$m and the fastest gradient increase occurs in z axis as the distance increases. The potential distributions with $1000\,\mu$m endcap separation shows the largest potential gradients of all three axes.

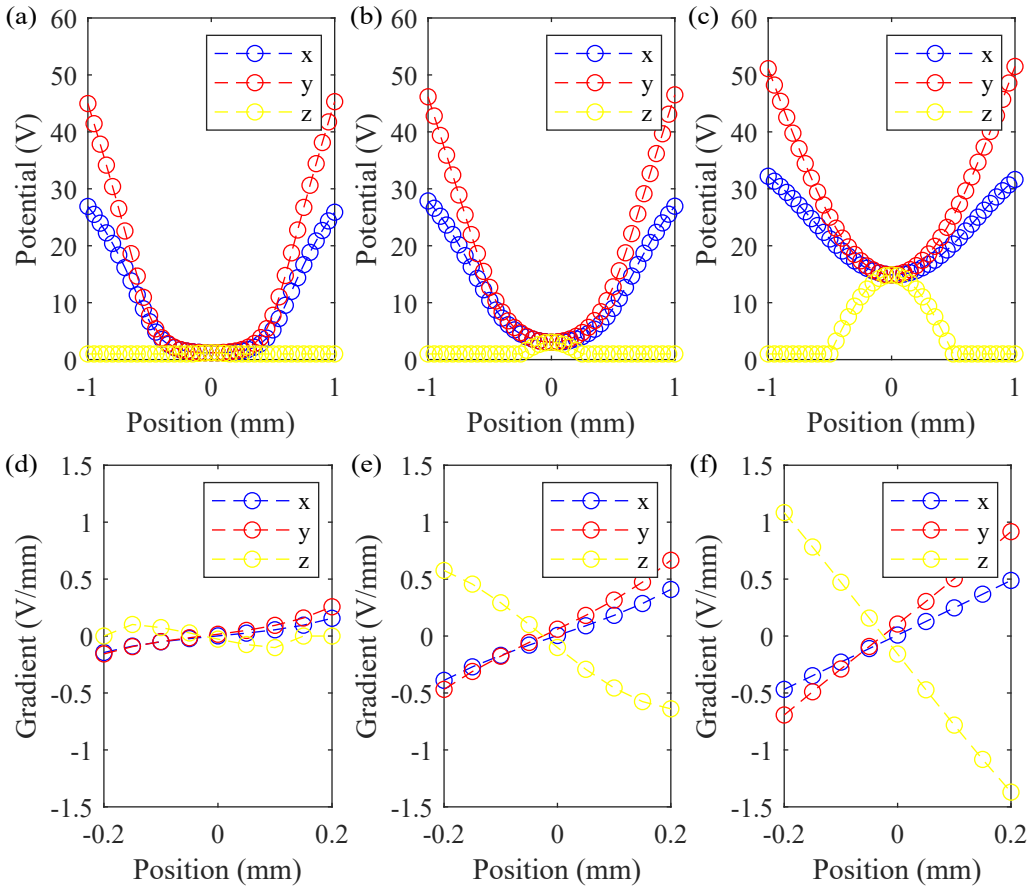

Fig. 2.12 (a)-(c) are potential distributions with various endcap separations at the centre of the trap. (a) Potential distributions with $300\,\mu$m endcap separation. (b) Potential distributions with $500\,\mu$m endcap separation. (c) Potential distributions with $1000\,\mu$m endcap separation. (d)-(f) are potential gradient distributions with various endcap separations at the centre of the trap. (d) Potential gradient distributions with $300\,\mu$m endcap separation. (e) Potential gradient distributions with $500\,\mu$m endcap separation. (f) Potential gradient distributions with $1000\,\mu$m endcap separation.

Simulations with various endcap diameters with the same endcap distance are conducted. The distance between the two endcaps is set to $500\,\mu$m. Figure 2.13 is potential distribution comparison with different endcap diameters. Figure 2.13(a) is with $1000\,\mu$m

diameter endcaps while Figure 2.13(b) has with 500 μm diameter endcaps. The potential distributions with 500 μm diameter endcaps shows larger potential gradients of all three axes compared to Figure 2.13(a). Considering the effects of the two endcap distance and diameters to the potential distribution of trap centre, we couldn't make encap separation very small to 300 μm or keep the endcap diameter large to 1 mm. Therefore, we finally choose a Micro-Paul trap with 300 μm diameter endcaps which are 800 μm separated from each other, which is shown in Figure 2.5. The separation from the centre of the trap to the surface of the rods is $r = 3.45$ mm and the diameter of two AC and DC electrodes are 1 mm.

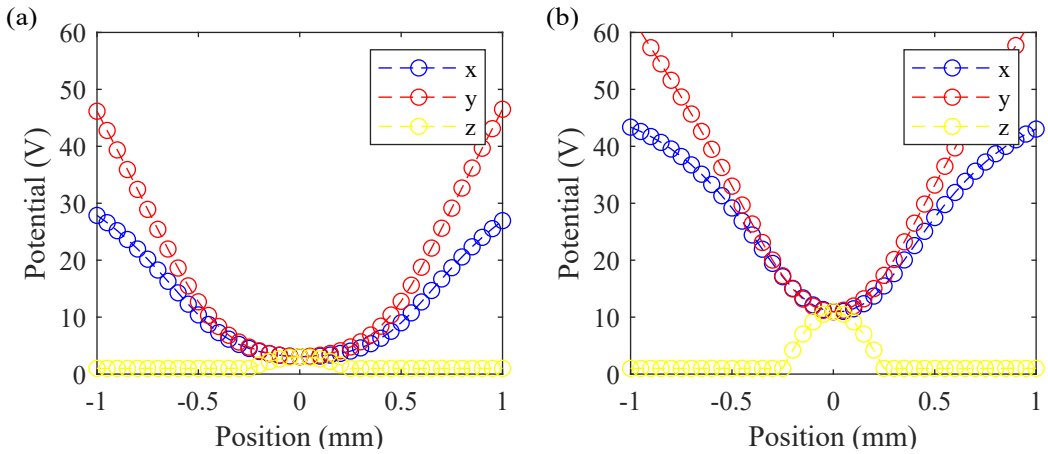

Fig. 2.13 Potential distribution comparison with different endcap diameters. (a) Potential distributions with 1000 μm endcap diameter. (b) Potential distributions with 500 μm endcap diameter.

2.4 Micro-Paul trap setup

Based on the determined Micro-Paul trap geometry depicted in Section 2.3 and the initial version of Micro-Paul trap shown in Figure 2.9(b), we grind the tips of the two endcaps to be 300 μm-diameter and make them separated with each other by $2z_0 = 800$ μm (z_0 is the distance from trap centre to one endcap electrode along z axis.) and from the trap centre to the surface of the rods the separation is $r = 1.15$ mm, which is shown in Figure 2.14.

In consideration of the assembly of the Micro-Paul trap, trap holders are designed and manufactured via 3D printing with MJF Nylon 12 material (More information see Appendix B). We then put the Micro-Paul trap into two trap holders which are connected to a flat board shown in Figure 2.15.

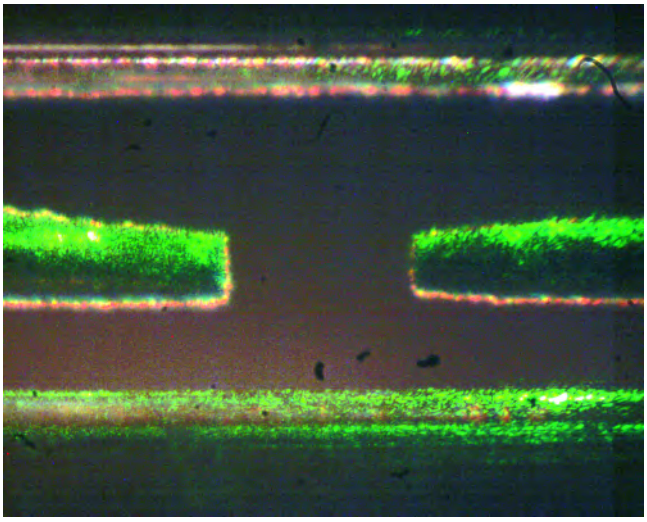

Fig. 2.14 Improved fabricated Micro-Paul trap. Two endcap electrodes are with 0.3 mm diameter and the separation between them is 800 μm.

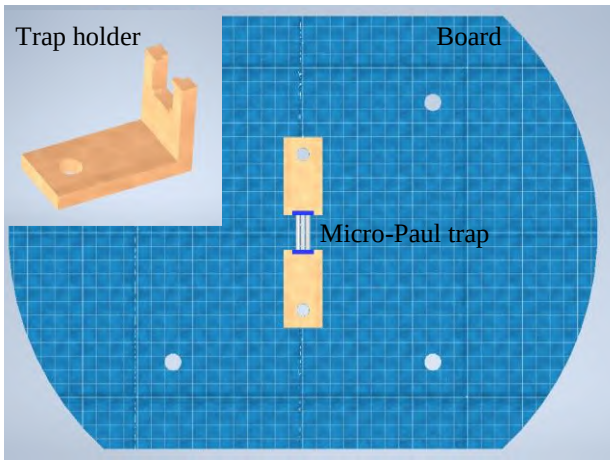

Fig. 2.15 The assembly of the Micro-Paul trap. The Micro-Paul trap mounted into two trap holders which are connected to a flat board.

2.4.1 Setup structure

Figure 2.16 illustrates the experimental setup structure. Laser-induced acoustic desorption (LIAD) method is used to launch particles into trap centre. After a charged particle is trapped in the Micro-Paul trap, an illuminating laser with 520 nm wavelength is focused onto the particle. A detector then receives the scattered light from the particle motion. A quadrant photodiode (QPD) or standard CCD/CMOS camera can also be adopted to detect the motion of the levitated particle.

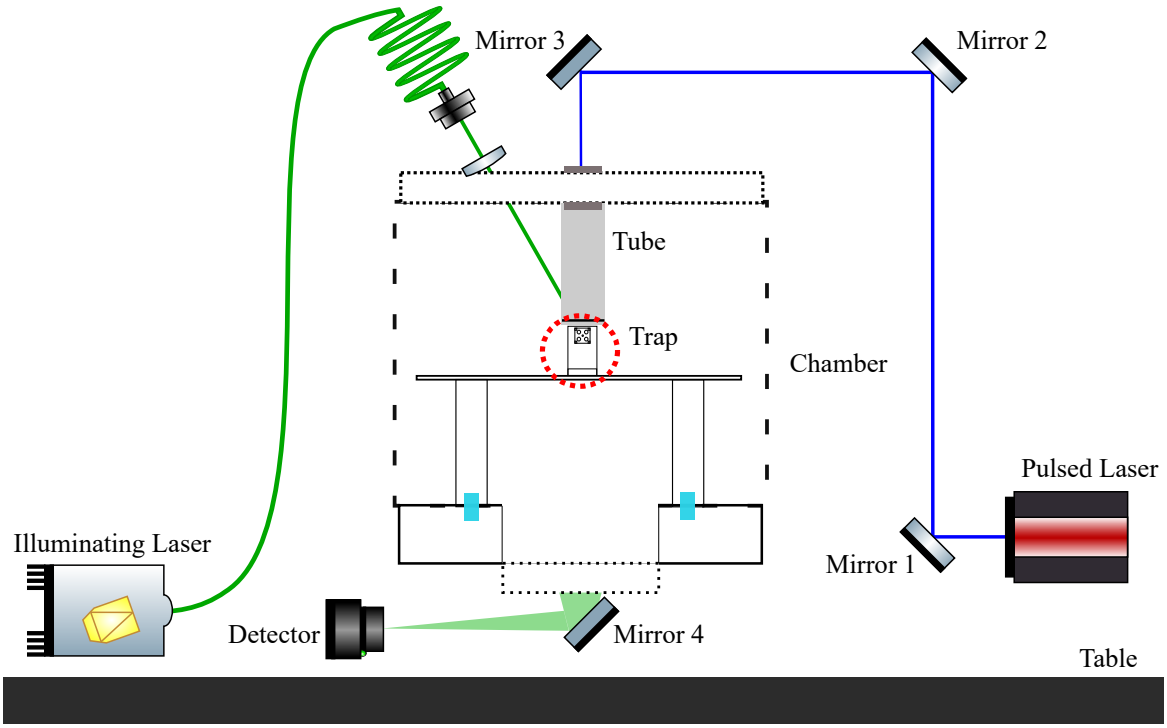

Fig. 2.16 The experimental setup structure. A pulsed laser beam is focused onto the back of the aluminum sheet to launch particles and the wavelength of the illuminating laser is 520 nm and the output power of the laser is 18 mW. After being focused by a convex lens onto a captured particle, a detector is used to receive the scattered light from the particle.

2.4.2 Particle loading

There are commonly several methods to launch particles into optical, magnetic or Paul traps. One method is spraying a solvent with suspending particles via a medical nebulizer [73] or an electrospray [74, 75]. The disadvantage of this technique is that spraying solvents will have a potential to contaminate the vacuum system.

Another method is to launch particles using piezoelectric transducers [76, 77], which is clean and dry. Particle launching requires enough mechanical force to overcome the van der Waals force between the piezoelectric surface and the particles. Although recent work using polytetrafluoroethylene surface instead of glass slides to decrease the particle stiction to the launching surface [78], piezoelectric launching is not suitable for fabricated particles grown on a substrate.

LIAD as another clean and dry method is used in this project. In this method, a pulsed laser is focused to hit the back of a substrate with particles deposited or grown. The pulse generates acoustic shockwaves by inducing thermomechanical stress, leading to the localized ejection of particles from the substrate [19]. The LIAD method works

for dielectric particles with different diameters ranging from $< 100\,\text{nm}$ up to several micrometres at pressures down to 1 mbar [79].

In our experiments, a thin aluminum sheet is firstly used to deposit 5 μm diameter silica particle samples (Bangs Laboratories; SSD5003). After rubbing two sheets with the particle samples inside, the silica microparticles get charged. A pulsed laser is with a wavelength of 532 nm, a pulse length of about 4.6 ns and typically operated in single-shot mode with a peak intensity of 588 GW/cm^2. A tube is used to hold the aluminum sheet. The distance from the sheet to trap centre is about 5 mm. The pulsed laser beam (Litron Lasers; model: NANO-S 120-20) is focused onto the back of the aluminum sheet to launch particles into trap centre at 2 to 10 mbar to provide enough gas damping to the kinetic energies of microparticles. Trapped particles can usually stay inside the Paul trap for several months.

2.4.3 Particle motion detection

Figure 2.17 describes the situation of the Micro-Paul trap which has a small endcap separation of 800 μm with a 5 μm diameter silica particle trapped. According to the stability region of the Paul trap and simulations based on SIMION, we pick up values for AC voltage and DC voltage. The setting AC voltage is with frequency $\Omega_{RF} = 2\pi \times 1100\,\text{rad}\,\text{s}^{-1}$ and amplitude $V_{RF} = 404\,\text{V}$, and the setting endcap voltage is $U_{DC} = 0.1\,\text{V}$. A QPD is used to detect the position of the levitated particle. Figure 2.18 shows detected results of the trapped microparticle. Figure 2.18(a) gives position signals of the levitated particle along z and y axis and Figure 2.18(b) illustrates the related PSDs along the two axes, from which we can obtain that the particle oscillation frequencies along three axes are $\omega_x = 13 \times 2\pi$ rad/s, $\omega_y = 78 \times 2\pi$ rad/s and $\omega_z = 115 \times 2\pi$ rad/s. From the data sheet of silica particle producer we can get the uncertainty of particle radius is 0.1 μm and from a Lorenzian fitting to the motion PSD we get the uncertainty of $\omega_z = (0.01 \times 2\pi)$ rad/s. Assume the uncertainty of r is about 5% and according to Equation 2.13 we can derive the charge of the levitated particle $Q = 5600 \pm 900\,\text{e}$.

We set the AC and DC voltages to be the same in SIMION simulation and the particle to have mass $m = 8.02 \times 10^{13}$ amu and charge $Q = 5600\,\text{e}$. We can get simulations of the trapped microparticle shown in Figure 2.19. Figure 2.19(a) gives position signals of the levitated particle along x, y and z axis. Figure 2.19(b) shows the PSDs of particle position signals along the three axes, from which we can extract the particle oscillation frequencies of three axes are $\omega_x = 13 \times 2\pi$ rad/s, $\omega_y = 80 \times 2\pi$ rad/s and $\omega_z = 100 \times 2\pi$ rad/s. Compare the extracted motion information from QPD detection and SIMION simulation, the two groups of obtained frequencies are quite close to each other, verifying that the particle motion detection from QPD is reasonable.

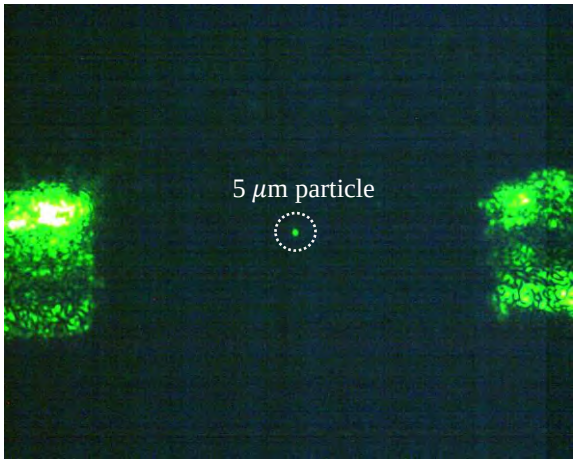

Fig. 2.17 The Micro-Paul trap with a levitated particle. Two endcap electrodes are with 0.3 mm diameter and the separation between them is 800 μm.

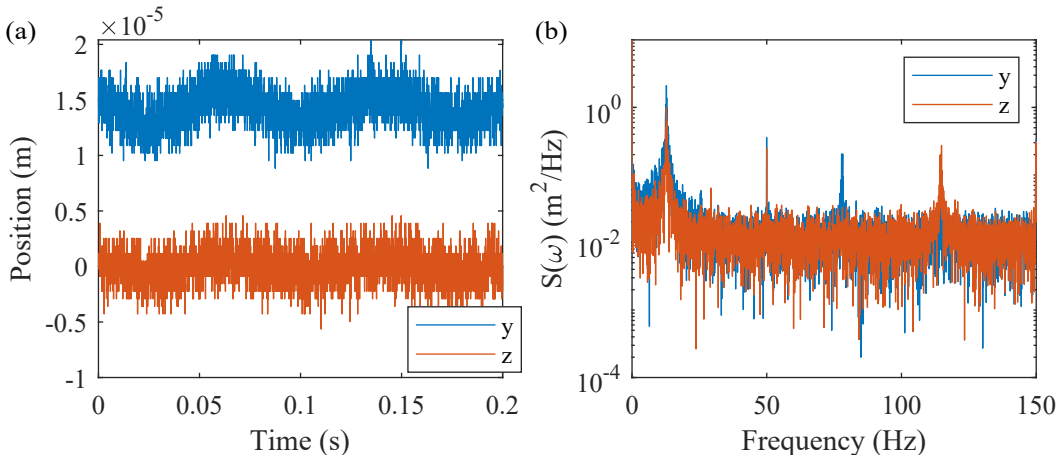

Fig. 2.18 Motion detection of a levitated particle based on a QPD. (a) Position signals of the levitated particle along z and y axis. (b) PSDs of the particle position signals along z and y axis. Blue and orange curves represent the motion along z and y axis respectively.

A CCD or CMOS camera can also be used to detect the trapped particle motion. Via constraining the region of interest (ROI) of the camera, the frame rate can be increased to a few hundred frames per second (fps). Here we introduce a CMOS camera (Thorlabs; model: CS165MU) to recover the particle motion and then make a comparison to the motion detection based on QPD shown in Figure 2.20. Figure 2.20(a) is the PSDs of particle motion along y and z axis based on the QPD detection, from which we can extract the particle oscillation frequencies are $\omega_x = 20 \times 2\pi$ rad/s, $\omega_y = 63 \times 2\pi$ rad/s and $\omega_z = 75 \times 2\pi$ rad/s. Figure 2.20(b) depicts the PSDs of particle motion along y and z axis based on the CMOS detection, from which we get the same motion frequencies. Thus, the feasibility of motion detection based on the CMOS camera is verified.

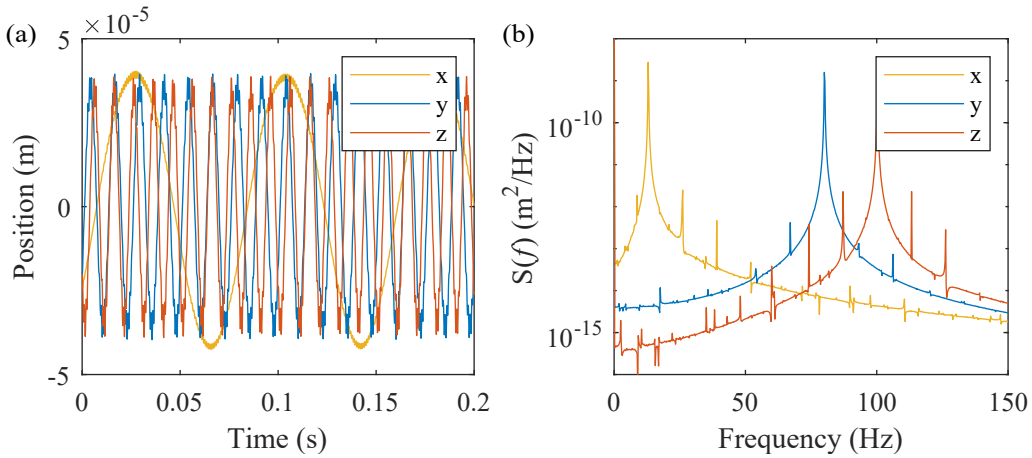

Fig. 2.19 Motion detection of a levitated particle from SIMION simulation. (a) Position signals of the levitated particle along x, y and z axis. (b) PSDs of the particle position signals along the three axes. Yellow, orange and blue curves represent the motion along x, y and z axis respectively.

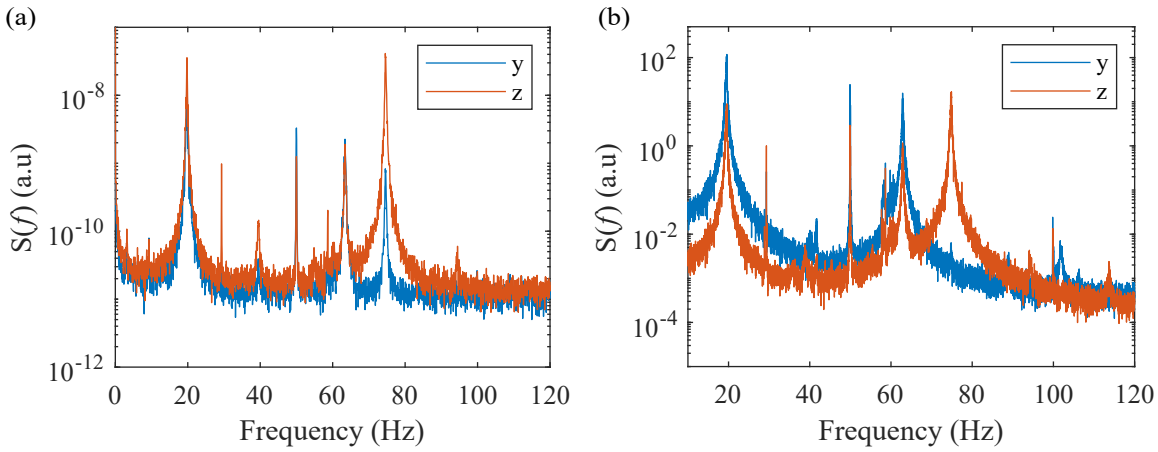

Fig. 2.20 Comparison of particle motion detection based on QPD and CMOS camera. (a) PSDs of particle motion along y and z axis based on the QPD detection. (b) PSDs of particle motion along y and z axis based on the CMOS detection.

2.4.4 Particle motion calibration

Calibration: obtaining conversion factor

The detection which record the particle motion is calibrated by applying a known potential difference ΔU across the endcap electrodes, causing the particle to move in the z-direction. The particle oscillates at the centre of the trap when $\Delta U = 0\,\mathrm{V}$. If the voltage of one of the endcaps is modified from $U_0 \rightarrow U_1$, the resulting voltage difference $\Delta U = U_1 - U_0$ exerts a force on the particle $\vec{F}_z = F_z\hat{z}$, where $\hat{z}$ denotes a unit vector along the z-axis, determined by:

$$F_z = \frac{Q\,\Delta U}{d}\,, \tag{2.28}$$

where d is the distance between the endcap electrodes. We confirm this analytic model for our specific trap geometry in Section 2.2. Since the Paul trap provides a harmonic pseudo-potential, the particle also experiences a linear restoring force:

$$F_z = -k\,\langle z\rangle\,, \tag{2.29}$$

where k is the trap stiffness and $\langle z\rangle$ is the average position of the particle (assuming $\langle z\rangle = 0$ when $\Delta U = 0$).

Noting that the measured $\langle z_m\rangle$ is in volts for the QPD, and related to the true value of $\langle z\rangle$ through a conversion factor γ, with units V/m and pixels/m, respectively, we can equate these two equations. Considering further that $k = m\omega_z^2$ for a harmonic oscillator of mass m and oscillation frequency ω_z, then:

$$\langle z_m\rangle = -\gamma\frac{Q}{m}\frac{\Delta U}{d\,\omega_z^2}\,. \tag{2.30}$$

By measuring the mean displacement of the particle as ΔU is varied, we can determine the conversion factor γ for each detector.

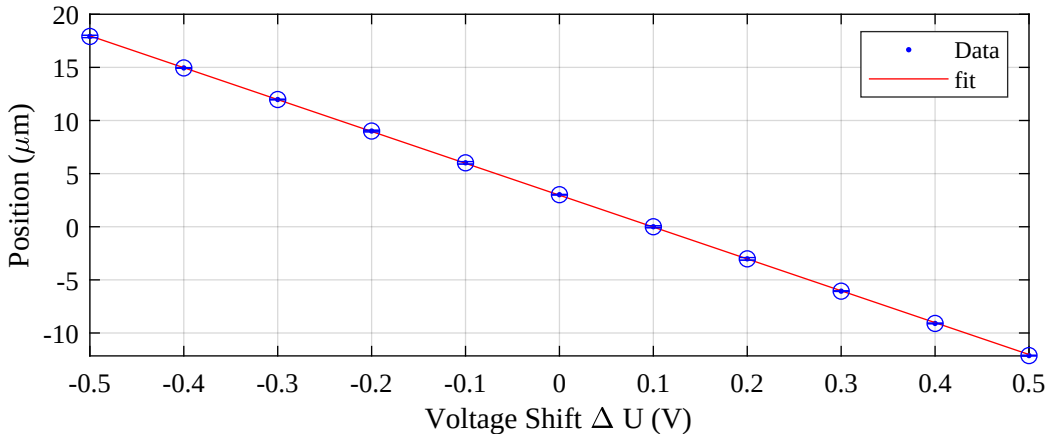

Fig. 2.21 Simulation verification of calibration method based on SIMION model in Figure 2.1. The mean position variations of the trapped particle with different voltage differences of two endcap rods, where a clear linear relationship can be seen.

To further verify the Equation 2.30, simulations based on SIMION are conducted. Figure 2.21 shows that when the voltage of one endcap is tuned by -0.5V to 0.5V, the related mean positions of the trapped particle linearly changes, verifying the feasibility of the used analytical expression.

Figure 2.22 illustrates the calibration in experiments for the same levitated particle. When we change the voltage of one endcap from -0.05V to 0.05V, the related mean positions of the trapped particle changes linearly both from QPD and CMOS camera detection.

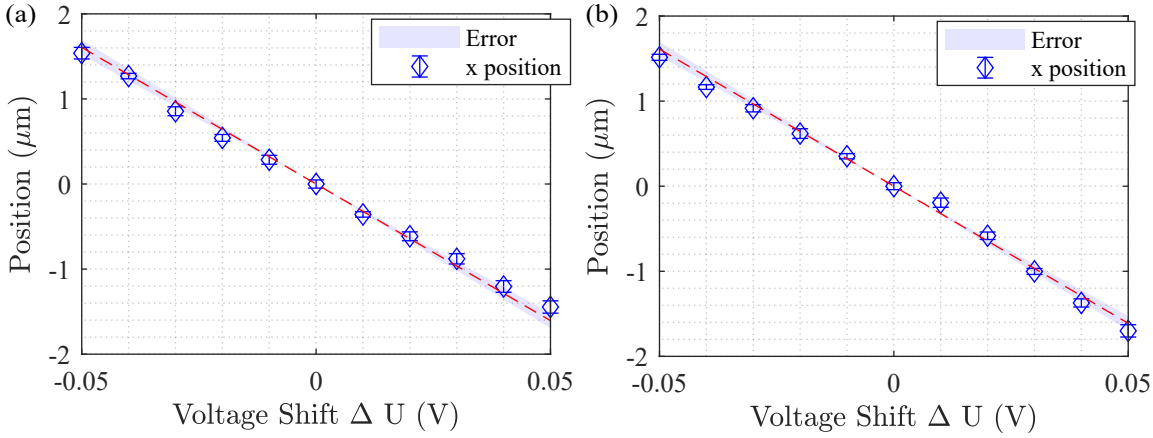

Fig. 2.22 Calibration comparison based on QPD and CMOS detection. (a) The mean position variations of the trapped particle with different voltage differences of two endcap rods from QPD detection. (b) The mean position variations of the trapped particle with different voltage differences from the CMOS camera detection.

Calibration: non-linear calibration with QPD

The QPD has a non-linear response to the movement of an image if the image deviates too far from the centre of the detector, i.e. if the particle moves too far from the centre of the trap. The image that the particle makes on the QPD has a 2D Gaussian intensity distribution, we can fit an error function (or Gauss error function) [80] to the mean measured position of the particle [81] (recorded in Volts, $\langle z_V \rangle$), with the expected actual position $\langle z_m \rangle$ based on the amount of applied potential difference, Equation 2.30.

$$\langle z_V \rangle = a_V + b_V \times \mathrm{erf}\left(\frac{\langle z_m \rangle - c_V}{d}\right), \tag{2.31}$$

where (a_V, b_V, c_V, g_V) are fitting constants obtained by fitting the above equation to the data as shown in Figure 2.23 and $\mathrm{erf}(z) = \frac{2}{\sqrt{\pi}} \int_0^z e^{-t^2}\, dt$. Compared to Figure 2.21, when the particle moves far from the trap centre, the response of the QPD is not linear and the Equation 2.30 is not suitable for calibration. The inverse of this error function then enables us to convert the positional information in volts $\langle z_V \rangle$ to metres $\langle z_m \rangle$.

$$\langle z_m \rangle = g_V\, \mathrm{erf}^{-1}\left(\frac{\langle z_V \rangle - a_V}{b_V}\right) + c_V, \tag{2.32}$$

This enables us to extend the detection range of the QPD by a few microns, but not reach the tens of microns.

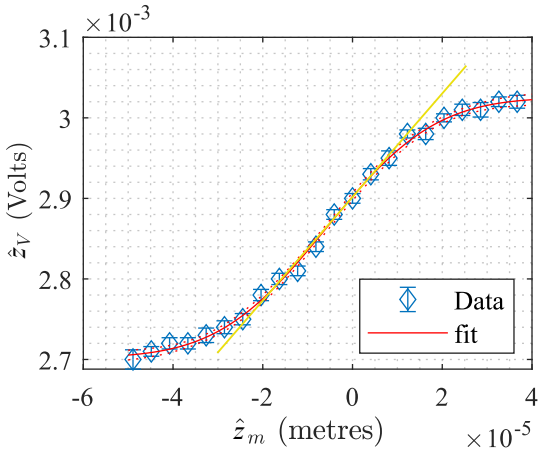

Fig. 2.23 Error function fitted to the measured mean position in volts, $\langle z_V \rangle$ of the particle when a potential difference ΔU is applied across the endcaps. The measured position $\langle z_V \rangle$ is converted to the actual position $\langle z_m \rangle = -\gamma \frac{Q\Delta U}{m\omega_z^2 d}$. The inverse of the error function then converts Volts into metres. A linear yellow line is labelled for checking the nonlinear calibration.

Calibration: a Lorentzian function fitting to PSD

The fitting to a PSD of a levitated particle with Equation 2.15, a Lorenzian function, will help to extract particle motional frequencies ω_i ($i = \{x, y, z\}$), particle damping rate Γ_0 and the centre-of-mass temperature T_{CoM}.

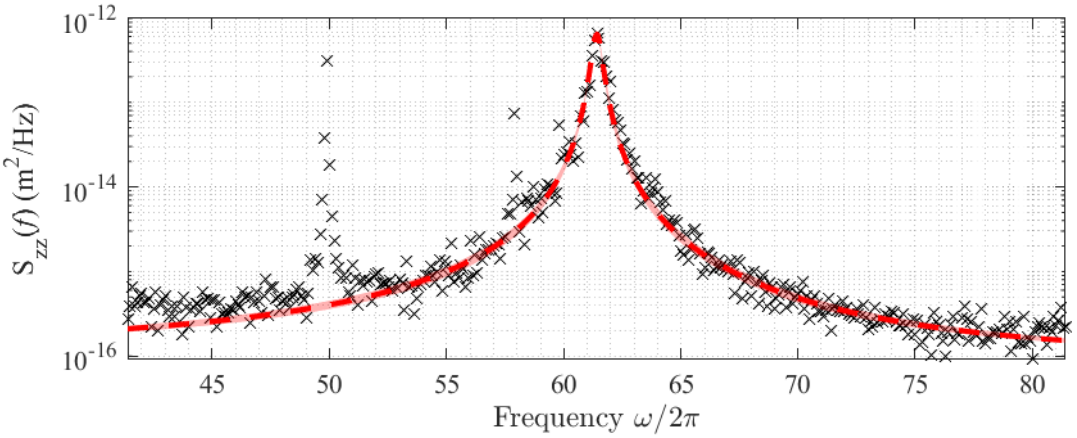

Fig. 2.24 The fitting to a PSD of a levitated particle. Black dots represent experimental position data along z axis and red curve is the the fitting line based on Equation 2.15.

Figure 2.24 illustrates the fitting with Equation 2.15, in which black dots are experimental position data along z axis and red curve is the the fitting line. We therefore can obtain the following information of the levitated particle: motional frequency along z axis $\omega = (61.40 \pm 0.01) \times 2\pi$ rad/s, damping rate $\Gamma_0 = (0.45 \pm 0.04) \times 2\pi$ rad/s, and the centre-of-mass temperature $T_{\mathrm{CoM}} = 1320 \pm 90$ K, which is higher than the room temperature due to the electric noises.

Calibration: solving for Q/m

Considering that our system follows a Mathieu equation of motion then the frequency of the different degrees-of-freedom can be written as,

$$\omega_i \cong \frac{1}{2}\Omega_{RF}\sqrt{a_i + \frac{1}{2}q_i^2}, \tag{2.33}$$

where ω_i are the harmonic oscillation frequencies, Ω_{RF} is the driving RF frequency, and a_i, q_i with $i = \{x, y, z\}$ are the stability parameters [82].

Using the stability parameters we can write a general statement for all three axis:

$$\omega_i^2 = q_m^2\left(\frac{V_{RF}^2}{2\Omega_{RF}^2 r^4}\alpha_i^2\right) + q_m\left(\frac{2U_{DC}}{d^2}\right)\beta_i, \tag{2.34}$$

where $q_m = Q/m$ is the charge-mass ratio, V_{RF} is the RF voltage amplitude, U_{DC} is the DC voltage at the endcaps, r is the distance between RF electrodes from the centre of the trap and d is the distance between the endcap electrodes. The variables α_i and β_i are geometric factors that are obtained through SIMION numerical simulation of the Paul trap used in the experiments (see Table 2.2) for each axis. The ratio q_m then can be calculated from experimentally measured values of ω_i. In our experiments, the charge of trapped particles usually range from 2×10^3 e to 2×10^4 e and the mass is $(1.3 \pm 0.2) \times 10^{-13}$ kg.

In conclusion, we introduced Paul trap theory which includes equations of particle motion, power spectral density. Simulations based on SIMION are introduced to provide the geometric information of Paul traps and predict particle behaviour. A Micro-Paul trap is fabricated and related experimetal setup is designed and assembled in which LIAD method is adopted to launch particles into trap centre and QPD and CMOS camera are used to detect the motion of levitated microparticles. Furthermore, particle motion calibration principles are explained incorporating obtaining conversion factor, solving for charge-to-mass ratio Q/m, nonlinear calibration with QPD and a Lorenzian function fitting to the PSD of motion.

Chapter 3

Event-based imaging of levitated microparticles

In this chapter, the objective is to realize the motion detection of both single and multiple particles via the event-based imaging technique. The work in this chapter was based on the Macro-Paul trap and published as Yugang Ren, Enrique Benedetto, Harry Borrill, Yelizaveta Savchuk, Katie O'Flynn, Muddassar Rashid, and James Millen. "Event-based imaging of levitated microparticles." Applied Physics Letters **121**, 113506 (2022) [83].

3.1 Introduction

When unravelling the underlying physics of particles interacting with external forces, or of interacting multi-particle systems, object tracking is key. One must consider a range of detection metrics such as field-of-view, resolution, latency, sensitivity, bandwidth, signal-to-noise ratio (SNR) and the ability to detect multiple objects.

In this work, we consider tracking the motion of microparticles levitated under vacuum conditions by optical, electrical or magnetic fields [84, 85]. Such systems are of interest for studies of fundamental quantum science [86], nano-thermodynamics [87] and advanced sensing [88, 89].

When working with particles optically trapped in liquid, it is sufficient to use standard CMOS or CCD cameras to track their motion, since the viscous damping provided by the liquid reduces dynamical timescales to a level suitable for camera frame-rates. However, if we want to study ballistic Brownian motion, or objects that are levitated in vacuum with their motion underdamped, faster tracking is required [4]. Although this is possible at the 100 kHz level with high-speed CMOS cameras [90], this requires significant reduction in the region of interest (ROI). Hence, particle tracking is usually performed using photodiodes, balanced photodetectors or quadrant photodetectors. Whilst these devices

are fast, even tracking at GHz rates [91, 92], they have limited field-of-view, restricting tracking to scales not much larger than the optical wavelength. This can limit studies of nanothermodynamics or non-linear motion where particles may explore large regions of space [86, 93, 4].

Additionally, a key technique when working with levitated objects is the application of real-time feedback onto their motion. This has enabled cooling to the quantum ground state of a harmonic potential [13], but more generally is essential for stabilization under vacuum conditions. Balanced photodetectors are the standard tool to realise real-time feedback [57], although recent work employing powerful graphics cards with a limited number of pixels [39] or on-board microprocessors [67] has enabled feedback control of sub-500 Hz oscillators via CMOS camera detection. We also note that cameras have excellent SNR and allow super-resolution detection [39], allowing one to minimize the amount of light required to detect levitated particles avoiding absorption [94] and photon recoil heating [18].

Finally, the prospect of levitating systems of multiple interacting particles has emerged [85, 95], for distributed sensing [96] or generation of entanglement [97]. Single photodetectors can only track single particles, whereas cameras are well suited to multi-particle detection.

Conventional, CMOS/CCD based cameras work using a specified region of interest or the whole pixel array to capture light from a scene. An alternative approach is that of event-based imaging (EBI), where pixels work independently of each other, triggering only when the change in light intensity is above a preset threshold [98]. This enables a dynamic ROI, thus enabling decreased informational load compared to conventional cameras.

In this chapter, we apply EBI for detecting the motion of microparticles levitated in vacuum. This imaging technique offers the potential for tracking single and multiple objects with high bandwidth, whilst an integrated tracking algorithm provides the real-time position of each object for use in feedback for state control.

3.2 Principles of Event-based detection

Conventional cameras, such as CMOS/CCD, capture continuous movement as a sequence of still images (frames) formed from every pixel of the sensor. As a result, stationary elements are unnecessarily replicated, while moving elements are under-sampled [99].

EBI provides an approach to image acquisition by only capturing changes in images through the detection of modifications in light intensity on each pixel [98]. Pixels in these neuromorphic sensors (sensors that try to mimic the neural structure of the brain) are completely independent. Each one of them contains a contrast detector (CD) that

continuously tracks photocurrents. When the variation of a photocurrent crosses a threshold, the CD triggers a contrast detection event, which represents a relative increase (positive) or decrease (negative) in light intensity. It then initiates the measurement of a new value, as outlined in fig. 3.1(b). Pixels which do not observe changes in light intensities that exceed the threshold do not produce output.

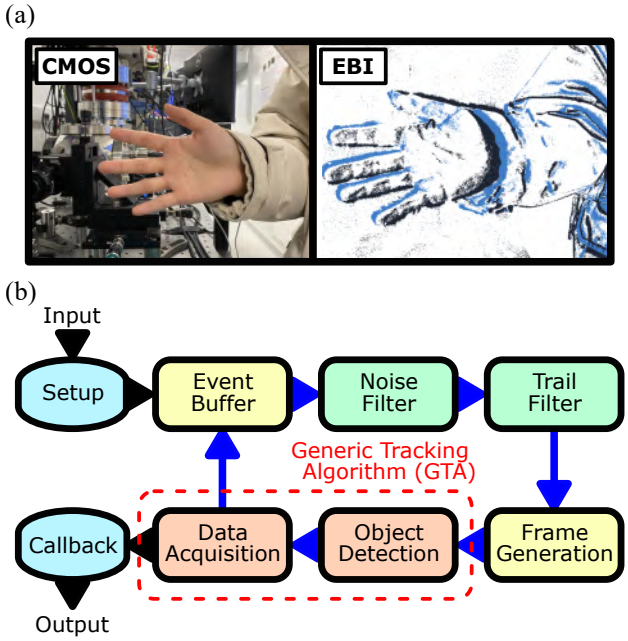

Fig. 3.1 (a) Left image is taken with a conventional CMOS camera, right image is taken by a camera using EBI. The black and blue pixels in the image correspond to negative / positive changes in light intensity, respectively. (b) Information pipeline from the point of data capture in an EBC.

This can be seen in fig. 3.1(a) where two images obtained with different cameras are shown. The event-based image consists of only three colours: white pixels indicate no change in light intensity across the threshold; blue and black pixels represent positive and negative changes in light intensity across the threshold, respectively. Only the blue and black pixels are transmitted as data. By comparing both sets of images in fig. 3.1(a), it is clear that the amount of data transferred is suppressed with EBI.

In conventional cameras the bandwidth of the communication link is usually a constraint whenever higher acquisition rates are needed to track rapid movement. This leads users to reduce the ROI of the sensor to decrease the amount of data per frame [39]. Due to the suppression of data redundancy, and the fact that EBI sensors have an effective pixel depth of 1-bit (an event is either detected or not), the data volume transmitted is considerably reduced, allowing acquisition rates over 1 GHz [98].

Figure 3.1(b) shows the detailed process of object tracking based on EBI. In an event-based camera (EBC), the EBI sensor is packaged with hardware which performs object

tracking, such that the output of the EBC lists the position of each detected object as a function of time. All of the input information related to the camera sensor is read, and in the setup period camera sensor parameters are tuned. An event producer, which is contained in the event buffer, is used to generate a stream of events. For each stream of events, a noise filter is applied to pick up events in the neighboring 8 pixels during a certain time. A trail filter then accepts an event if the last event is detected at the same position within an accumulation time. All of the data collected by the sensor pixels generates a frame and a proprietary generic tracking algorithm (GTA) analyzes these frames to extract detected objects and associate data to previous frames. The deployed tracking algorithm limits the effective frame-rate of the EBC as compared to the read-out rate of the EBI sensor. When the detected object is recognized, there is a trigger in callback and the motional information of the detected particle is obtained from output.

3.3 Particle tracking

Detection based on object tracking (rather than, for example, measuring the intensity of light) has been shown to allow sub-pixel resolution and low noise [39]. The dynamic range of the EBI sensor used in this study [1] is 120 dB, which is high compared to standard CMOS / CCD ($\sim$ 70 dB) or EMCCD ($\sim$ 100 dB) sensors. It is hard to quantify the effect of shot noise or dark counts on the GTA, and hence make a direct comparison to photodiode-based tracking. We use an EBC [2] to track the motion of levitated microspheres.

3.3.1 Schematic of experimental setup

Charged silica microspheres of diameter 5 μm and charge Q are levitated in partial vacuum using a Paul trap (the Macro-Paul trap in Section 2.2.1), made with four 3mm-diameter rods and two 1mm-diameter endcap rods (not shown, aligned axially along the centre of the structure), as illustrated in fig. 3.2. The microsphere is trapped using an oscillating electric field and the particles deposited on an aluminium foil are loaded into the Paul trap using LIAD [19, 79] as described in Section 2.4.2 at a pressure of 2×10^{-2} mbar. An illumination laser (532 nm) is focused onto the trapped particle, with a beam waist of $\sim 80\,\mu$m. The scattered light is collected by a microscope (16$\times$ magnification) and directed onto the EBC for motion detection. There is a coordinate system of the camera besides the Paul trap coordinate system and the two are not the same, but the z axis is common.

[1] Prophesee PPS3MVCD, 640×480 pixels
[2] Prophesee Evaluation Kit Gen3M VGA CD 1.1

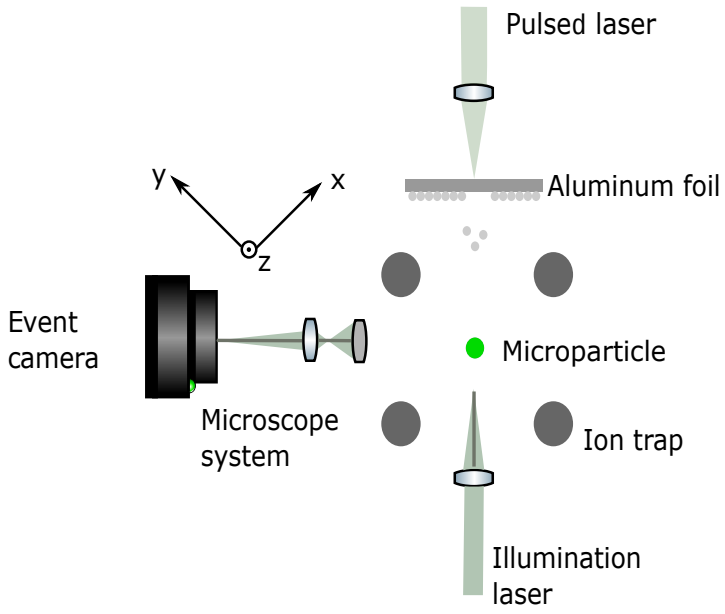

Fig. 3.2 Schematic overview of experimental setup. Silica microspheres are levitated in a Paul trap, illuminated by a laser, and the scattered light is imaged onto an EBC or QPD.

3.3.2 Single particle tracking

The AC voltages are with frequency $\Omega_{RF} = 2\pi \times 800\,\mathrm{rad\,s^{-1}}$ and amplitude $V_{RF} = 750\,\mathrm{V}$. The two endcap electrodes are held at $U_{DC} = -4$ V DC. Figure 3.3 gives the related position detection results of single particle tracking via EBC. The time domain signal is illustrated in fig. 3.3(a) and PSDs of the particle motion along three axes are shown in fig. 3.3(b), from which we can notice the oscillation frequencies are 53.2 Hz, 82.7 Hz and 85.9 Hz as for x, y and z axis. The SNR at the motional frequency f_z is about 30 dB, which reaches a similar SNR level compared to QPD-based motion detection. The bandwidth of the PSDs is 500 Hz, due to 1 kHz frame rate of the tracking algorithm.

In fig. 3.4 we present the SNR at the motional frequency of the particle as recorded by the EBC, as we vary the power of the illumination laser to make the scattered light received via the EBC from 10 μW scale to 10^3 μW scale and then measure the SNR of the EBC at the resonant frequency of the particle motion f_z. To do this, we fit the following empirical model to the noise floor of the detector, by analysing its PSD:

$$\mathrm{Noise}\,(f) = \log_{10}\left(\frac{a_0}{f} + \frac{b_0}{f^2}\right), \tag{3.1}$$

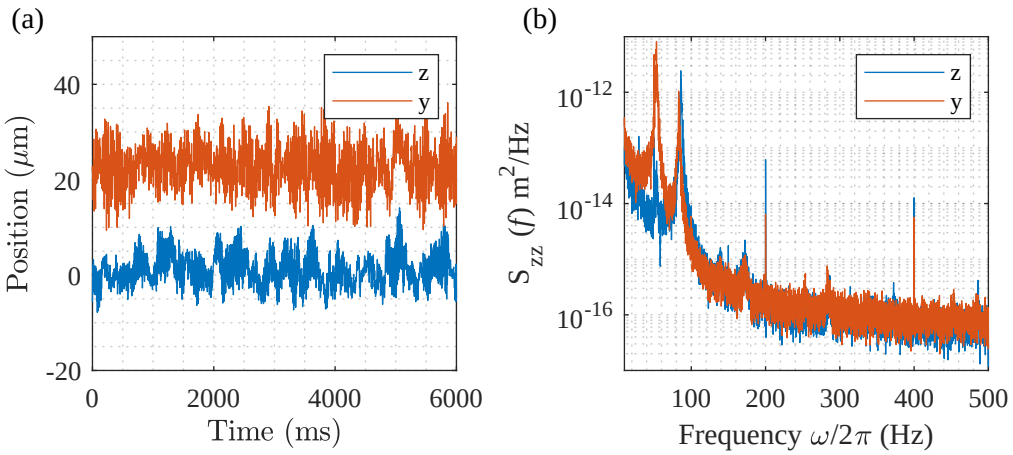

Fig. 3.3 (a) Time domain motion of a levitated microparticle detected via the GTA of an EBC. Blue line and red line represent the particle motion along z and y axis respectively. (b) Corresponding PSDs, illustrating the oscillation frequencies along three axes are 53.2 Hz, 82.9 Hz and 85.9 Hz as for x, y and z axis.

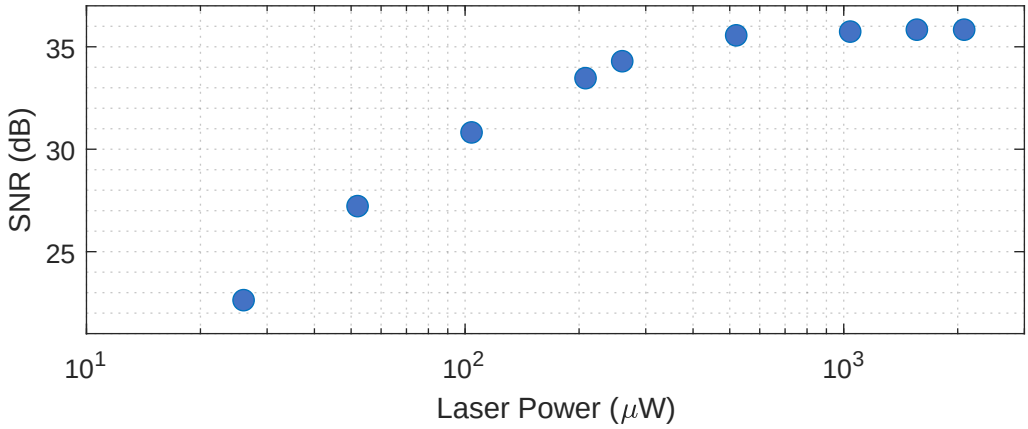

Fig. 3.4 EBC SNR at the motional frequency of the levitated microparticle, as a function of the maximal scattered laser power reaching the detector.

where a_0, b_0 are fitting constants. We found that both terms were required to get a good fit. We fit the PSD of the particle motion with a standard model[87], with the above noise model added:

$$\text{Signal}\,(f) = \log_{10}\left(\frac{ac}{\left(b^2-f^2\right)^2+(cf)^2}+\frac{a_0}{f}+\frac{b_0}{f^2}\right), \tag{3.2}$$

where a, b, c are fitting constants. Therefore, the SNR at the motional frequency is obtained via $\text{SNR}\,(f_z) = \text{Signal}\,(f_z) - \text{Noise}\,(f_z)$.

We can see the detected SNR is increasing with the increment of laser power and then the SNR reaches a maximal value of about 35 dB. According to the data in fig. 3.4 we

estimate the maximal scattered power reaching the EBC sensor, illustrating the excellent sensitivity of the detector.

In order to have a more clear understanding of our single particle tracking based on EBC, we conduct a comparison of EBC and QPD detection. Figure 3.5(a) shows the output from the EBC compared to the output of a QPD [3], when tracking the oscillatory motion of a microparticle using identical imaging systems. Due to the limited speed of the tracking algorithm, the GTA acts like an effective filter, removing high-frequency noise. Figure 3.5(b) shows the corresponding derived PSDs of the particle motion. Like all balanced detection methods, the QPD minimizes $1/f$ noise at low frequencies, whereas the EBC has lower-noise performance at higher frequencies.

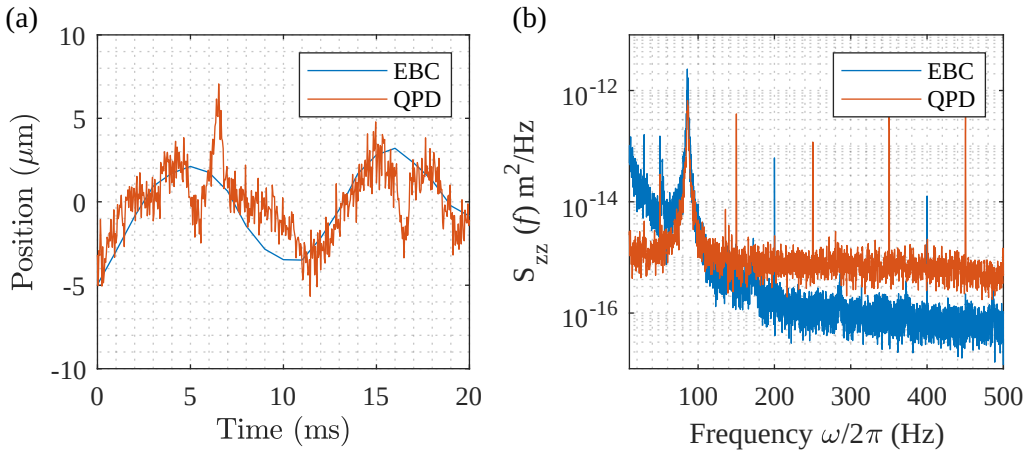

Fig. 3.5 (a) Time domain motion of one degree-of-freedom of a levitated microparticle, obtained via the GTA of an EBC (blue) and via a QPD (red). (b) Corresponding PSDs, illustrating the varying noise characteristics of the two detection methods.

Regardless of the detection method used, the detector has to be calibrated. To calibrate the system and obtain a conversion function we apply an electric force, F_z to the particle via a potential difference ΔU across the endcap electrodes (More information see Section 2.4.4):

$$F_z = \frac{Q\Delta U}{d}, \tag{3.3}$$

where d is the spacing between the endcap electrodes, which is equal to spring force experienced in the trap: $m\omega_z^2\langle z\rangle$. When equated with the above equation we get a theoretical value for positional shift in metres for an applied voltage difference ΔU:

$$\langle z\rangle = \frac{Q}{m}\frac{\Delta U}{\omega_z^2 d}, \tag{3.4}$$

[3] New Focus 2901 Quadrant Cell Photoreceiver

The oscillation frequency ω_z can be obtained from the power spectral density (fig. 3.5(b)) and Q/m obtained by solving the Mathieu equations. More detailed information can be found in Section 2.4.4. In our system we typically trap particles with positive charges.

The calibrated particle position as a response to a potential difference can be seen in fig. 3.6(a). It is apparent that as $|\Delta U|$ becomes large, the response of the QPD becomes non-linear, whereas eqn. (3.4) predicts a linear response. This can be somewhat mitigated through a non-linear calibration (more detailed information in Section 2.4.4) but limits the field-of-view of the QPD. On the other hand, the EBC has a linear response to the particle displacement across the full range. Figure 3.6(b) shows a histogram of the equilibrium motion of the trapped particle. The amplitude of detected motion via EBC is 9.4 μm while the value from QPD detection is 5.7 μm, again showing that large displacements are missing when using the QPD. Hence, we can track both small (i.e. the oscillatory motion) and large displacements using EBI.

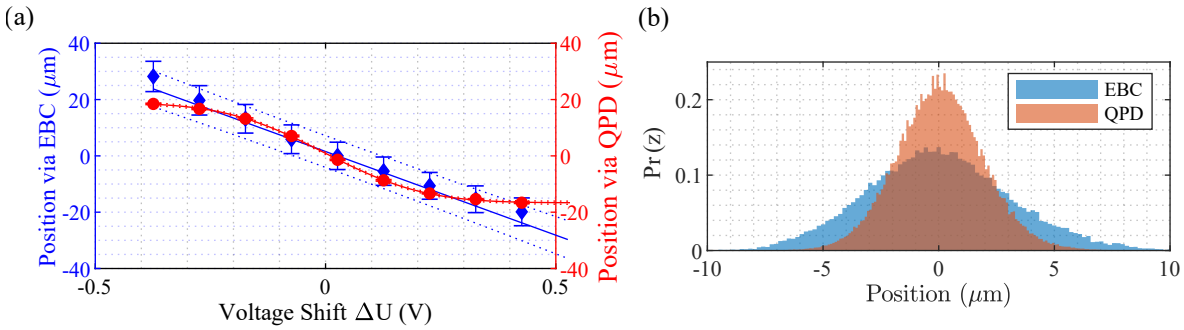

Fig. 3.6 (a) Average position of a levitated microparticle in response to a potential difference across the endcap electrodes. It is evident that the response of the EBC (blue) is linear across the full range of motion, whereas the QPD (red) responds non-linearly at large displacements. (b) Position probability histogram for the motion of a levitated microparticle, recorded by the EBC (blue) and QPD (red), where it is evident that the QPD cannot pick up large displacements.

Levitated particles provide an ideal system for probing stochastic thermodynamics [87]. This is in part due to the characteristic energy of the system being comparable to that of thermal fluctuations of the bath, which enable levitated systems to be highly sensitive to surrounding fluctuations. The coupling to the bath is characterized by the ratio of its oscillation frequency ω_z to its momentum damping rate Γ, yielding overdamped ($\Gamma \gg \omega_z$) and underdamped ($\Gamma \ll \omega_z$) regimes. In the overdamped regime, trapped particles have been used for studying heat engines [100], non-thermal baths [101], and for testing Landauer's principle [102]. In the underdamped regime, the studies in stochastic thermodynamics have

been extended to observing Kramer's turnover [103], studying non-equilibrium Landauer's principle [104] and testing fluctuation-dissipation theorems [105].

Often when such systems exhibit non-equilibrium dynamics, they go beyond the linear detection regime of photodiode-based detection systems, and CMOS cameras would need a large ROI to capture the dynamics, at the expense of bandwidth. In our experiments, the maximum frame rate of the CMOS camera will drop from about 800 fps to 320 fps while maintaining a comparable ROI to detect particle motion compared to EBC.

To further characterise the capability of EBI, and the GTA of the EBC, we cause random jumps in the particles' position with varying time intervals, τ.

Random jumps in position of the particle are implemented by applying telegraph noise statistics which is outside of scope of the thesis. These random jumps, as seen in fig. 3.7(a), are driven by voltage changes applied to the endcap electrodes which follow telegraph noise statistics distributed about a mean waiting time $\bar{\tau}$. For fast switching times relative to the gas damping rate Γ_0, the position probability distribution of the particle is Gaussian, and for slow switching times it is bimodal, as shown in fig. 3.7(b). Comparing to fig. 3.6(a), the particle's motion would go deep into the non-linear range of the QPD. However, the EBC has no such limitation, and position shifts greater than 100 μm are tracked, without compromising on position sensitivity, which is approximately 30 nm Hz$^{-1/2}$ in this work for both devices, as can be extracted from fig. 3.5(b). For the QPD to track such a range of motion, one would have to use a lower magnification imaging system, with a corresponding reduction in position sensitivity.

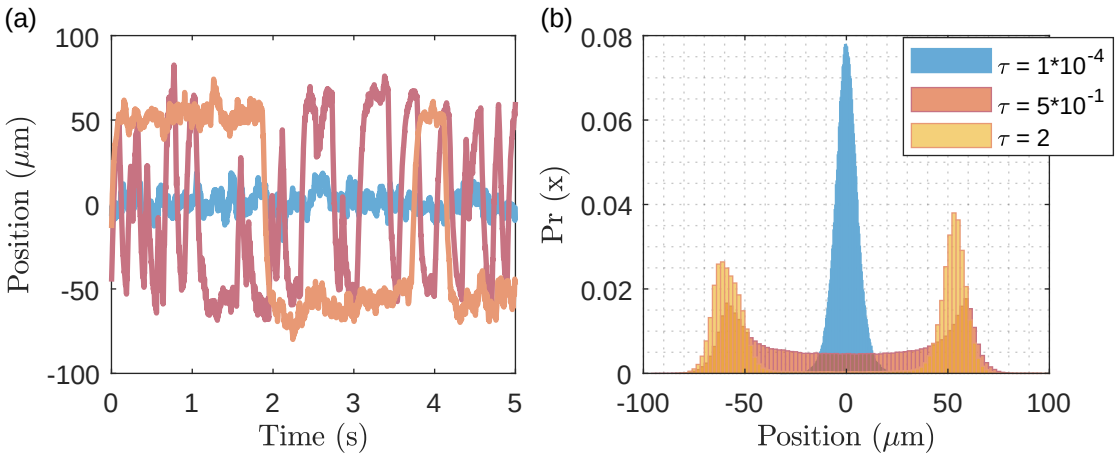

Fig. 3.7 (a) Particle motion, as tracked by an EBC, when the particle is driven to make large jumps in position. Different coloured lines indicate different jump time-constants τ. (b) Position probability distributions for different jump time-constants. As predicted, when $\tau = 1 \times 10^{-4}$ s, the distribution is Gaussian, and for slower jump time-constants the distribution is bimodal.

The factor limiting the bandwidth of our EBC is the GTA which is with 1 kHz frame rate. For shifts in position that are in quick succession and large in displacement, the GTA lags behind or misses consecutive shifts. This is illustrated in fig. 3.7(a), where the GTA of the EBC faithfully tracks the particle position when $\bar{\tau} > 1$ s. For shorter mean waiting times, $\bar{\tau} < 500$ ms the GTA struggles to track the jumps, as evidenced by apparent spikes in the time domain signal. The GTA doesn't represent a true bandwidth limit to EBI and advantageously, as shown in fig. 3.7(b), our EBC can simultaneously track large displacements and the smaller oscillations of the particle about its equilibrium position.

3.3.3 Multi-particle tracking

We extend our study to multi-particle tracking using EBI. The ability to track arrays of particles would enable the study of quantum correlations [106–109], non-hermitian systems [110], and the detection of dark matter [111, 89], vacuum friction [112] and differential force-sensing [97]. To date, few have experimentally explored multi-particle physics, with only two particles trapped to demonstrate state-swapping and sympathetic cooling [113], dipole-dipole [95, 114] and coulomb-coulomb [115] interactions, and cold damping and state control [116].

Motional detection of individual particles in a multiple particle trap is a non-trivial problem. A single focused light beam can carry motional information of two particles [117], or an additional beam can be added for detection of the second particle [95]. Going beyond two particles in this way would require a complex and non-scalable optical setup. Within the context of optical tweezers, there are numerous approaches most suited to tracking multiple particles, using high-speed cameras [118] and multiple-beams in conjunction with a QPD [119], but these detection methods face the same limitations outlined earlier in this chapter.

Figure 3.8(a) shows an image of two microspheres of $5\,\mu$m diameter trapped in a Paul trap, captured on our EBC. The image shows the bounding boxes which the GTA uses to track the two-dimensional position of the particles, labelled "986" and "987".

The levitated microspheres are tracked and their motional information separately reconstructed in fig. 3.8(c). We observe oscillation frequencies of both particles independently. For particle ID= 986, the motional frequencies are $\{\omega_x^{986} = 2\pi \times 68$ rad s^{-1}, $\omega_y^{986} = 2\pi \times 114$ rad s^{-1}, $\omega_z^{986} = 2\pi \times 108$ rad s$^{-1}\}$, whilst particle ID= 987 has frequencies $\{\omega_x^{987} = 2\pi \times 20$ rad s^{-1}, $\omega_y^{987} = 2\pi \times 122$ rad s^{-1}, $\omega_z^{987} = 2\pi \times 184$ rad s$^{-1}\}$ with an approximate uncertainty of $2\pi \times 0.1$ rad s^{-1} . The positions of the two particles have diffrent geometrical factors which explain why these frequencies are similar in y axis and very different in x and z axis. We observe all three centre-of-mass degrees-of-freedom due to imperfect alignment between the coordinate axis of the Paul trap and our imaging

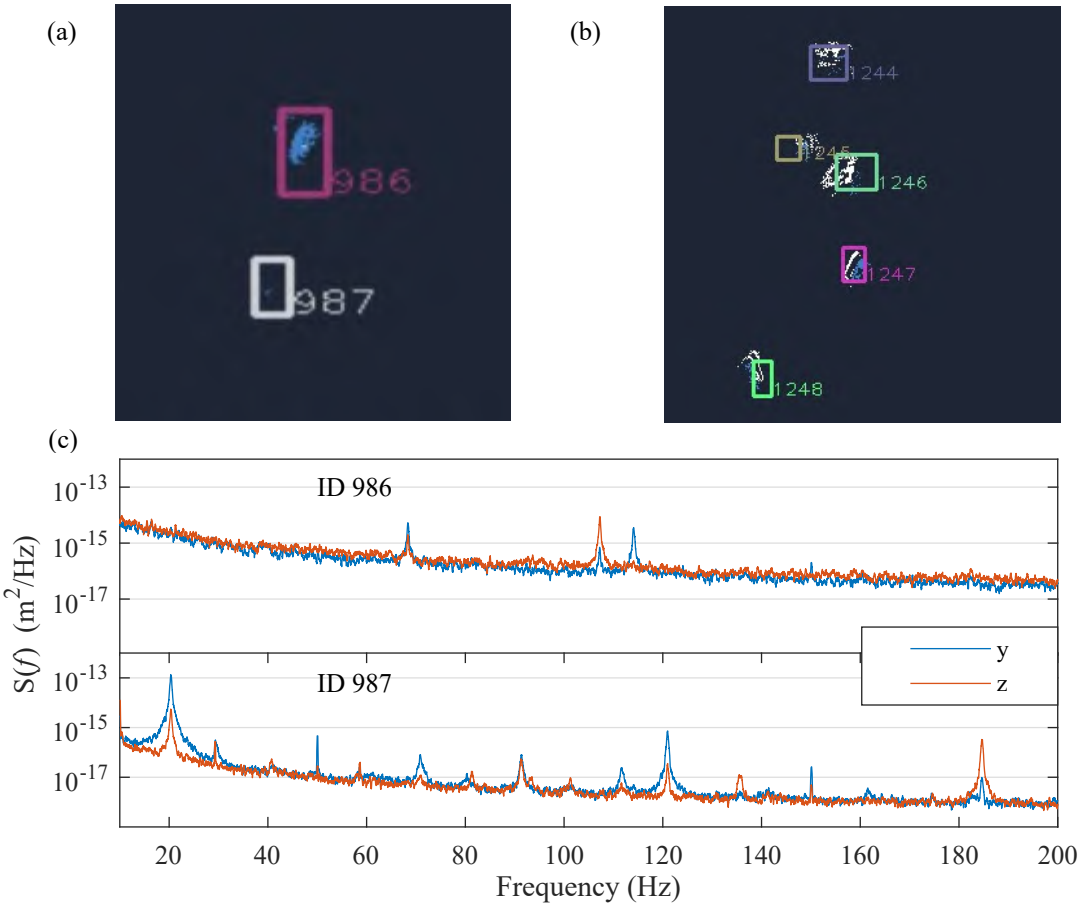

Fig. 3.8 (a) EBC image of two microspheres of 5 μm diameter trapped in a Paul trap. The image shows the bounding boxes which the GTA uses to track the two-dimensional position of the particles, labelled "986" and "987". (b) EBC image illustrating tracking of five particles. (c) PSDs reconstructed from the output of the GTA for the particles in (a).

system. The additional frequency components in the spectrum for ID 987 could be other degrees-of-freedom (e.g. librational) or evidence of multi-particle collective modes, but that is beyond the scope of this study.

The EBC is not limited to tracking two particles, and in fig. 3.8(b) we show that the GTA has identified 5 separate particles. Due to varying Q/m, each particle has different resonant motional frequencies, and hence it is possible to individually excite them. Figure 3.9 shows the motion of the two particles with 108 Hz mode excited after we give an AC signal to one of the DC electrodes with 108 Hz frequency and $V_{\mathrm{rms}} = 0.04$ V amplitude. Compared to fig. 3.8(c), we can witness that the area beneath the peak of z-axis mode increases as for particle with ID= 986. At the same time, there is an obvious 108 Hz peak in the PSD of particle with ID= 987 due to the interaction of the two charged particles. If we set the exciting frequency to 114Hz to excite the y motion mode of particle labelled with "986",

similar trend can be observed in fig. 3.10 in comparison to fig. 3.8(c). We believe this opens the door to the study of a wide range of non-equilibrium phenomena.

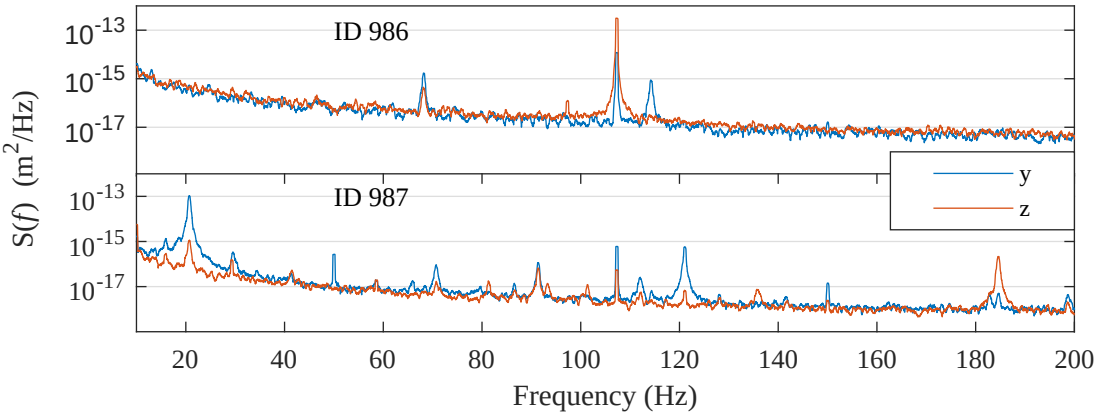

Fig. 3.9 PSDs reconstructed from the output of the GTA for the particles labelled with "986" and "987" with an AC signal added to one of the DC electrodes of 108 Hz frequency and $V_{\mathrm{rms}} = 0.04$ V amplitude.

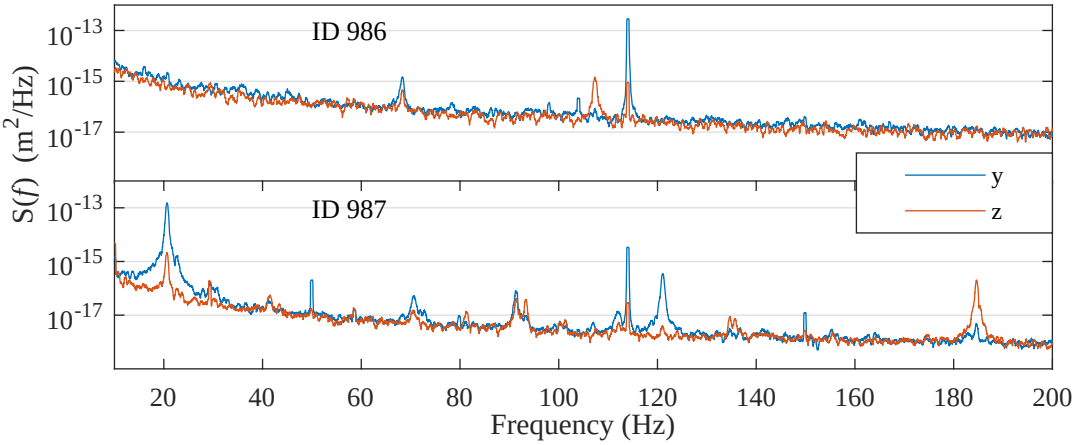

Fig. 3.10 PSDs reconstructed from the output of the GTA for the particles labelled with "986" and "987" with an AC signal added to one of the DC electrodes of 114 Hz frequency and $V_{\mathrm{rms}} = 0.04$ V amplitude.

In conclusion, we have shown that EBI is an interesting alternative to conventional detection schemes used for tracking levitated particles. The key enabling feature of EBI is the low data transfer, which enables EBC to track multiple objects at higher speeds than conventional cameras, and when combined with natural low pixel latencies [98] will allow the experimenter to implement real-time feedback for state control. In this study,

the bandwidth of tracking is limited to 1 kHz by the very general and proprietary GTA employed. The underlying dynamics of our system are well known, therefore a more precise filter, like an asynchronous Kalman filter [120, 121] in which we can input the expected equation of motion, will enable faster and more accurate tracking.

As compared to photodiode-based detection schemes, EBCs feature a dynamic ROI, enabling tracking over a wide field-of-view, with particular application in the study of non-equilibrium physics. We have demonstrated tracking over 100 micrometres whilst retaining $30\,\mathrm{nm\,Hz^{-1/2}}$ resolution. Finally, we have introduced an imaging technique suitable for fast tracking of a large number of particles, reaching MHz rates with the application of tailored particle tracking algorithms.

Chapter 4

Linear feedback cooling of an array of levitated microparticles

The purpose of this chapter is to realize the real-time position output of levitated microparticles from the event-based imaging detection (see Chapter 3), and cool the motion of an array of charged microparticles in the Micro-Paul trap.

4.1 Introduction

Levitated nanoparticles and microparticles, when subjected to optical [122–124], electric [125, 40, 33], or magnetic [126–128] fields, offer a compelling testbed that allows for the investigation of nanoscopic and microscopic thermodynamics [129, 130, 87], high-precision sensing [131–133], and the exploration of quantum phenomena [134, 135, 16] in an isolated system. By manipulating the levitation fields, it becomes possible to control and finely tune the motion of mesoscopic particles [41].

Paul traps are a well-established method for generating confining potentials that exhibit advantageous properties, including great trap depth (approximately 1 keV [43]), and large trapping regions (approximately 1 cm^3 [17]). Furthermore, Paul traps as compared to optical traps reduce the motional decoherence by random photon scattering [18] and internal heating of levitated particles [136]. Recent research has increasingly focused on the investigation of multiple levitated nanoparticles or microparticles [114, 115]. Arrays of levitated mesoscopic particles have advantages in enhancing the detection of dark-matter candidates [137, 111], verifying the quantumness of gravity via entanglement [27, 138] and suppressing noise heating via inducing non-CoM modes of motion [139].

The cooling of the CoM motion of levitated particles can prevent particle loss in high vacuum [140], improve measurement sensitivity of weak forces [141, 56] and enable investigations to enter the quantum regime [12]. Several techniques have been employed

to achieve the CoM motion cooling of trapped mesoscopic particles including direct feedback cooling [17, 116], cavity-assisted resolved-sideband cooling [37, 63, 16] and sympathetic cooling [142, 113]. Sympathetic cooling is not only possible in Paul traps, and can happen to two coupled uncharged particles via scattered light or cavity within optical traps. Direct feedback cooling involves linear velocity damping [59, 67, 116] and non-linear parametric feedback cooling [57, 143, 144]. In the context of Paul traps, effective cooling based on an integrated optical cavity [63] resulted in a greater than 1000-fold temperature reduction. Cooling via velocity damping of a charged dielectric particle using electric field is reported to achieve temperatures on the order of a few millikelvins [17]. A comparative analysis between parametric and velocity feedback damping methods was performed [42] to illustrate that velocity damping cools an oscillator to a temperature an order of magnitude lower in comparison to parametric cooling and is more resilient to imperfect experimental conditions in a Paul trap setup. Furthermore, a demonstration of imaging-based velocity feedback cooling of a levitated nanoparticle in a Paul trap was presented [67]. Sympathetic cooling of two levitated particles in Paul traps are recently reported to show that the cooling of one levitated particle through direct feedback leads to the cooling of a second particle according to the Coulomb interaction between the charged particles [113, 142].

In this chapter, our objective is to implement linear feedback cooling on an array of charged microparticles levitated within a Paul trap. The experiment utilizes an event-based camera (EBC) (see Chapter 3) to capture the motion of the particles, while a Field Programmable-Gate-Array (FPGA)-based system is employed to convert the data from the camera into a feedback force onto nearby electrodes. EBCs are a new technology enabling simultaneous rapid tracking of the motion of multiple objects, which could be used in the construction of sensor-arrays. Initial experiments have achieved a four-fold reduction in the temperature of a single particle at 2×10^2 mbar, and future work will concentrate on multi-particle cooling.

4.2 Theory of feedback cooling

4.2.1 Theory of velocity damping cooling

The three axes of motion in the Paul trap are uncoupled for the small motion of amplitudes we have in this work. In order to analyse the dynamics of the trapped particle, the one-dimensional Langevin equation is utilized to describe the dynamics in the z-axis for

example [145]

$$\ddot{z}+\Gamma_0\dot{z}+\omega_z^2 z=\frac{F_{\mathrm{fluct},z}}{m}+\frac{F_{\mathrm{ext}}}{m}, \tag{4.1}$$

where ω_z (with unit rad/s) is the mechanical oscillation frequency of the particle along the z axis, Γ_0 is the friction coefficient or damping rate, $F_{\mathrm{fluct},z}$ is a stochastic force and F_{ext} is an externally applied force.

When we feedback a Coulomb force which is proportional to the charged particle's velocity, this is called velocity damping or cold damping. Equation 4.1 along z axis is then modified as [42]

$$\ddot{z}+\Gamma_0\dot{z}+\omega_z^2 z=\frac{F_{\mathrm{fluct},z}}{m}-\gamma_{fb}\left(\dot{z}+\delta\dot{z}\right), \tag{4.2}$$

where γ_{fb} is the damping rate due to feedback signal, $\delta\dot{z}$ is a stochastic noise added by the feedback signal where detection noise dominates. According to the equipartition theorem, the CoM temperature of the trapped particle can be indicated as

$$T_{\mathrm{CoM}}=T_0\frac{\Gamma_0}{\Gamma_0+\gamma_{fb}}+\frac{1}{2}\frac{m\omega_z^2}{k_B}\frac{\gamma_{fb}^2}{\Gamma_0+\gamma_{fb}}S_{nn}, \tag{4.3}$$

where S_{nn} is feedback noise from detection defined by a constant spectral noise density and the second term is a part from the detection noise which will cause heating after being fed back to trapped particle. This will cause a phenomenon called noise squashing [146–148]. When it happens, correlations between detection noise and particle motion will make the spectrum of particle oscillating motion appear to be cooled below the noise floor. In the limit, $\gamma_{fb}\gg\Gamma_0$, the optimum feedback gain is given by

$$\gamma_{fb}=\sqrt{\frac{2\Gamma_0 k_B T_0}{S_{nn}m\omega_z^2}}, \tag{4.4}$$

with a minimum temperature expressed as

$$T_{\mathrm{CoM}}=\sqrt{\frac{2S_{nn}m\omega_z^2\Gamma_0 T_0}{k_B}}. \tag{4.5}$$

In our setup, take the data in Figure 4.7 as an example, S_{nn} is about 10^{-16} m^2/Hz, $\omega_z=(174.30\pm0.03)\times2\pi$ rad/s, $\Gamma_0=0.63\pm0.01$ Hz at 2×10^{-2} mbar and the centre-of-mass temperature is $T_0=800\pm200$ K with feedback cooling switched off. We can estimate the minimum temperature at 2×10^{-2} mbar is about 34 ± 3 K according to Equation 4.5, which is slightly lower than the minimum temperature we achieve 90 ± 20 K in the cooling

experiment which could be due to imperfect phase. Pumping the Paul trap system to lower pressures allows to farther cool the CoM motion of the levitated particle. At the 8×10^{-4} mbar, the centre-of-mass temperature is cooled to $T_0 = 2 \pm 1$ K.

4.3 Feedback cooling of levitated microparticles

Velocity damping cools the CoM motion of a levitated particle via adding a drag force which is proportional to the particle velocity. Compared to parametric feedback cooling, velocity damping is illustrated to cool an oscillator to a temperature an order of magnitude lower and more resilient to imperfect experimental conditions [42]. Therefore, in this study we adopt velocity damping to conduct feedback cooling exploration.

4.3.1 Schematic of experimental setup

A schematic diagram in Figure 4.1 depicts the whole process of our feedback cooling experimental setup. Two pairs of diagonal electrodes provide AC signals and DC signals separately, which help to confine particles in x-y plane. Two endcap electrodes provide static field to confine particle motion along axial direction namely z axis in this setup. The LIAD [43] method is adopted to launch 5 μm-diameter silica particles deposited on a thin aluminum sheet into trap centre. The sheet we employed is 0.4 mm-thick. Levitated microparticles are trapped in a linear Paul trap and then illuminated by a green laser with $\lambda = 520$ nm wavelength and P = 18 mW output power. The scattered light from the particle is then collected by a microscope and imaged onto an EBC or QPD. In order to feedback signals to trapped particles, a FPGA system is utilized to output the particle position signal from the EBC in real time. Our EBC and the FPGA system are both connected to a computer. Via programming on computer with Python in Linux environment, we successfully drive the FPGA system to output real-time position signal from EBC detection with one output channel. At the same time, the FPGA also conducts a derivation algorithm to the position signal, attenuates the signal to a proper amplitude which has a similar scale of position amplitude and outputs with the other channel. Therefore, an amplitude-adjusted velocity signal is fedback to one of DC electrodes to cool levitated microparticles.

4.3.2 Feedback cooling of one particle

Our EBC product is provided by Prophesee company with module EVK1 -Gen3.1VGA (camera sensor: Prophesee PPS3MVCD, 640×480 pixels). The camera is connected with a computer via a USB 3.0 port. The sequence of output event frames along with some statistics can be visualized from a company-provided Graphical User Interface, and then

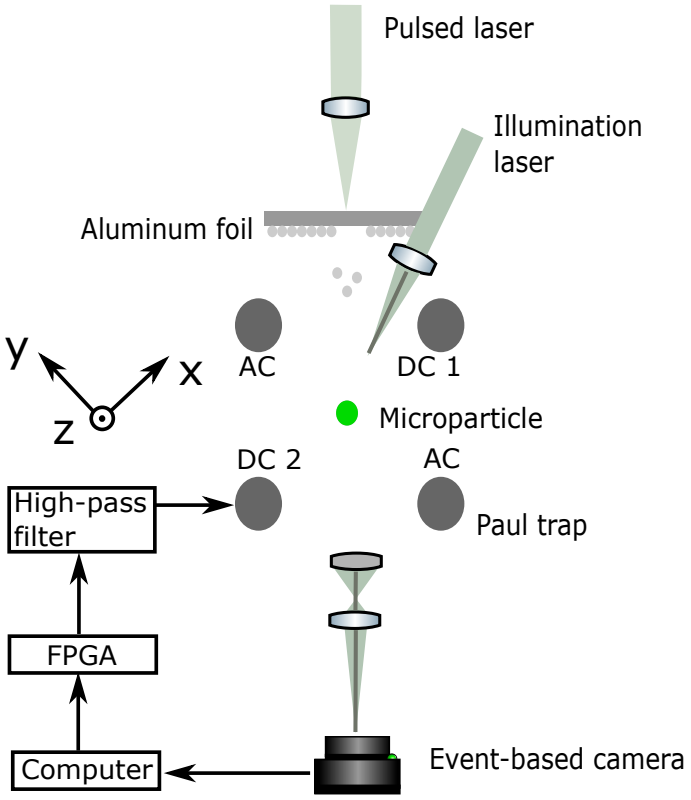

Fig. 4.1 Schematic of the feedback cooling experiment. LIAD method is used to launch 5 μm-diameter silica particles deposited on a thin aluminum sheet. An illumination laser at 520 nm is focused on the particle, and Event-Based camera placed at the bottom of chamber detects the particle motion. The FPGA helps to derive velocity signal of particle and feedback it to cool the motion of microparticle. The EBC and FPGA system are both connected to a computer.

saved as a video or a CSV file in computer. After confirming with the camera company technical support that there is no ready-to-use tool to output the stream of events in real time, we begin our work with employing a FPGA system to realize the real-time output of detected events from the event-based camera. The FPGA system we adopted is Red Pitaya STEMlab 125-14 [149]. The system has Xilinx Zynq 7010 FPGA and supports two 125MSps 14-bit inputs and two 14-bit outputs. It can be controlled remotely using LabVIEW, MATLAB, Python, or Scilab and works with Linux or Windows PC. Our EBC is operated in Linux environment and programmed with Python, which makes this type of FPGA system suitable for this aim.

A pipeline is shown in Figure 4.2 to indicate how the FPGA system works to output the motion signal of the particle. EBC sensor detects the events of light contrast caused by particle motion and store these events in event buffer. After noise filter and trail filter are applied to these events, frames of the data are generated. Via the GTA, the detected object is recognised and the position signal of the particle will be sent to a computer and then the computer will drive the FPGA system to output the position signal. Clock synchronization of the FPGA clock and the EBC clock is achieved via citing EBC clock only. Because the position output of the EBC has large absolute values with unit pixel, the FPGA system obtains an equilibrium position of the particle firstly and then outputs the relative position with the unit Volt. The procedures from Event Buffer to Data Acquisition are within an iteration loop to keep the particle position signal detected.

In our initial attempts to drive FPGA to output the position signal of the levitated particle in real time, we find that there is always an obvious time delay from the EBC outputs to the FPGA outputs. We find out that the delay time is partly from the EBC data saving within computer and partly from the iteration loop period time expanding.

Figure 4.3 shows the two situations which cause time delay to FPGA outputs. In Figure 4.3(a), a distinct and consistent flat output signal can be observed during the time interval from 234 s to 235 s. Figure 4.3(b) depicts the motion spectrum of the trapped particle along z axis. The blue and red lines represent PSDs from the EBC and FPGA output respectively. The peak frequency from the EBC spectrum is 109 Hz while the motion frequency from the FPGA is 94 Hz, lower than the real particle motion frequency.

This phenomenon in Figure 4.3(a) arises due to a delay between the Callback and Computer. This is introduced by the EBC processing and saving captured motion data as a CSV file to the computer. Therefore, it will lead to a period where the output signal of the FPGA system remains constant before it resumes its normal behavior. The time delay in Figure 4.3(b) is caused by each iteration loop period expanding beyond 1 ms (frame rate here is 1 kHz). When we set the iteration loop period larger than the reciprocal of frame rate or enable the Frame Generation step, each loop will take more time than the reciprocal of frame rate and causing FPGA output to have time delay.

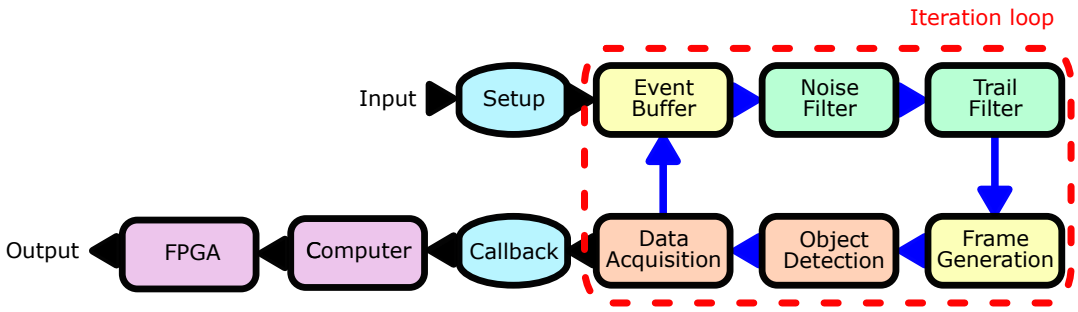

Fig. 4.2 Pipeline information of the FPGA system output based on EBC detection. Motion data of levitated the particle is firstly captured in EBC and then transferred to a computer. The computer obtains the data and drives the FPGA system to output the motion signal. The procedures from Event Buffer to Data Acquisition are within an iteration loop.

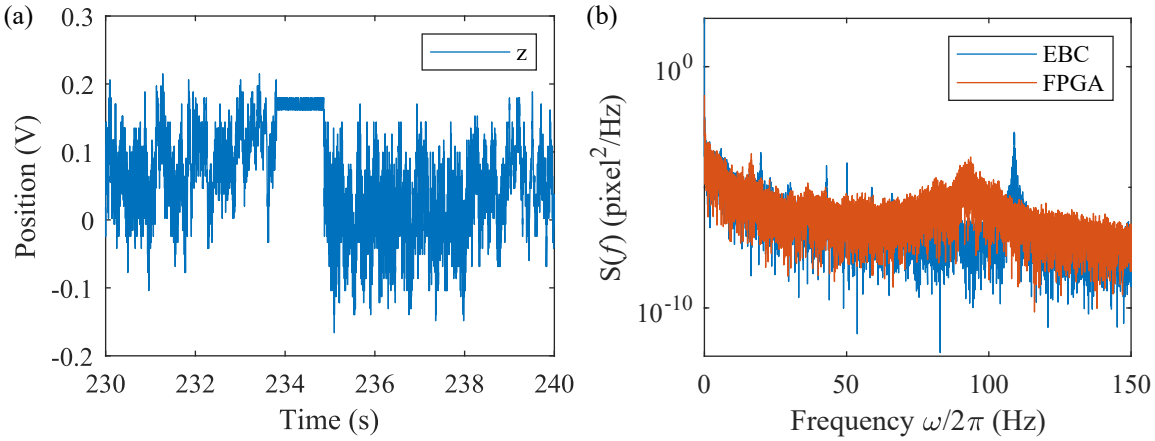

Fig. 4.3 Two situations causing time delay to FPGA outputs. (a) The FPGA time delay caused by captured data saving. (b) The FPGA time delay caused by Iteration loop setting. The blue and red lines represent the motion spectrum of levitated particle along z axis from EBC and FPGA output respectively. The peak frequency from EBC spectrum is 109 Hz while the motion frequency from FPGA is 94 Hz, lower than the real particle motion frequency.

By disabling the camera saving option, optimizing iteration loop settings and disabling the Frame Generation step, the time delay problem of the FPGA output can be solved. Figure 4.4 is an verification of the FPGA outputing signal in real time from the EBC detection. It compares the PSDs obtained from FPGA and EBC outputs. In this experimental setup, AC voltages with frequency $\Omega_{RF} = 2\pi \times 1060\,\mathrm{rad\,s^{-1}}$ and amplitude $V_{RF} = 400\,\mathrm{V}$ are applied. The two endcap electrodes are held at a potential of $U_{DC} = -1.0\,\mathrm{V}$. Two diagonal DC electrodes are independently set to 0 V and 5.1 V, respectively. The measurements are

performed at a pressure of 2×10^{-2} mbar. The setting update frequency is 1 kHz, therefore, a 500 Hz-bandwidth is witnessed. The mechanical motion frequency of trapped particle along z axis is 39 Hz. Signal-to-noise (SNR) obtained from the two methods is close to each other, noise floor from the FPGA is slightly higher than from the EBC below 250 Hz and then gradually goes to the equal level from EBC above 250 Hz.

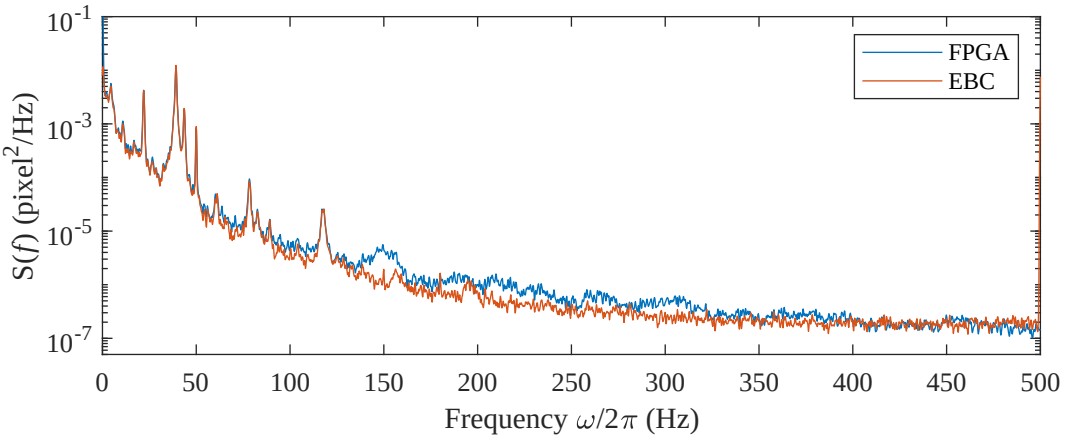

Fig. 4.4 PSDs of FPGA and EBC output along axial axis at 2×10^{-2} mbar. Blue and red curves represent the frequency domain of motion output from FPGA and EBC respectively.

A differentiator is realized within FPGA in this project to aquire the velocity signal from EBC detected position signal. Therefore, we can make sure a feedback signal proportional to velocity is generated. Blue and red lines in Figure 4.5 indicate position and feedback signals. A 90° phase difference is observed between the two curves. Green line is the mathematical derivation obtained from the position signal, exhibiting a phase difference close to 0° in comparison to the feedback line.

To have a good understanding of the feedback cooling scheme, we firstly test the cooling efficiency through a QPD for detection. In order to generate a velocity signal, a FPGA system (National Instruments; model: PXIe-7847) is utilized to realize the derivation algorithm of an input position signal with LabVIEW programming. The diagram in Figure 4.6(a) depicts the input and output signals originating from the FPGA in the time domain and Figure 4.6(b) shows the frequency information. The blue line represents the input sine signal with 0.4 V peak-to-peak voltage and 85 Hz, while the red line represents the output signal. We can notice an obvious close to 90° phase shift between the two lines.

After acquiring the velocity signal, it is possible to achieve the cooling of particle motion by introducing the velocity back into one of the DC electrodes. Figure 4.7 gives typical PSDs at 2×10^{-2} mbar, comparing the situations with feedback cooling switched on and off. After data calibartion, we extracted the CoM temperature of the particle motion along z axis, which dropped from 800 ± 200 K to 90 ± 20 K with feedback cooling

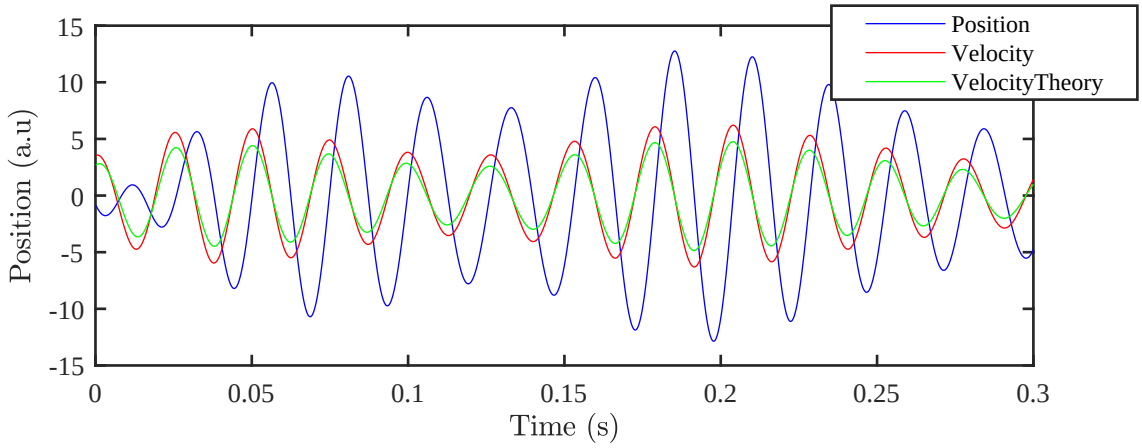

Fig. 4.5 Velocity output from FPGA. Blue and red lines are position signal and corresponding velocity signal from two output channels of FPGA. For comparison, a green line is calculated theoretically to show velocity signal is obtained.

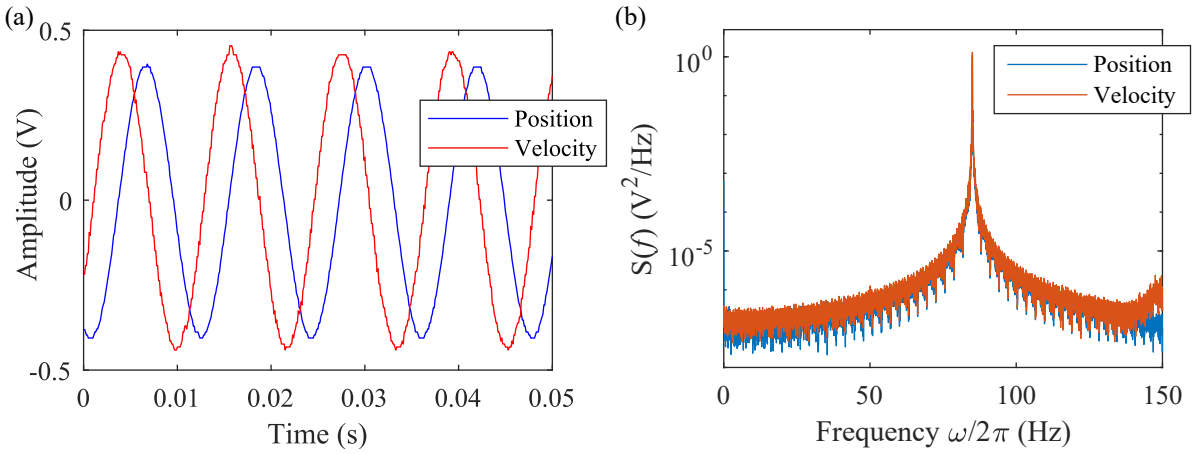

Fig. 4.6 The velocity output test from FPGA. (a) The input and output signals originating from the FPGA in time domain. (b) The PSDs of input and output signals from the FPGA. The blue and red lines are the input and output signals of FPGA separately. An expected close to 90° phase shift between the two lines can be noticed.

switched on. The minimum CoM temperature is limited by the imperfect phase and the heating due to gas collisions at relatively low vacuum.

PSDs with different feedback gains are further obtained, in which feedback gain set to 0 means that there is no feedback signal. According to a Lorentzian function fitting [16] (More information can be found in Section 2.4.4) peaked at mechanical motion frequency, CoM temperature is able to be extracted. In Figure 4.8, when there is no feedback signal, data shows the CoM temperature of particle is 800 ± 200 K, which is higher than room temperature (300 K). This could be due to electric noises originated from high voltage amplifier. When the feedback signal is switched on, the CoM temperature dropped to

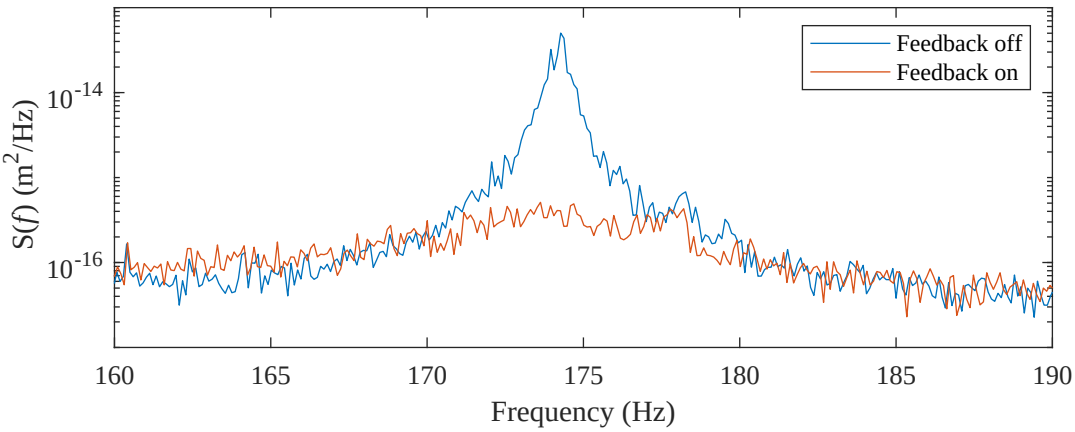

Fig. 4.7 Typical PSDs along z axis with and without feedback based on QPD detection at 2×10^{-2} mbar. The motion frequency along axial axis is 174 Hz. Blue curve corresponds to the particle motion with feedback cooling switched off. After calibration, the CoM temperature of levitated particle dropped from 800 ± 200 K to 90 ± 20 K with feedback cooling switched on.

190 ± 40 K. After taking the derivative of the position signal, the obtained velocity signal will be multiplied by ω time and ω indicates the motion frequency with unit rad/s. In this situation, $\omega = 2\pi \times f_z = 1.1 \times 10^3$ rad/s. Therefore, we set feedback gain smaller than 1 (at 1×10^{-3} scale) to tune the amplitude of feedback signal. With feedback gain increasing, the CoM temperature goes lower reaching a minimum temperature at 90 ± 20 K at feedback gain set at 0.004 and then the temperature fluctuates around this value. This indicates that the detection noises in feedback signal causes heating of the particle along with cooling. Figure 4.8(b) shows the extracted damping rate grows with feedback gain increasing.

Feedback cooling based on EBC detection is then conducted. The PSDs measurements depicted in Figure 4.9 is taken at 2×10^{-2} mbar with feedback cooling on and off. The observed motion frequency is 65 Hz.

According to setting the gain of feedback signal from 0.0001 to 0.0008 with 0.0001 interval, different PSDs at 2×10^{-2} mbar are obtained shown in Figure 4.10. Here, with the increase of feedback gains, the peak values at motion frequency show a decreasing trend. The observed maximum gain, as depicted in the image, is determined to be 0.0008, which is about 8 times of the particle position amplitude. This value is constrained by the occasion where the particle experiences heating along the y axis while simultaneously undergoing cooling along the z axis due to disparate phases of motion along these two axes.

After calibration, total damping rates of the levitated particle under different feedback gains are obtained shown in Figure 4.11(b). After Lorentzian function fitting, the centre-of-

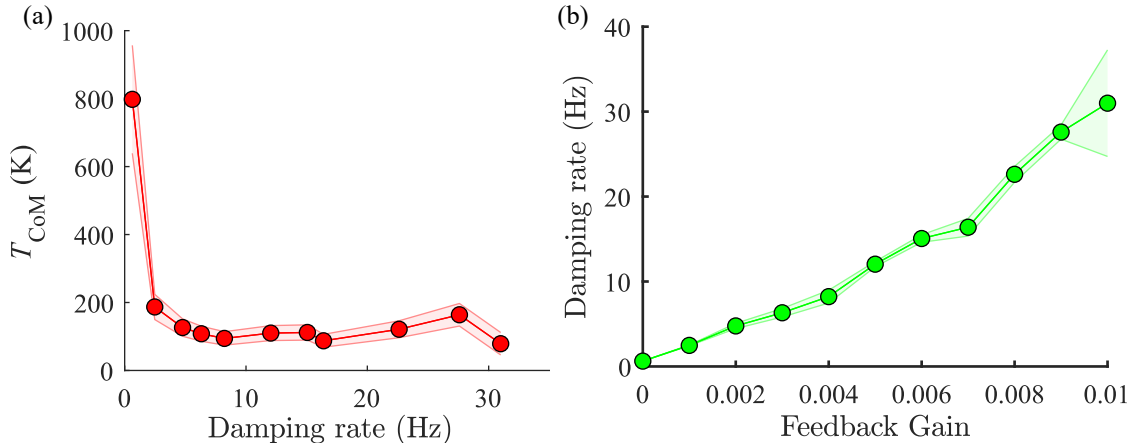

Fig. 4.8 Feedback cooling of one particle based on QPD detection. (a) The trend of CoM temperature of the particle motion and total damping rate. (b) The trend of total damping rate and feedback gain. The damping rate increases when setting feedback gain becomes larger. Temperature and damping rate error bars are derived via Lorentzian function fitting uncertainty and correspond to 1 standard deviation.

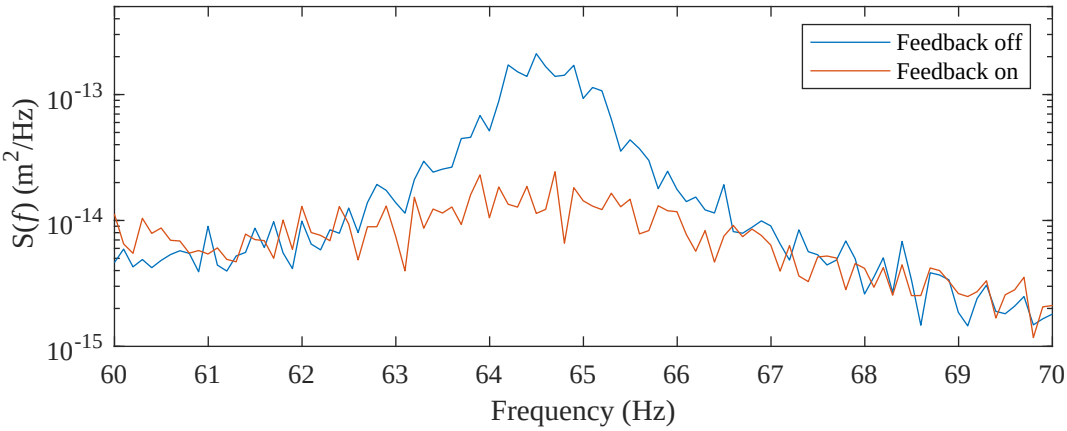

Fig. 4.9 Typical PSDs with and without feedback based on EBC detection at 2×10^{-2} mbar. The motion frequency along axial axis is 65 Hz. Blue curve corresponds to the particle motion with feedback cooling switched off.

mass temperature trend with damping rate is observed in Figure 4.11(a). The Temperature is 900 ± 200 K with feedback cooling switched off and it decreases to the minimum temperature of 220 ± 50 K when damping rate reaches 4.4 ± 0.5 Hz. Further increment of feedback gain doesn't help cool the levitated particle to a lower centre-of-mass temperature. During feedback cooling, not only the particle's velocity signal but also noises caused by detection will be fed back to the particle. Further improvement will be focused on conducting cooling experiments at lower pressures which will help to decrease the heating due to gas collision.

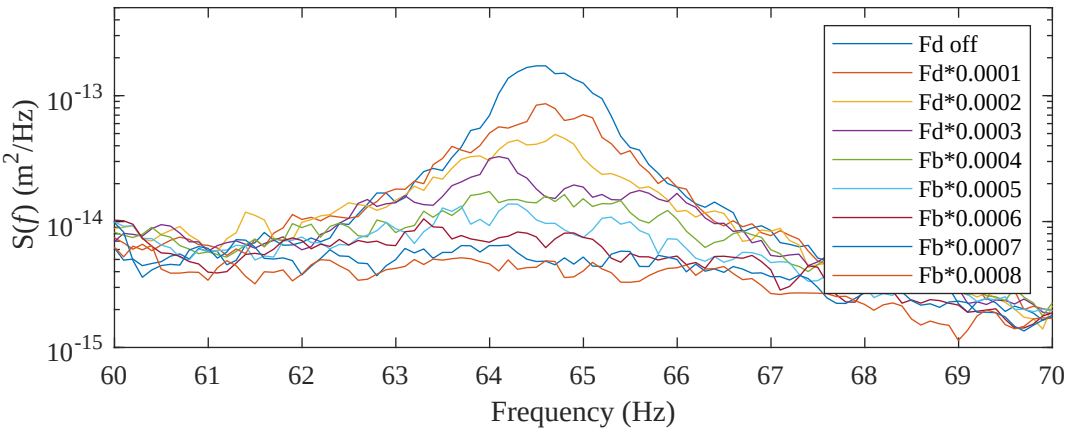

Fig. 4.10 PSDs with different feedback gains from 0.0001 to 0.0008 based on EBC detection at 2×10^{-2} mbar. The motion frequency along axial axis is 65 Hz. Blue curve corresponds to the particle motion with feedback cooling switched off. The observed maximum feedback gain is determined to be 0.0008, which is constrained by the occasion where the particle experiences heating along the y axis while simultaneously undergoing cooling along the z axis.

Cooling effect of the levitated particle is not only determined by the amplitude of feedback signal but also the phase of the signal. Phase shift is now achieved via a FPGA system, which is shown in Figure 4.12. A sine wave signal with 100 Hz and 0.3 V amplitude is connected to FPGA input for test. Blue and red lines represent input and output signals of FPGA. Figure 4.12(a) corresponds to 15° phase shift and Figure 4.12(b) corresponds to 45° phase shift.

Then the feedback cooling experiments with different feedback phase are carried out. Figure 4.13 shows the detailed trend of CoM temperature of particle motion and extra phase of feedback signal. The phase interval between each data is 30°, and the CoM temperature of levitated particle is 800 ± 200 K with feedback cooling switched off. When the feedback signal is added to the trap system, T_{CoM} drops to 700 ± 200 K and then goes up to a maximum value of 1900 ± 500 K with extra phase reaching 180°. Because we don't want to have a gain coefficient too high for the out-of-phase heating, the minimum temperature here is higher than in the previous example in Figure 4.11. The CoM temperature goes down with the extra phase increasing from 180° to 360°. Define the extra phase as ϕ, the CoM temperature is expressed as [17]

$$T_{\mathrm{CoM}} = \frac{\Gamma_0 T_0}{\Gamma_0 + \gamma_{\mathrm{fb}} \cos(\phi)}. \tag{4.6}$$

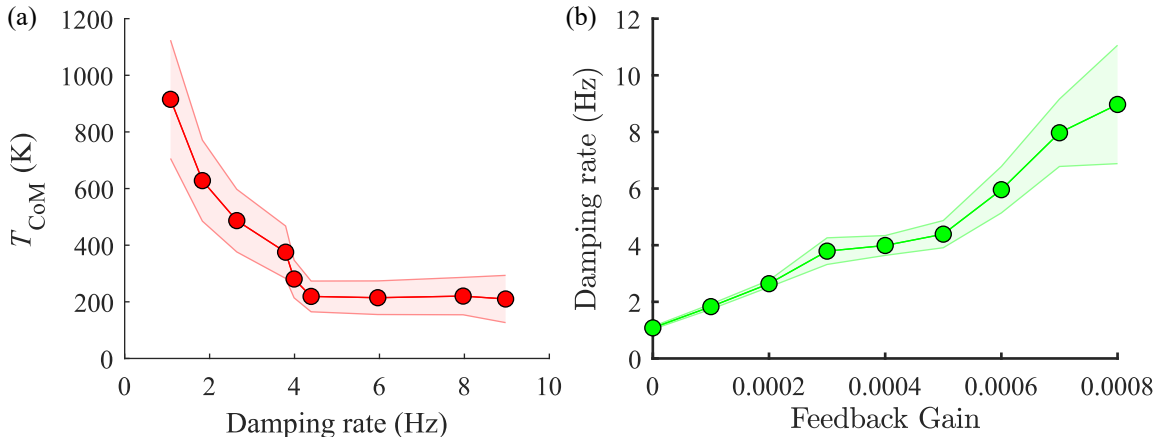

Fig. 4.11 Feedback cooling of one particle based on EBC detection. (a) The trend of the motional temperature and total damping rate. (b) The trend of the total damping rate and feedback gain. Temperature and damping rate error bars are derived via Lorentzian function fitting uncertainty and correspond to 1 standard deviation.

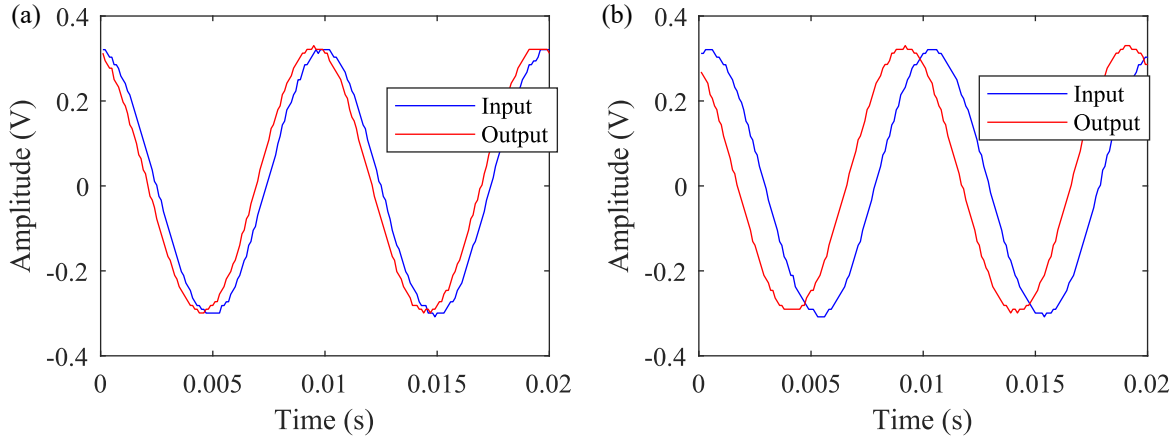

Fig. 4.12 Phase shift manipulated by FPGA. A sine wave signal with 100 Hz and 0.3 V amplitude is input to FPGA, indicated as blue line and the output signal is represented as red line. (a) 15° phase shift. (b) 45° phase shift.

Considering the slight phase shift caused by feedback wires or other devices and the uncertainty of T_0, we revise the Equation 4.6 to be

$$T_{\mathrm{CoM}} = \frac{\alpha \Gamma_0 T_0}{\Gamma_0 + \gamma_{\mathrm{fb}} \cos(\phi + \phi_0)}. \tag{4.7}$$

where α is a constant related to the uncertainty of T_0 and ϕ_0 is the phase shift caused by wires or other devices. The curve in Figure 4.13 is fit to Equation 4.7 with α, γ_{fb} and ϕ_0 are the three free parameters. The fitted result of ϕ_0 is 3°, which means the cooling effect should be optimized via extra phase shift reaching 357°.

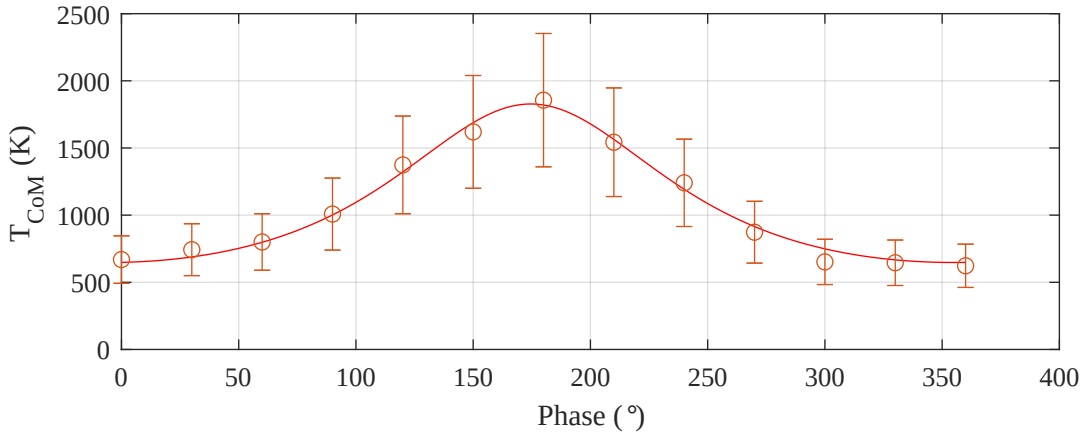

Fig. 4.13 The trend of CoM temperature of particle motion and extra phase of feedback signal. Data is taken at 4×10^{-2} mbar.

4.3.3 Feedback cooling of multi-particles

The event-based imaging technique, as a novel detection method in levitated nanoparticles and microparticles, allows for the simultaneous tracking of motion in multiple particles. This property enables the cooling of the motion of multi-particles at the same time. Multiple particle cooling will not only pave a way for quantum entanglement and correlations [150, 106, 107], but also facilitate the detection of weak forces [108].

Figure 4.14(a) shows the image of two microspheres tracked from CMOS camera and EBC respectively. The two particles on the EBC are with different colour box, labelled 48 and 58. Figure 4.15 is the related PSDs from the EBC of the two microparticles along z axis. In comparison to clear one or two peaks of one-particle spectrum, more motion peaks are observed indicating that there exists an interaction between the two charged particles.

The initial focus of this research is directed towards the achievement of real-time motion output of multiple particles utilizing the FPGA system. Due to the restricted number of available outputs on the Red Pitaya device, a computational approach is employed to combine the positional information of two particles along the z-axis. This involves the summation of the particle positions, followed by the application of computing the Power Spectral Density. By taking the derivative of the position signal, we are able to obtain the combined velocity signals of the two particles. This sum of velocity signals is subsequently utilized as feedback without any filtering and directly applied to one of the DC electrodes of the Paul trap. Spectrums in Figure 4.16 shows the PSDs of the two-particle position summation with feedback on and off.

To obtain a more comprehensive understanding of two-particle cooling, we conducted an investigation involving the adjustment of various feedback gains, as depicted in Figure 4.17. The feedback gains are set to increase from 1×10^{-4} to 5×10^{-4} with an interval

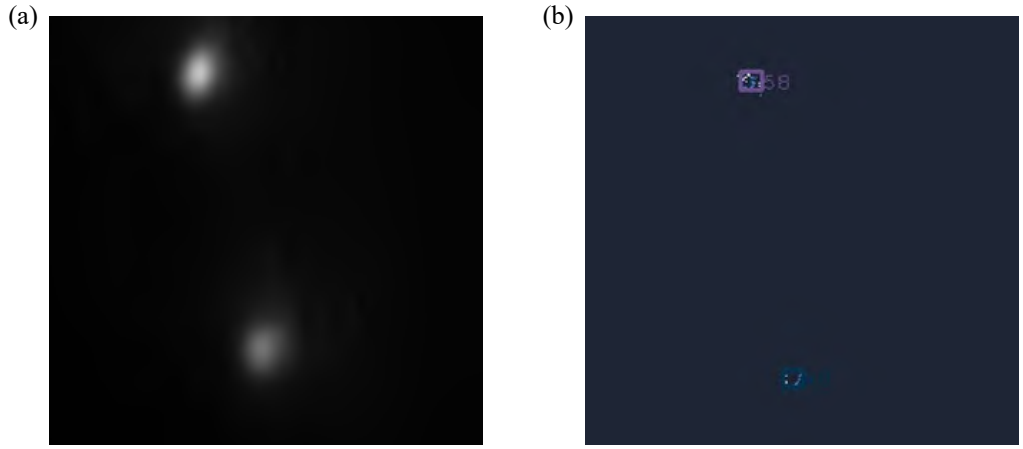

Fig. 4.14 (a) The view from CMOS camera of the two particles at 3×10^{-2} mbar for reference. (b) The EBC view of two levitated microparticles. The upper and lower particles are labelled with ID=58 and ID=48.

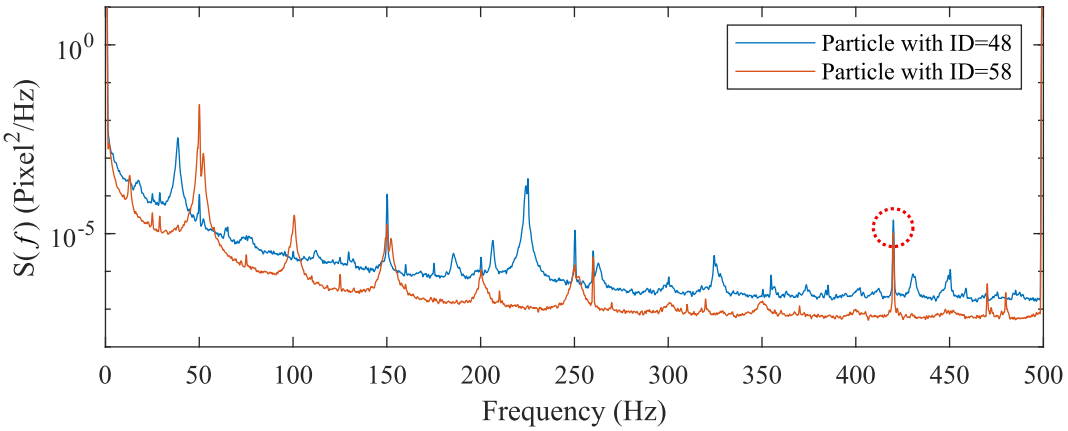

Fig. 4.15 The PSDs of the positions of two particles after computing the Power Spectral Density along z axis. Compared to single levitated particle, more motion peaks can be observed which means there exists an interaction between the two particles. A peak with 420 Hz oscillation frequency labelled with red dashed circle appears on the PSDs of the two particle motion.

of 1×10^{-4}. The experimental data is taken at the pressure of 3×10^{-2} mbar. The obtained spectrum reveals distinct motion peaks that exhibit varied cooling or heating outcomes. For example, the mode with oscillating frequency around 224 Hz shows cooling effect in Figure 4.17(a) but the mode with about 37 Hz shows heating effect in Figure 4.17(b). This should be originated from the phase difference between the detected position signal and the feedback velocity signal and the phase differences are not accurately 90° for all the oscillating modes due to a phase shift between the actual phase and detected phase for each

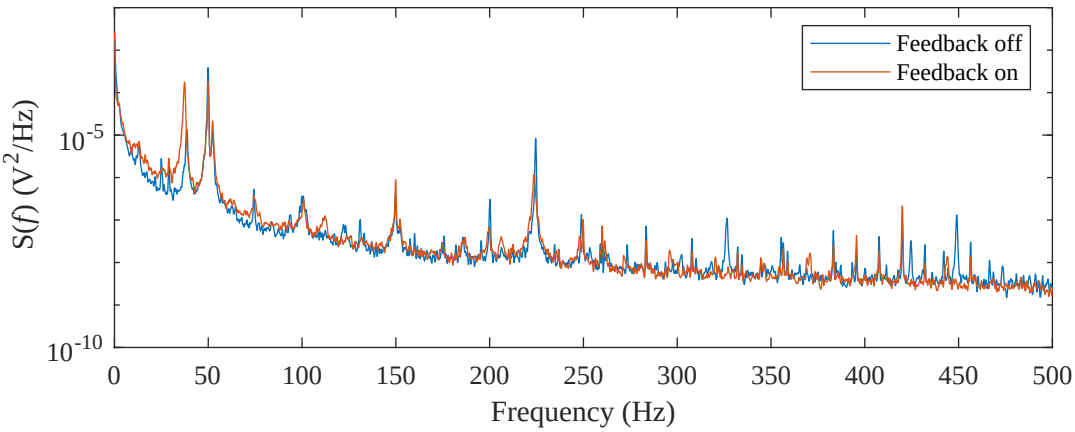

Fig. 4.16 The PSDs of the summation of the two particle positions along axial axis with feedback on and off. More than six motion peaks can be observed and some of the peak values dropped after feedback signal is switched on. No filtering is applied to the feedback signal.

oscillation mode. We can further quantify the cooling and heating after the calibration of the two particle motion is finished.

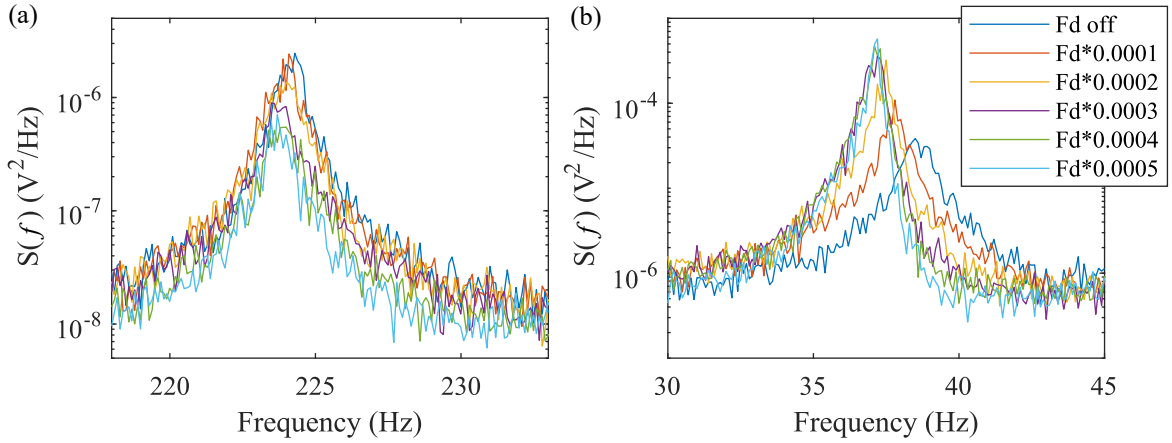

Fig. 4.17 Feedback cooling of two particles based on EBC detection. The spectrum with distinct motion peaks exhibiting varied cooling or heating outcomes. (a) Cooling with 224 Hz mode. The oscillating frequency around 224 Hz has cooling effect. (b) Heating with 37 Hz mode. The mode with about 37 Hz has heating effect. Cooling or heating should be determined from the phase difference between the detected position signal and the feedback velocity signal.

In conclusion, we have demonstrated linear feedback cooling of an array of levitated microparticles based on EBI technique. The real-time output of detected events from

the event-based camera is achieved via employing a FPGA system. The efficiency of the feedback cooling scheme is explored through a QPD for detection, and an eight-fold reduction in the CoM temperature at 2×10^{-2} mbar is achieved. Switching to an EBI, we further conducted the feedback cooling of one particle at the same pressure to get a four-fold temperature reduction, which might be originated from EBC receiving more $1/f$ noise at low frequencies. The cooling temperature is limited by the back-action of motion measurement and background-gas collisions. The cooling effect with different feedback phase is also investigated at 4×10^{-2} mbar. For the feedback cooling of multi-particles, certain modes that undergo cooling effect are observed via changing feedback gains, which verifies the feasibility of cooling an array of particles simultaneously.

Chapter 5

Electric detection of particle motion

In this chapter, theory of an electric detection and schematic of experimental setup are introduced with the aim to realize the electric detection of a charged microparticle in the Micro-Paul trap.

5.1 Introduction

Levitation of mesoscopic particles in high vacuum provides a promising platform to investigate nanoscale thermodynamics and the boundary between the classical and quantum worlds. By using a microfabricated Paul trap, charged particles with a wide range of sizes and materials can be coupled to the electrodes of the trap, enabling all-electrical levitation and cooling [20]. With this two-way interaction between mesoscopic particles and the trapping electrodes, detection and control of particle motion can be realized.

In this chapter, plans to control the motion of charged microparticles in microfabricated Paul traps by coupling to electronic circuitry will be described. This will create a compact, monolithic platform for the manipulation of charged microparticles, for applications in force sensing, studies in nanothermodynamics, and exploration of macroscopic quantum physics.

5.2 Theory of electric detection

Unlike the optical detection of particle motion in optical traps, an electric method is shown in Figure 5.1, which has not previously been used for mesoscopic particles. In this picture, d is the distance between the two plates of a capacitor formed by the endcap electrodes, C_0 is the capacitance and U_C is the voltage across the endcaps. An inductance L is also added to form an LC circuit with the circuit damping rate $\Gamma_{\mathrm{cir}} = \frac{R}{L}$. If we consider the velocity of

the charged particle along the z axis, the current I flowing in the circuit can be depicted as

$$I = -\frac{Q}{d}\dot{z} + C_0\dot{U}_C. \tag{5.1}$$

where Q is the charge of the particle. When the circuit damping rate Γ_{cir} is much larger than the motion frequency of the particle ω_z, namely $\Gamma_{\text{cir}} \gg \omega_z$, Equation 5.1 is written as

$$I = -\frac{Q\eta}{d}\dot{z}. \tag{5.2}$$

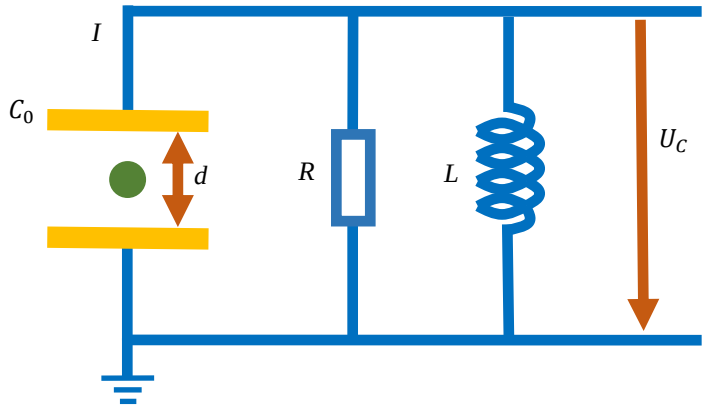

Fig. 5.1 Circuit diagram for motion detection of a charged particle in the Micro-Paul trap. The motion of the charged particle leads to the variation of the induced current.

Compared with Equation 5.1, Equation 5.2 loses the second term and introduces a geometry factor η which is a single endcap geometry factor in an idealised Paul trap. Therefore, according to the variation of the current we can detect the motion of the trapped mesoscopic particle. This electric detection has been proved in electrons, ions and protons [151, 152, 70] which makes it feasible for nanoparticles and microparticles. From the equipartition theorem, the maximum value of the velocity is

$$\dot{z}_{\text{max}} = \sqrt{\frac{k_B T_{\text{CoM}}}{m}}. \tag{5.3}$$

where k_B is the Boltzman constant and T_{CoM} is the temperature of the centre-of-mass motion. Therefore, the peak of the image current I is

$$I_{\text{max}} = \frac{Q\eta}{d}\sqrt{\frac{k_B T_{\text{CoM}}}{m}}. \tag{5.4}$$

We can notice that the maximum of the current scales with the ratio of $\frac{Q}{\sqrt{m}}$. So a comparable current can be produced for highly charged mesoscopic particles compared to

ions. For example, a silica sphere particle with $1\,\mu$m radius has a mass $m = 5.5 \times 10^{12}$ amu and a realistic charge $Q = 10^6$ e [20]. Therefore, the $\frac{Q}{\sqrt{m}}$ of the particle is 1.7×10^{-6} C/kg. A $^{88}Sr^+$ ion has a mass $m = 88$ amu and a charge of $Q = 1$ e. The $\frac{Q}{\sqrt{m}}$ of the $^{88}Sr^+$ ion is 4.2×10^{-7} C/kg.

5.3 Motion detection

Based on the electric detection, exploration of motion detection of levitated microparticles is carried out. In this chapter we focus on the electric detection of particle motion along axial axis, namely z axis. Considering the weak signal of induced current, we firstly design a schematic of this electric detection.

5.3.1 Schematic of experimental setup

Figure 5.2 gives a schematic of our experimental setup for particle motion extraction via electric detection. Two resistors with large resistance are introduced between the two endcaps and their two DC voltage supplies to block the caused current from flowing into the circuit branch of the two DC voltage supplies. In consideration of gain bandwidth product (GWB) of amplifiers and the motion frequency ω_z in our experiments is about 100 Hz, a two-level amplification system is adopted instead of only one-level amplification. Picked-up current between two endcaps is firstly amplified via a current amplifier and then secondly magnified by a voltage amplifier. In order to extract the valid motion signal which is buried in noises, a lock-in amplifier (LIA) is used to output a detection result.

5.3.2 Electric detection

In our experiments, we choose a current amplifier (Stanford Research System; model: SR750) for its low-noise properties. From the manual of the current amplifier, it labelled $5\text{fA}/\sqrt{\text{Hz}}$ input noise, $1\text{pA}/V$ maximum gain, adjustable bias voltage, two configurable signal filters and variable input offset current. This device also supports battery operation up to 15 hours which means it will minimize the noises added by power supply. As for the voltage amplifier, we use a JFET voltage amplifier (Stanford Research System; model: SIM910) for low-noise consideration as well. From the manual of the voltage amplifier, it labelled $4\text{nV}/\sqrt{\text{Hz}}$ input noise, AC or DC coupled and selectable gain from 1 to 100. When it comes to LIA, we finally choose a LIA (Stanford Research System; model: SR860) with a mentioned reference frequency range of 1 mHz to 500 kHz.

The performance of LIA to detect small signals buried in noises is firstly tested. Setting the voltages of trap electrodes as follows: AC voltages of 400 V amplitude with a frequency

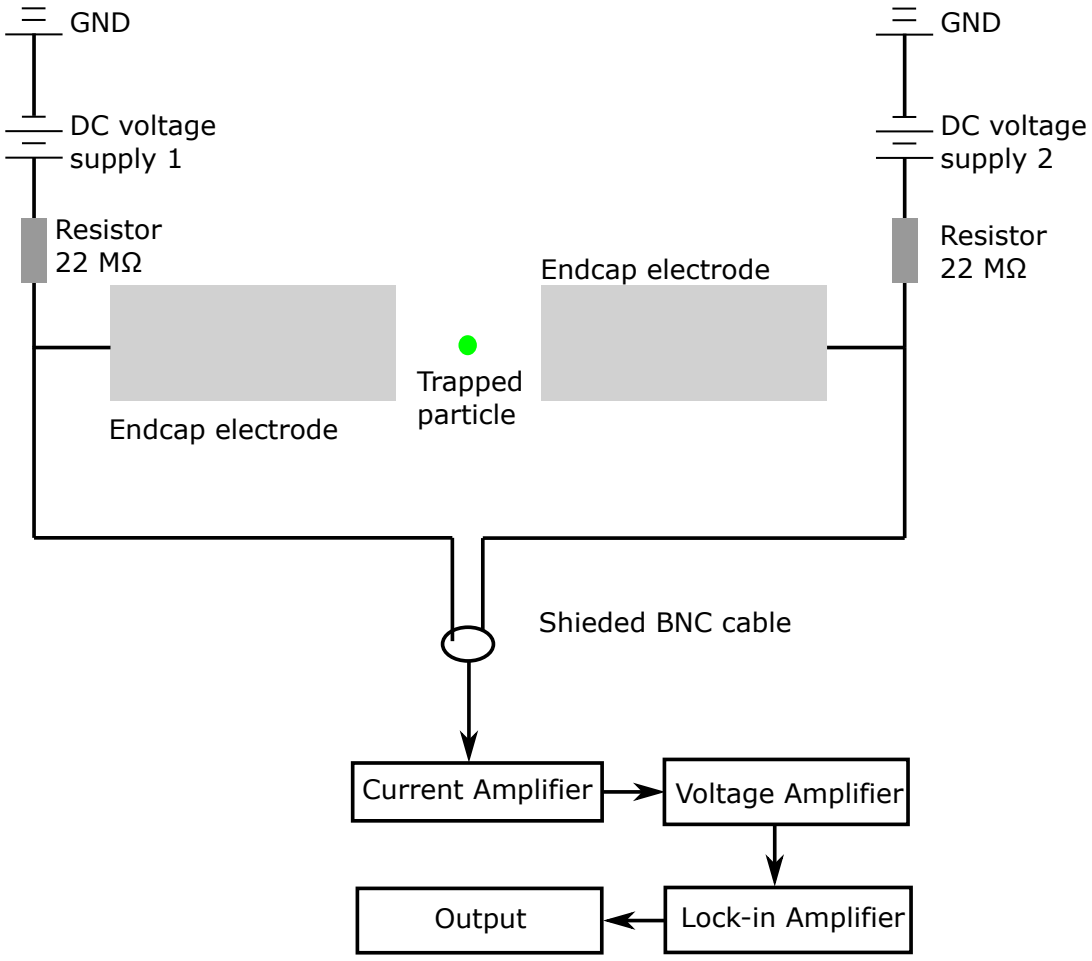

Fig. 5.2 The schematic of experimental setup for electric detection. Two resistors with large resistance are introduced between the two endcap electrodes and related two DC voltage supplies. Picked-up current caused by particle motion between two endcaps is firstly amplified via a current amplifier and then secondly magnified by a voltage amplifier. A LIA is next utilized to detect the current signal buried in noises and output the final detection result.

of 810 Hz. The two endcap electrodes are held at a potential of 1.0 V. Two diagonal DC electrodes are independently set to 0 V and -2.0 V, respectively. The measurements are performed at a pressure of 5×10^{-2} mbar. Using a QPD for detection, we can get the PSDs of particle motion along the z axis shown in Figure 5.3(a) and get the oscillation frequency of the trapped particle, which is $\omega_z = 82 \times 2\pi$ Hz. Adding an absorptive neutral density filter in front of our illumination laser, and setting the QPD amplification/gain from 10 to 3, we then decrease the obtained motion signal and Figure 5.3(b) illustrates the PSD of the decreased motion signal. No motion peaks can be observed but only a 50 Hz frequency originating from the power supply.

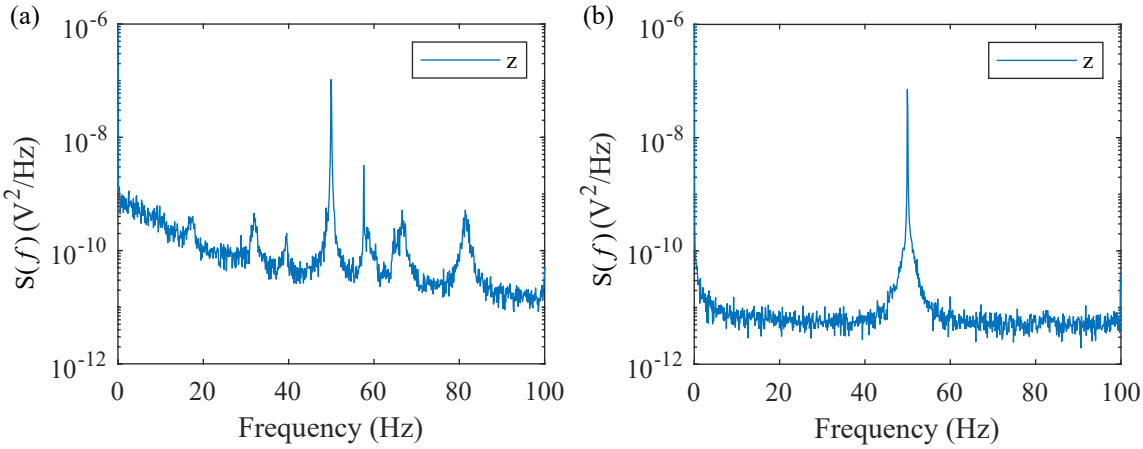

Fig. 5.3 The PSDs of particle motion along the z axis (a) before and (b) after attenuation of laser and QPD magnification. Data is taken at 5×10^{-2} mbar. (a) The PSD of particle motion. A $82 \times 2\pi$ rad/s oscillation frequency can be observed. (b) The PSD of particle motion after we decrease the power of the illumination laser and the QPD magnification. No motion peaks can be witnessed but only a 50 Hz frequency originating from the power supply.

Connecting the decreased particle motion signal in Figure 5.3(b) to the LIA input and setting the inter sweeping frequency of the LIA changing from 60 to 90 Hz, we then get an average output of five times frequency sweeping shown in Figure 5.4. The inter frequency of LIA is doing cyclic sweeping and a dominant peak can be noticed when the sweeping frequency approaches the particle motion frequency ω_z. By extracting the frequency information of these peaks, we obtain $\omega_z = (83 \pm 2) \times 2\pi$ rad/s, which matches the frequency detection from Figure 5.3(a).

To test a minimum detection based on the LIA, a $103 \times 2\pi$ rad/s sine signal is then added to one of the trap DC electrodes shown in Figure 4.1. By tuning the peak-to-peak voltage (VPP) of the sine wave, the amplitude of the LIA input signal can be controlled. Via setting the VPP of the sine signal to be 0.05 V and the inter frequency of the LIA sweeping from 101 Hz to 104 Hz, we can get an average amplitude detection result shown

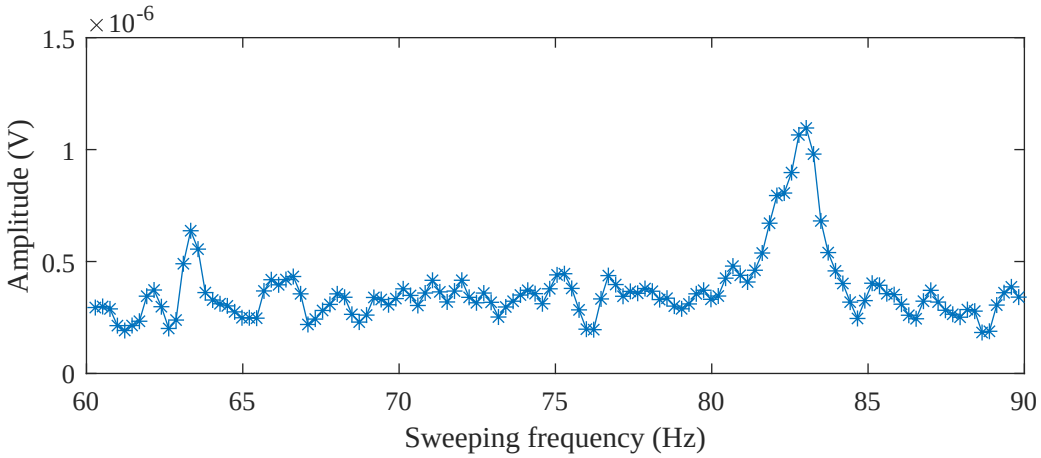

Fig. 5.4 Detection test of the LIA. The setting of inter frequency of the LIA sweeps from 60 to 90 Hz and the average amplitude outputs from LIA. The peak can be clearly observed when the inter sweeping frequency is approaching to particle motion frequency.

in Figure 5.5. The peak can be clearly observed when the inter sweeping frequency approaches the particle motion frequency. By extracting the frequency information of these peaks, we obtain $\omega_z = (103.35 \pm 0.04) \times 2\pi$ rad/s, which is close to the set sine frequency $103 \times 2\pi$ rad/s. The frequency difference of 0.3 Hz between the extracted frequency and the setting sine wave frequency might be caused by the noises of the input signal to the LIA. The extracted peak amplitude is $(6 \pm 1.0) \times 10^{-4}$ V. In this experiment, the current amplifier is with 200 nA/V sensitivity, the voltage amplifier is with 100 gain and the LIA works with 500 uV sensitivity. Therefore, we detect a current signal at $(\omega_z = 103.35 \pm 0.04) \times 2\pi$ rad/s with $(1.1 \pm 0.2) \times 10^{-12}$ A. Further reduction of the added sine wave amplitude cannot make the induced current between the two endcaps detected by our system, which means that the detected signal is below the minimum detection level of our system.

Although the fundamental limit to the noise floor is Johnson-Nyquist noise, to push down the minimum detection level of our system, the magnification of detection should be increased. Now the magnification is limited by a dominated AC current which is induced from the provided AC voltage of the trap. In order to have a clear understanding of the current induced by the AC voltage, we compare two situations of detected current signals with provided AC voltages switched off and on. Figure 5.6(a) gives the detected current signal with the AC voltage switched off and Figure 5.6(b) gives the current signal with the AC voltage switched on. We can witness that the peak-to-peak voltages of the detected currents increase from 70 mV to 4 V after the AC voltage is added to the trap. The spectrum in Figure 5.6(b) also illustrates that the detected current has the same frequency with the setting AC voltage frequency to be 980 Hz .

According to Equation 5.4, we can estimate a maximum scale of induced current from the particle motion in our experiments. Take the data in Figure 2.24 as an example,

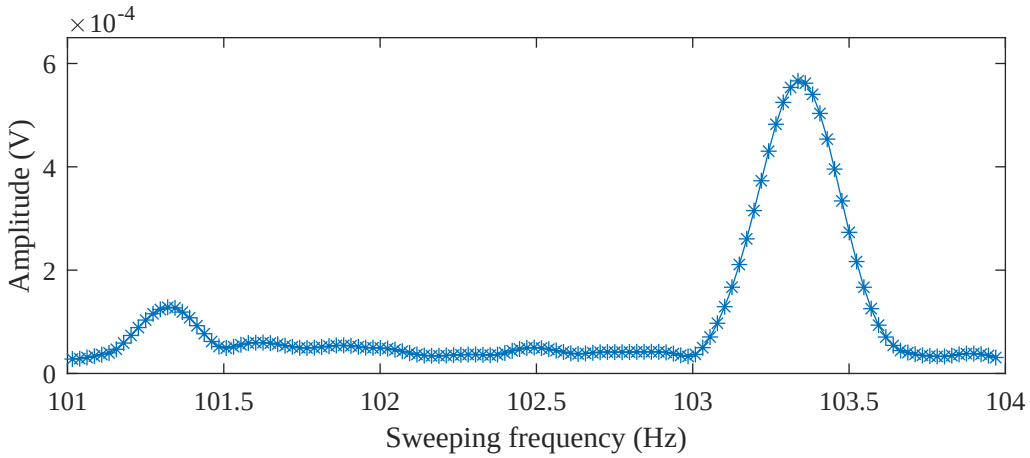

Fig. 5.5 Minimum detection of the LIA. The setting of inter frequency of the LIA sweeps from 101 to 104 Hz and the y axis shows the average amplitude outputs from LIA. The peak can be clearly observed when the inter sweeping frequency approaches the particle motion frequency.

the charge of the particle is $Q = 2900\,\mathrm{e}$ and the centre-of-mass temperature is $T_{\mathrm{CoM}} = 1300 \pm 90\,\mathrm{K}$. Assume the geometry factor $\eta = 1$, we can get $I_{\mathrm{max}} = (2.2 \pm 0.2) \times 10^{-16}\,\mathrm{A}$. Thus the minimum detection level of our system should be pushed down by four orders.

5.3.3 Improvement of electric detection

To achieve the electric detection of particle motion, we can conduct the improvements illustrated in Figure 5.7 which mainly include two aspects. One is to increase detection magnification and the other is to induce large image current from particle motion. In consideration of detection magnification, lowering the induced current caused by AC voltages and using multi-level amplification are available. Decreasing the induced current caused by the AC voltages incorporates utilizing an LC circuit as a filter and shielding the two endcaps. To increase the image current caused by particle motion, we can focus on heating the particle to get high T_{CoM} and lessening the separation between the two endcap electrodes. We discuss these methods below. Of course increasing the charges of levitated particles is also an available scheme, but it is not that easy to realize and is therefore out of our near future plan.

LC circuit

Although the LIA has built-in filters to process the magnified input current signal, an LC circuit can work as a a band-pass filter to lower the induced current by AC voltages before the Current amplifier. Thus magnification of the detection system can be increased. To determine the inductor and capacitor values of the LC circuit, a simulation based on NI

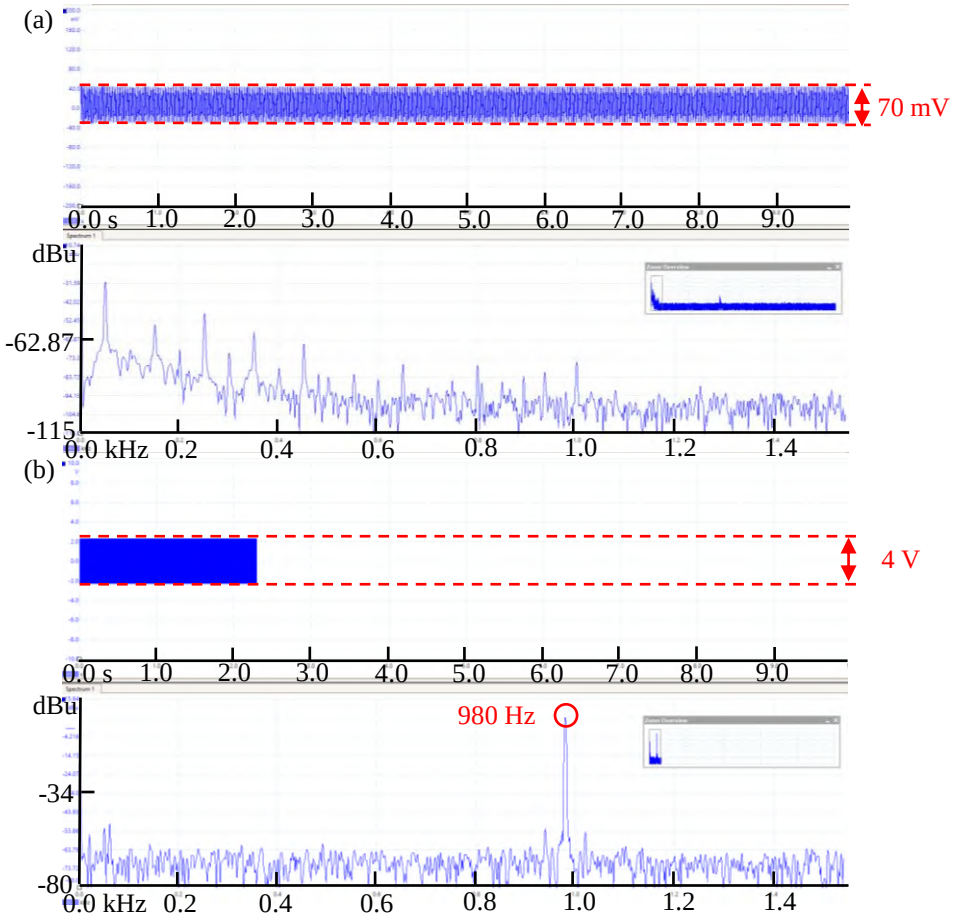

Fig. 5.6 The current induced by AC voltage to the two endcaps. The frequency of the AC voltage is $\Omega_{RF} = 980 \times 2\pi$ rad/s. (a) The signal output of the current amplifier with all voltages switched off. (b) The signal output of the current amplifier with all voltages switched on, in which the component of 980 Hz signal dominates.

Multisim software is carried out at first. Figure 5.8(a) shows the diagram of the designed current band-pass filter consisting of an LC circuit. The values of the inductor and capacitor are respectively $L_1 = 100$ mH and $C_1 = 25\mu$F. The resistor is set to be 100Ω. We set the input AC current to be 1 kHz frequency and 1 A amplitude. Figure 5.8(b) depicts the frequency response of the current amplitude flowing through a capacitor C_1. Therefore, we can get the resonance frequency of the LC circuit $\omega_{LC}/2\pi$ about 100 Hz with 50 Hz lower cut-off frequency and 200 Hz upper cut-off frequency.

Particle heating

According to Equation 4.2, if we feedback noises to levitated particles, the particle will get heated and the related T_{CoM} will get increased. Therefore, we test the heating of the

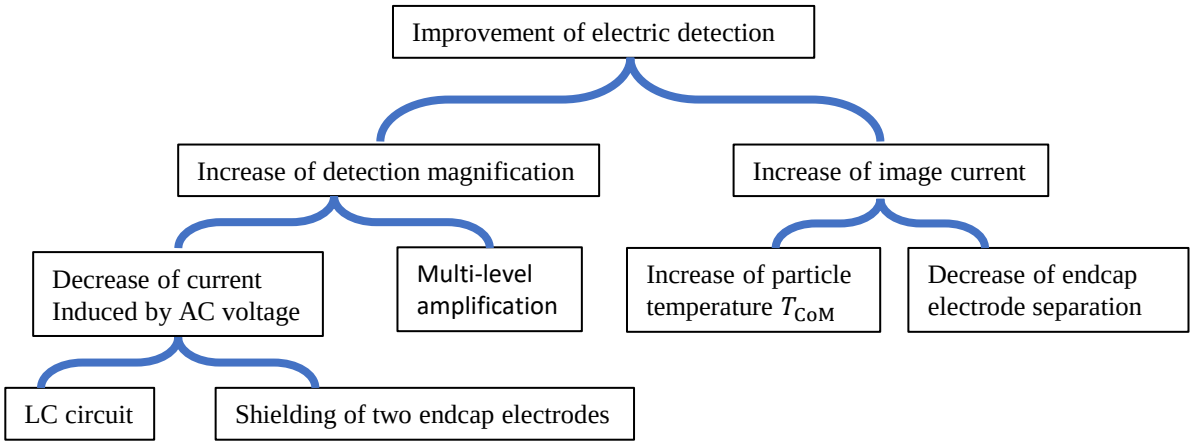

Fig. 5.7 Procedures of electric detection improvement. Increase of detection and image current are two mainly focused aspects. To realize high detection magnification, we can lower the induced current caused by AC voltages and adopt multi-level amplification. To deduct the induced current by AC voltages, An LC circuit working as a band-pass filter and add shielding to the two endcaps can be added. In order to enlarge the image current, heating the trapped particle and lessening the distance between the two endcap electrodes are both available.

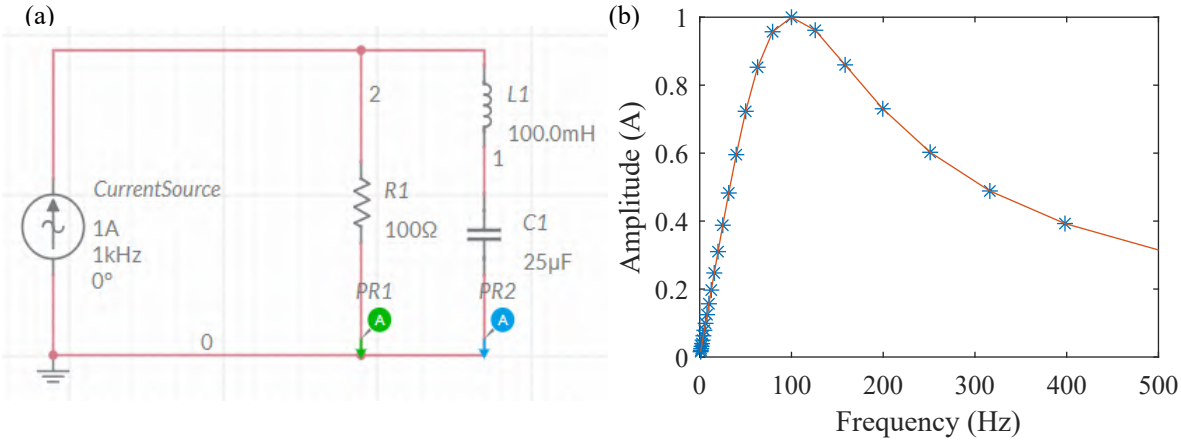

Fig. 5.8 Simulation of the LC circuit. (a) The diagram of the LC circuit. (b) The frequency response of the current amplitude flowing through a capacitor. The designed resonance frequency of the LC circuit $\omega_{LC}/2\pi$ about 100 Hz with 50 Hz lower cut-off frequency and 200 Hz upper cut-off frequency.

levitated particle with white noise for a proof of principle. White noise as a specific type of broadband signal is suitable to heat trapped particles without adding any specific obvious frequency. Therefore, we can choose white noise to heat particles to enlarge the induced image current. In experiments, a white noise is generated and then connected to one summing amplifier (Stanford Research System; model: SIM980). The amplitude of the white noise is 10V amplitude due to the maximum input limit of the summing

amplifier. The summing amplifier adds the white noise and setting DC voltage together to supply potential to one DC electrode of the Paul trap system. Figure 5.9 displays two PSDs of a levitated particle along the z axis without and with white noise heating based on CMOS camera detection. The particle motion frequency is $\omega_z = 104 \times 2\pi$ rad/s. Because the detection based on CMOS camera receives more $1/f$ noise compared to QPD, the noise level of the heated PSD curve is increased at low frequencies compared with the unheated curve, but the peak value for ω_z does not show obvious variance. Therefore larger amplitude of white noise should be added to a levitated particle. We could combine the white noise and an AC signal (instead of the DC voltage) via the summing amplifier firstly and then amplify the summing amplifier output for our next steps.

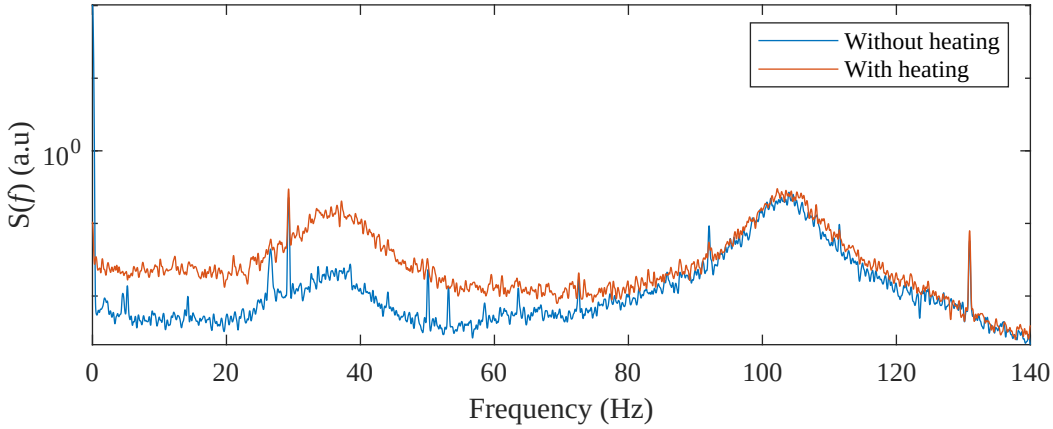

Fig. 5.9 Particle heating due to extra white noise. The blue and red lines represent the PSDs of a levitated particle motion along z axis with motion frequency $\omega_z = 104 \times 2\pi$ rad/s. The blue curve is without heating while the red corresponds to heating situation.

Shielding of endcap electrodes

Providing shielding to the two endcap electrodes is also a valid way to decrease the current induced in the endcaps due to the AC voltage. Figure 5.10 is a new fabricated Micro-Paul trap. The diameter of the two endcaps is 0.3 mm diameter and the other four electrodes are with 1 mm diameter. The two endcaps are shielded via two tubes with 0.6 mm inner diameter and 1mm outer diameter. The distance between the endcap electrodes is 750 μm.

It is also useful to explore more highly charged spheres, so the ratio of $\frac{Q}{\sqrt{m}}$ can be increased to produce large image current caused by particle movement.

In conclusion, we introduced a novel electric detection to recover the motion information of levitated charged particles. The experimental setup for the electric detection is designed and carried out. Based on this setup, the detection of current signal can reach

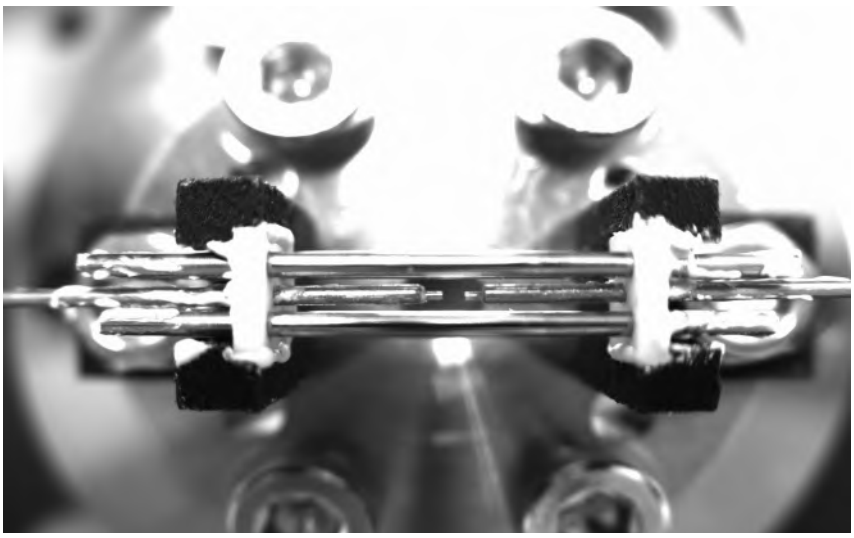

Fig. 5.10 A new Micro-Paul trap with two endcaps shielded via two 0.6 mm inner diameter tubes. The distance between the endcap electrodes is 750 μm.

$(1.1 \pm 0.2) \times 10^{-12}$ A. According to a theoretical estimation, the image current induced by the particle CoM motion is about 2×10^{-16} A. The current between two endcaps from provided AC voltages is verified to limit the magnification of the detection system. Further improvement of the electric detection can be centred on utilizing an LC circuit, shielding the endcap electrodes, adopting multi-level amplification instead of two-level amplification, heating the CoM motion of levitated particles and shortening the endcap distance.

Chapter 6

Conclusion and outlook

To make a summary of the introduced work throughout the thesis, the construction and characterization of the Micro-Paul trap of 300 μm diameter endcaps with 800 μm separation is explained. The detection of the motion of single and multiple particles is utilized and characterized. The EBI technique is adopted for feedback cooling to get a four-fold reduction of the centre-of-mass temperature T_{CoM} and multi-particle cooling. An electric detection is introduced to recover the motion of the trapped particle and the detection of current signal is now pushed to $(1.1 \pm 0.2) \times 10^{-12}$ A.

Next steps will be focused on multi-particle cooling, improving electric detection and testing a chip-based Micro-Paul trap. Therefore, I will explain the future work from the three aspects.

6.1 Feedback cooling of multi-particles with a new Micro-Paul trap with large endcap separation

In order to further analyze the cooling of multi-particles, simplification of the particles' interaction is required. As we observed from Figure 4.17(a) in Section 4.3.3 , there are more than six peaks for the added two-particle motion spectrum along axial axis, which indicates that the interaction of the two particles on the radial plane is also strong. This is also clear visually, the two particles are not aligned along the axial axis. However, limited by the short distance between two endcap electrodes ($2z_0 = 800\mu$m), the trapping region along the axial axis is very narrow. Therefore, we couldn't control two particles to locate in a line parallel the trap axis (or z axis). To solve this problem, we designed a new Paul trap which has large separation ($2z_0 = 1500\mu$m) between the two endcap electrodes. It has four 1 mm diameter rods at the outer circle and has two 0.3 mm diameter rods in the middle region to work as endcap electrodes. The base of the trap is constituted of several same blocks with two M3 holes to make the trap assembly flexible. Then we send the

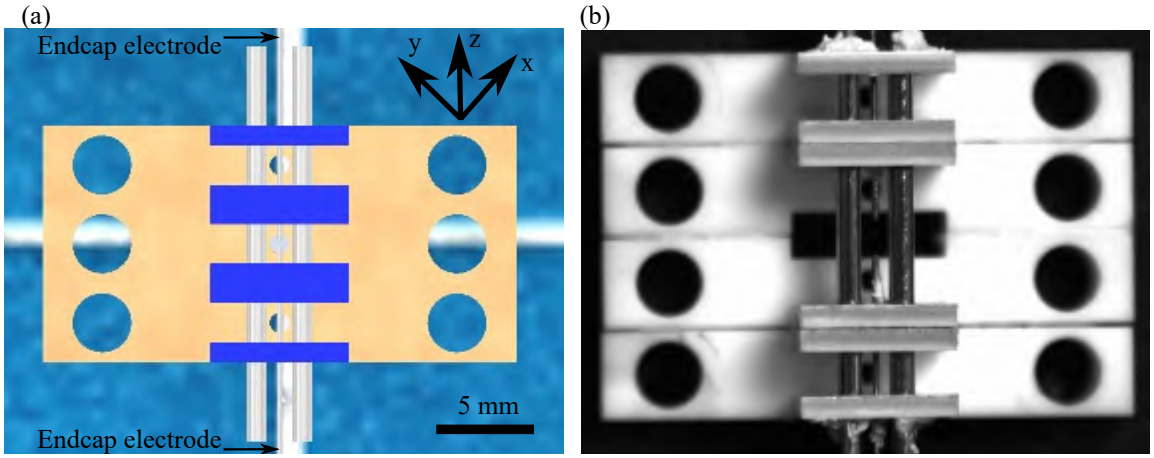

Fig. 6.1 The image of new micro-Paul trap with large separation between two endcap electrodes. In comparison to the preceding Paul trap configuration, the recently implemented Paul trap setup remain the same geometric characteristics, except for the increase in the endcap separation to control two particles in a line parallel to trap axis. In the context, trap axis is z axis. (a) The system design. (b) The real image of the new fabricated Paul trap system which is made of ceramics material.

drawing to factory to manufacture ceramics pieces and then the fabricated trap is shown in Figure 6.1 ((More information please see Appendix C)). In contrast to the preceding linear Paul trap configuration, the geometric characteristics of the recently implemented Paul trap setup remain unchanged, except for the alteration in the separation distance between the two endcap rods.

6.2 Electric detection with a shielded Micro-Paul trap

When the two endcap electrodes are shielded, the current induced by the provided AC voltages can be decreased. With the new fabricated Micro-Paul trap shown in Figure 5.10, we can levitate a microparticle and further increase the amplification of image current detection hopefully by 2×10^2 times. The current amplifier is now with 200 nA/V sensitivity and its minimum sensitivity is 1 nA/V in consideration to the GWB of the amplifier. Besides, employing a multi-level amplification instead of two-level amplification can also help to increase detection amplification.

At the same time, we can heat the CoM motion of a levitated particle and decrease the distance between two endcaps to increase the induced image current from the particle motion. The designed LC circuit shown in Figure 5.8 working as a band-pass filter can also be tested to decrease current induced by provided AC voltages.

6.3 Chip-based Micro-Paul trap

Except the micro-fabricated linear Paul trap in Section 2.4.1, We also consider a chip-based Micro-Paul trap for charged particle levitation and control which is manufactured by A. G. Sinclair's group at National Physical Laboratory [153–155]. Figure 6.2(a) shows a photograph of a monolithic three-dimensional ion trap mounted to a ceramic chip carrier. In the picture, there are 21 connection ports to voltages on each side of the chip.

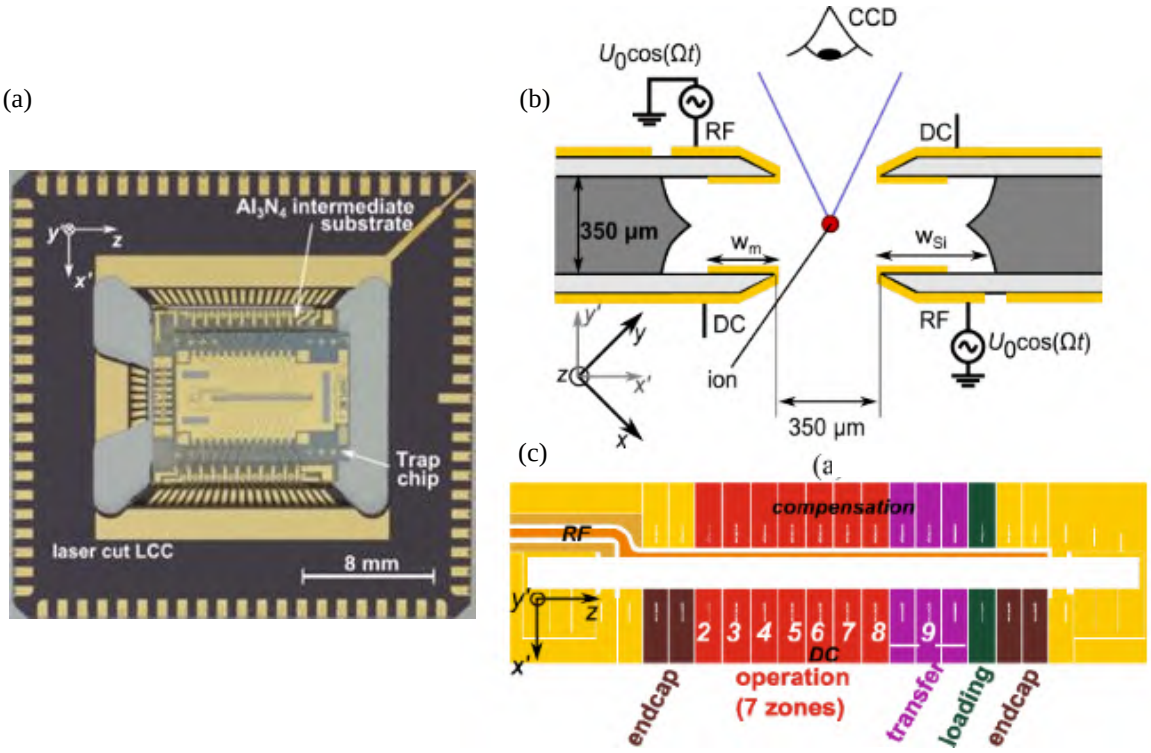

Fig. 6.2 The physical map and structure of the chip-based Micro-Paul trap. Reproduced from [155]. (a) The physical map of the chip-based Micro-Paul trap. In the map, there are 21 ports on each side of the chip. (b) The cross section of the micro-fabricated trap. There are two layers of oxidised Si and a highly doped Si bulk between them. Si bulk works as a conducting spacer and the oxidised Si layer provides low-loss dielectric isolation. Gold electrodes are patterned on top of the oxidised Si. The thickness of the gold electrodes is about 5 μm. The thickness of Si bulk is 350 μm and the oxidised Si layer is 15 μm-thick. (c) The top view of the micro-fabricated chip structure. Five distinct regions can be observed which include the endcap region, operation region, compensation region, transfer region and loading region.

Figure 6.2(b) and (c) reveal the trap geometry of the microfabricated chip structure. A 3D electrode structure replaces the four rods in a linear Paul trap and the chip trap has unit aspect-ratio geometry shown in Figure 6.2(b). The chip provides seven operation segments and makes it possible to control several particles at the same time. In Figure 6.2(c), the top-plate of the trap is shown, with five distinct regions: the endcap region, operation region,

compensation region, transfer region and loading region. This geometry is reproduced in reflection on the bottom layer. These chips are designed for use in atomic-ion quantum computing experiments, and hence have such a complex structure. In those experiments, charged particles are firstly captured in the loading region and then are transferred to the transfer region to avoid electrode pollution caused by particle launching. Finally, they are controlled in the operation region. This scheme will not necessarily be used in our experiment, but may be necessary if our silica particles contaminate the chip. The endcap region is connected to DC voltages to control the particle motion along the z axis, and the compensation region is designed to compensate for stray electric fields. Segments from 2 to 8 span a length of 2.01 mm.

Based on the chip geometry, we simplified the structure to that shown in Figure 6.3 to carry out a simulation. In Figure 6.3(a), each electrode has a dimension of $1000\,\mu$m $\times$ $280\,\mu$m $\times$ $20\,\mu$m (Length $\times$ Width $\times$ Thickness). Si bulk is $350\,\mu$m-thick and the distance between two electrode tips is $350\,\mu$m. Figure 6.3(b) is the top view of the whole structure.

Four electrodes on each layer of the chip, which are $880\,\mu$m away from the middle plates, are used for endcap electrodes and the middle ones are utilized for AC electrodes. The length from the trap centreline to the endcap electrode surface is $z_0 = 1.02$ mm. The width of the electrodes on the left side is 570 μm and the width is 860 μm for the right side electrodes. So the distance from the centre of the trap to the surface of the electrodes is $0.175\sqrt{2}$ mm and the distance from the trap centre to the endcap should be about $\sqrt{\left(0.175\sqrt{2}\right)^2 + 1.02^2} \approx 1.05$ mm.

Then, we can establish this chip trap model in the SIMION environment depicted in Figure 6.3(c)-(e). Figure 6.3(c) is the whole structure and the angle between the plate and x axis is 45° , to match the standard linear Paul trap geometry (see Figure 2.5). Figure 6.3(d) and Figure 6.3(e) are the side view and top view of the chip trap. In order to make the charged particles stably captured, we pick up values for AC voltage and DC voltage so that the related values of a_i and q_i are in the stability region of the Paul trap. If we connect the AC voltage with $V_{RF} = 150$ V and $\Omega_{RF} = 2000 \times 2\pi$ rad/s and the endcap electrodes with $U_{DC} = 1$ V, the potential distributions of the trap and motion frequencies of trapped particles can be analysed.

Because the motion region of the trapped particle is a small part around the trap centre, we test the harmonicity of the electric potential in a central $100\,\mu$m cube distributions along three axes. In this simulation, each grid size of the electric field is 0.02 mm so the minimum spatial resolution is 0.02 mm. The quadratic equation $V = \kappa_{1i}{u_i}^2 + \kappa_{2i}u_i + \kappa_{3i}$ is used to fit the potential distribution, where V is the potential and i can be x, y and z with all lengths in mm. Table 6.1 lists the fitting results.

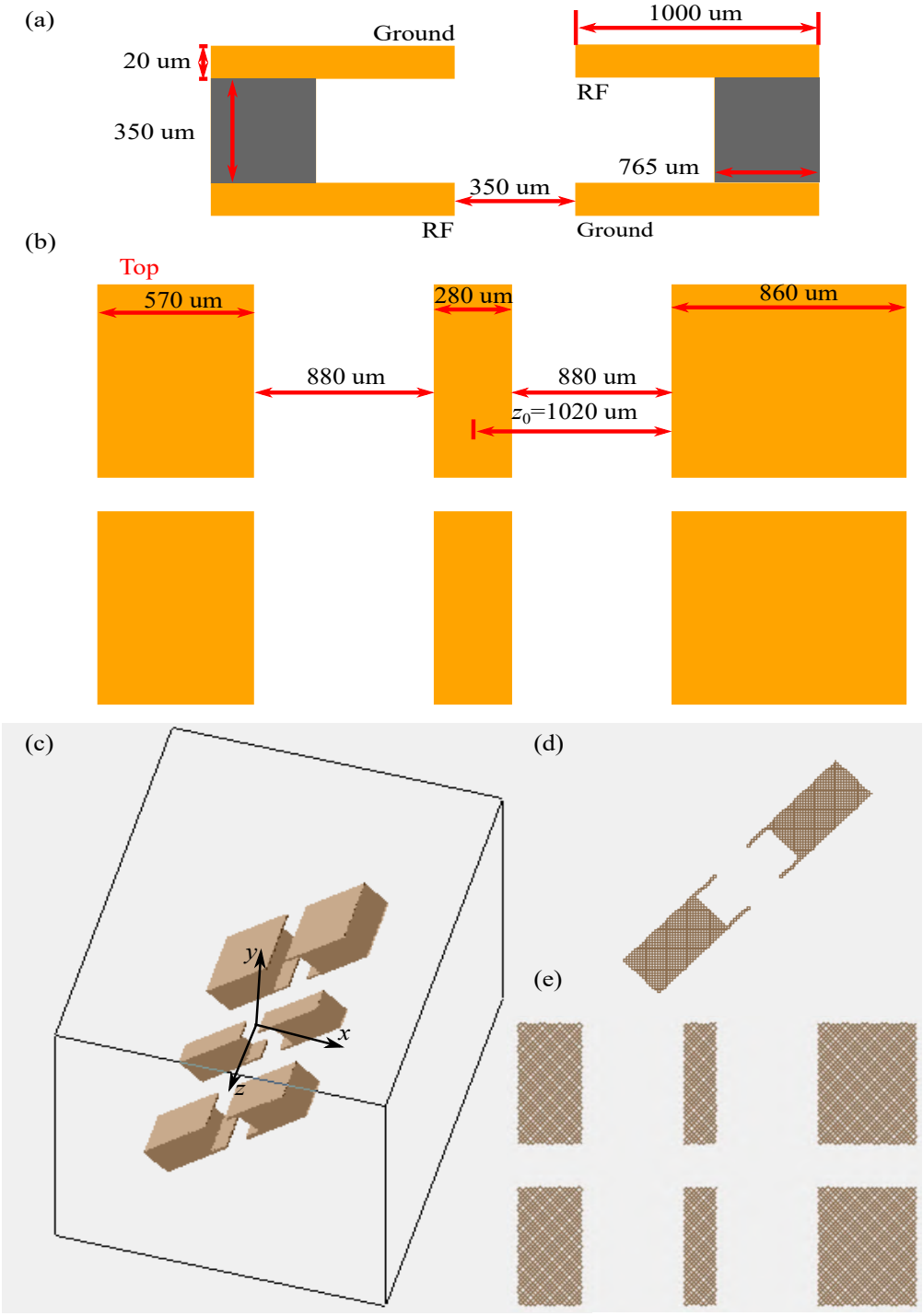

Fig. 6.3 The simplified structure of the chip trap. (a) The simplified cross section of the structure. (b) The top view of the whole structure. (c)-(e) The chip trap in SIMION environment. There are two layers of the trap with endcap electrodes are on the two sides. Charged particles are trapped in the region constructed by the middle four plates.

Table 6.1 The fitting results of potential distributions from Micro-trap chip.

κ_{1x}	κ_{2x}	κ_{3x}	κ_{1y}	κ_{2y}	κ_{3y}	κ_{1z}	κ_{2z}	κ_{3z}
-696.9	-1.3	50.6	961.5	-1.7	50.6	-194.4	0.8×10^{-1}	50.6

Table 6.2 Geometric factors obtained from the Micro-trap chip.

	x	y	z
α	0.79 ± 0.01	-0.57 ± 0.01	$(-1.59\pm0.01)\times10^{-1}$
β	-0.46 ± 0.02	-0.43 ± 0.02	$(7.47\pm0.03)\times10^{-1}$

Compared with κ_{1i}, κ_{2i} $(i=x,y,z)$ can be negligible. With the same method mentioned above in Section 2.2.2, we can get the values of six geometric factors α_i and β_i $(i=\{x,y,z\})$. All the weighting constants are dimensionless and are listed in Table 6.2.

When the DC voltage is $U_{DC}=1\,\mathrm{V}$ and the AC voltage is with $V_{RF}=150\,\mathrm{V}$ and $\Omega_{RF}=2000\times2\pi\,\mathrm{rad/s}$, as for a charged particle with mass $m=8.02\times10^{13}$ amu and the charge $Q=-20000\,\mathrm{e}$, the oscillation frequencies with unit rad/s are calculated via Equation 2.11, Equation 2.12 and Equation 2.13. Divided by 2π, the frequencies with unit Hz are obtained,

$$f_x=415.3\ \mathrm{Hz}, \tag{6.1}$$

$$f_y=301.0\ \mathrm{Hz}, \tag{6.2}$$

$$f_z=78.5\ \mathrm{Hz}. \tag{6.3}$$

With the trajectory data exported from SIMION, the mechanical frequencies in three axes are obtained. The PSD of x position from which we can see the mechanical frequency in the x axis is $f_x'=418.6\,\mathrm{Hz}$. Similarly, the other two frequencies $f_y'=310.9\,\mathrm{Hz}$ and $f_z'=69.8\,\mathrm{Hz}$ in y and z axis can be calculated.

If we compare the two calculation results from Equation 2.11, Equation 2.12, Equation 2.13 and SIMION, we can calculate the relative errors as following

$$\left|\frac{f_x'-f_x}{f_x}\right|=\left|\frac{418.6-415.3}{7.9}\right|=13.9\%, \tag{6.4}$$

$$\left|\frac{f_y'-f_y}{f_y}\right|=\left|\frac{61.0-57.3}{57.3}\right|=6.5\%, \tag{6.5}$$

$$\left|\frac{f_z'-f_z}{f_z}\right|=\left|\frac{75.4-86.7}{86.7}\right|=13.0\%. \tag{6.6}$$

All relative errors are below 15%, therefore we can use the SIMION simulation, the Equation 2.11, Equation 2.12 and Equation 2.13 to predict particle motion in the chip trap.

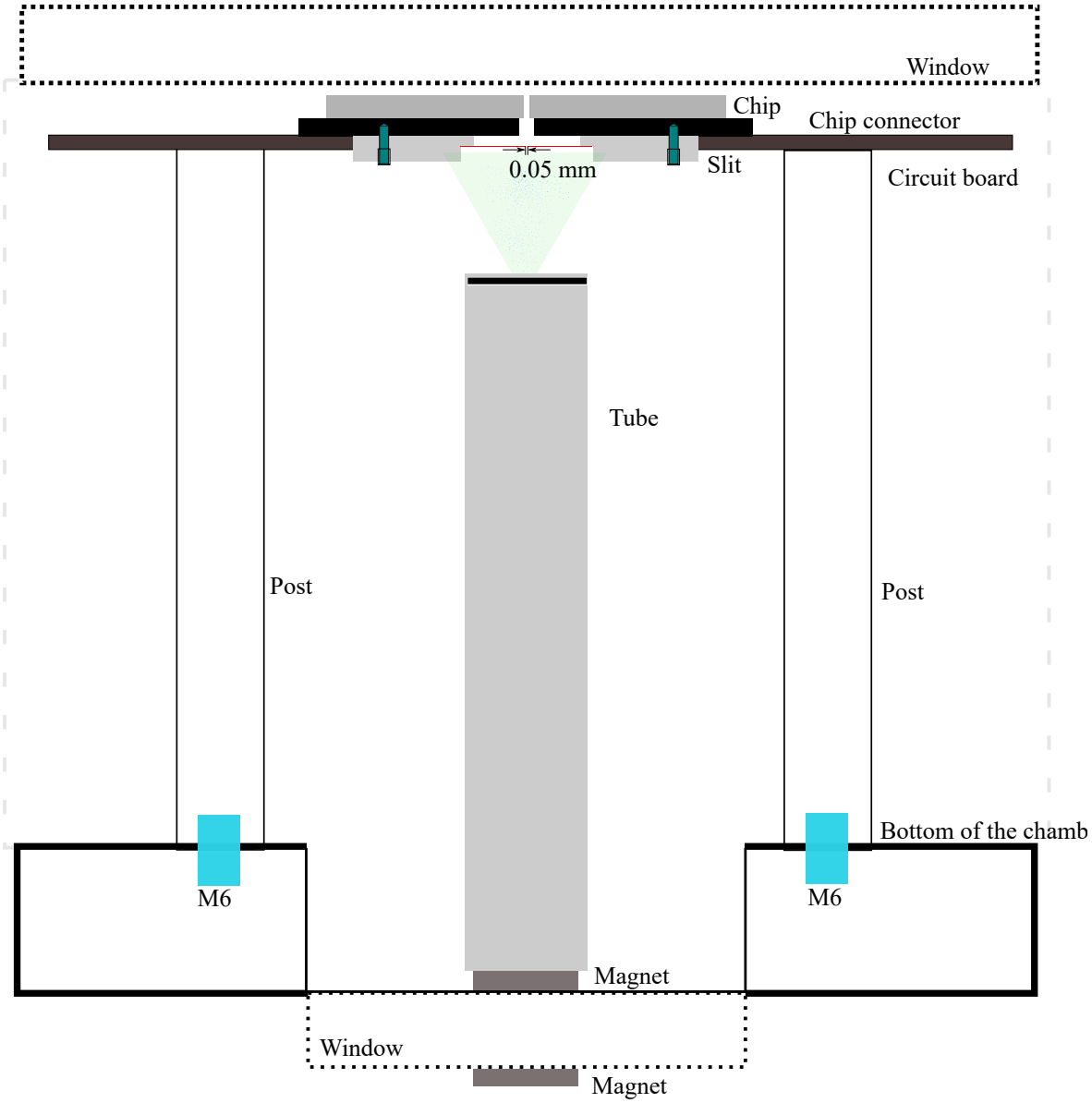

Fig. 6.4 The mechanical structure of the chip trap chip inside chamber. The chip is connected to a circuit board which is put onto four posts. A slit beneath the circuit board is adopted to limit the flying direction of launched particles.

In experiment, we design the mechanical structure of the Paul-trap system shown in Figure 6.4. At the bottom of the chamber we can use a magnet to move a tube which is utilized to launch charged particles. Because the aperture of the Chip trap is very narrow, there is a slit with 50 μm width mounted on the circuit board to prevent charged particles

from getting stuck to the trap electrodes. The chip is placed on a chip connector, which is soldered onto the circuit board.

The wiring of this trap is finished. Figure 6.5(a) is the design diagram and Figure 6.5(b) shows the back of the circuit board. From the pictures, we can see there are mainly four ports connected with voltages, they are DC voltage 1, DC voltage 2, AC voltage and Ground. In Figure 6.5(b), the AC electrodes are connected to three ports of the chip

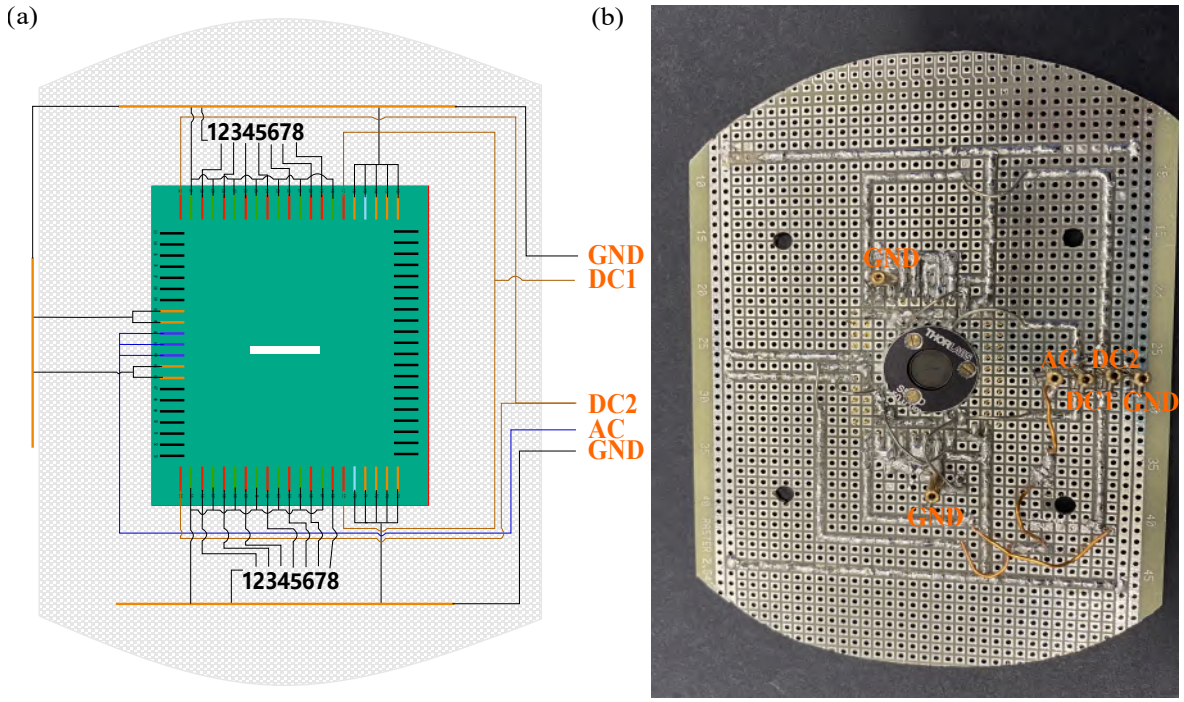

Fig. 6.5 The wiring of the chip trap. (a) The design of the circuit wiring. (b) The image of the wiring on the circuit board.

(labelled with blue color in Figure 6.5(a)). Two electrodes in the transfer region work as endcap electrodes on the right side and are connected to two ports of the chip. Two endcap electrodes on the left side are connected to another chip two ports. So in Figure 6.5(a), we give AC voltages to the three ports, DC voltage 1 signal to the two ports with right endcap electrodes and DC voltage 2 to the two ports with left endcap electrodes. Other electrodes are all grounded. Figure 6.5(b) is the electric connection on the circuit board. The chip ports labelled from 2 to 8 will be the electrodes connected to a circuit for further electric motion detection of a levitated particle.

We then try trapping with this chip trap system, but charged particles will deposit between the gap of chip electrodes which will cause nearby electrodes to be joint. Although we employed a slit with 50 μm width to block particles off the trap centre. But due to the influence of the electric field of trap centre, some particles will oscillate and then deposit on the electrode gap instead of flying away from the chip. The next step is to improve the

electrodes joint caused by charged particles. An available solution might be trap a charged particle with another trap and then transfer it to the chip.

To conclude, work is underway to further minimize our trapping technology and to make it more robust against noise. This will realize the all-electrical levitation, detection, cooling and control of multi-particles in a compact package, ideal for an advanced integrated sensor.

References

[1] S. D. Fuerstenau, W. H. Benner, J. J. Thomas, C. Brugidou, B. Bothner, and G. Siuzdak. Mass spectrometry of an intact virus. *Angewandte Chemie*, 113(3):559–562, 2001.

[2] A. N. Krutchinsky, M. Kalkum, and B. T. Chait. Automatic identification of proteins with a maldi-quadrupole ion trap mass spectrometer. *Analytical Chemistry*, 73(21):5066–5077, 2001.

[3] E. Takács, E. Silver, J. M. Laming, J. D. Gillaspy, H. Schnopper, N. Brickhouse, M. Barbera, M. Mantraga, L. P. Ratliff, H. Tawara, et al. Astrophysics and spectroscopy with microcalorimeters on an electron beam ion trap. *Nuclear Instruments and Methods in Physics Research Section B: Beam Interactions with Materials and Atoms*, 205:144–155, 2003.

[4] T. Li, S. Kheifets, D. Medellin, and M. G. Raizen. Measurement of the instantaneous velocity of a brownian particle. *Science*, 328(5986):1673–1675, 2010.

[5] L. Dania, D. S. Bykov, F. Goschin, M. Teller, and T. E. Northup. Ultra-high quality factor of a levitated nanomechanical oscillator. *arXiv preprint arXiv:2304.02408*, 2023.

[6] J. Gieseler, L. Novotny, and R. Quidant. Thermal nonlinearities in a nanomechanical oscillator. *Nature Physics*, 9(12):806–810, 2013.

[7] A. Vinante, P. Falferi, G. Gasbarri, A. Setter, C. Timberlake, and H. Ulbricht. Ultralow mechanical damping with meissner-levitated ferromagnetic microparticles. *Physical Review Applied*, 13(6):064027, 2020.

[8] Y. Leng, R. Li, X. Kong, H. Xie, D. Zheng, P. Yin, F. Xiong, T. Wu, C. Duan, Y. Du, et al. Mechanical dissipation below 1 μHz with a cryogenic diamagnetic levitated micro-oscillator. *Physical Review Applied*, 15(2):024061, 2021.

[9] D. E. Chang, C. A. Regal, S. B. Papp, D. J. Wilson, J. Ye, O. Painter, H. J. Kimble, and P. Zoller. Cavity opto-mechanics using an optically levitated nanosphere. *Proceedings of the National Academy of Sciences*, 107(3):1005–1010, 2010.

[10] G. P. Conangla, F. Ricci, M. T. Cuairan, A. W. Schell, N. Meyer, and R. Quidant. Optimal feedback cooling of a charged levitated nanoparticle with adaptive control. *Physical Review Letters*, 122(22):223602, 2019.

[11] J. Hofer, G. Higgins, H. Huebl, O. F. Kieler, R. Kleiner, D. Koelle, P. Schmidt, J. A. Slater, M. Trupke, K. Uhl, et al. High-q magnetic levitation and control of superconducting microspheres at millikelvin temperatures. *arXiv preprint arXiv:2211.06289*, 2022.

[12] U. Delić, M. Reisenbauer, K. Dare, D. Grass, V. Vuletić, N. Kiesel, and M. Aspelmeyer. Cooling of a levitated nanoparticle to the motional quantum ground state. *Science*, 367(6480):892–895, 2020.

[13] L. Magrini, P. Rosenzweig, C. Bach, A. Deutschmann-Olek, S. G. Hofer, S. Hong, N. Kiesel, A. Kugi, and M. Aspelmeyer. Real-time optimal quantum control of mechanical motion at room temperature. *Nature*, 595(7867):373–377, Jul 2021.

[14] F. Tebbenjohanns, M. L. Mattana, M. Rossi, M. Frimmer, and L. Novotny. Quantum control of a nanoparticle optically levitated in cryogenic free space. *Nature*, 595(7867):378–382, 2021.

[15] A. Ranfagni, K. Børkje, F. Marino, and F. Marin. Two-dimensional quantum motion of a levitated nanosphere. *Physical Review Research*, 4(3):033051, 2022.

[16] J. Piotrowski, D. Windey, J. Vijayan, C. Gonzalez-Ballestero, A. de los Ríos Sommer, N. Meyer, R. Quidant, O. Romero-Isart, R. Reimann, and L. Novotny. Simultaneous ground-state cooling of two mechanical modes of a levitated nanoparticle. *Nature Physics*, 19:1–5, 2023.

[17] L. Dania, D. S. Bykov, M. Knoll, P. Mestres, and T. E. Northup. Optical and electrical feedback cooling of a silica nanoparticle levitated in a paul trap. *Physical Review Research*, 3(1):013018, 2021.

[18] V. Jain, J. Gieseler, C. Moritz, C. Dellago, R. Quidant, and L. Novotny. Direct measurement of photon recoil from a levitated nanoparticle. *Physical Review Letters*, 116(24):243601, 2016.

[19] D. S. Bykov, P. Mestres, L. Dania, L. Schmöger, and T. E. Northup. Direct loading of nanoparticles under high vacuum into a paul trap for levitodynamical experiments. *Applied Physics Letters*, 115(3):034101, 2019.

[20] D. Goldwater, B. A. Stickler, L. Martinetz, T. E. Northup, K. Hornberger, and J. Millen. Levitated electromechanics: all-electrical cooling of charged nano-and micro-particles. *Quantum Science and Technology*, 4(2):024003, 2019.

[21] D. J. Wineland, J. C. Bergquist, W. M. Itano, J. J. Bollinger, and C. H. Manney. Atomic-ion coulomb clusters in an ion trap. *Physical Review Letters*, 59(26):2935, 1987.

[22] D. Stick, W. K. Hensinger, S. Olmschenk, M. J. Madsen, K. Schwab, and C. Monroe. Ion trap in a semiconductor chip. *Nature Physics*, 2(1):36–39, 2006.

[23] C. Monroe and J. Kim. Scaling the ion trap quantum processor. *Science*, 339(6124):1164–1169, 2013.

[24] S. Arnold and L. M. Folan. Fluorescence spectrometer for a single electrodynamically levitated microparticle. *Review of Scientific Instruments*, 57(9):2250–2253, 1986.

[25] H. Winter and H. W. Ortjohann. Simple demonstration of storing macroscopic particles in a "paul trap". *American Journal of Physics*, 59(9):807–813, 1991.

[26] S. Schlemmer, J. Illemann, S. Wellert, and D. Gerlich. Nondestructive high-resolution and absolute mass determination of single charged particles in a three-dimensional quadrupole trap. *Journal of Applied Physics*, 90(10):5410–5418, 2001.

[27] S. Bose, A. Mazumdar, G. W. Morley, H. Ulbricht, M. Toroš, M. Paternostro, A. A. Geraci, P. F. Barker, M. S. Kim, and G. Milburn. Spin entanglement witness for quantum gravity. *Physical Review Letters*, 119(24):240401, 2017.

[28] C. Marletto and V. Vedral. Gravitationally induced entanglement between two massive particles is sufficient evidence of quantum effects in gravity. *Physical Review Letters*, 119(24):240402, 2017.

[29] A. Kuhlicke, A. W. Schell, J. Zoll, and O. Benson. Nitrogen vacancy center fluorescence from a submicron diamond cluster levitated in a linear quadrupole ion trap. *Applied Physics Letters*, 105(7):073101, 2014.

[30] T. Delord, L. Nicolas, L. Schwab, and G. Hétet. Electron spin resonance from nv centers in diamonds levitating in an ion trap. *New Journal of Physics*, 19(3):033031, 2017.

[31] T. Delord, L. Nicolas, M. Bodini, and G. Hétet. Diamonds levitating in a paul trap under vacuum: Measurements of laser-induced heating via nv center thermometry. *Applied Physics Letters*, 111(1):013101, 2017.

[32] H. L. Partner, J. Zoll, A. Kuhlicke, and O. Benson. Printed-circuit-board linear paul trap for manipulating single nano-and microparticles. *Review of Scientific Instruments*, 89(8):083101, 2018.

[33] T. Delord, P. Huillery, L. Nicolas, and G. Hétet. Spin-cooling of the motion of a trapped diamond. *Nature*, 580(7801):56–59, 2020.

[34] B. E. Kane. Levitated spinning graphene flakes in an electric quadrupole ion trap. *Physical Review B*, 82(11):115441, 2010.

[35] P. Nagornykh, J. E. Coppock, and B. E. Kane. Cooling of levitated graphene nanoplatelets in high vacuum. *Applied Physics Letters*, 106(24):244102, 2015.

[36] P. Nagornykh, J. E. Coppock, J. P. J. Murphy, and B. E. Kane. Optical and magnetic measurements of gyroscopically stabilized graphene nanoplatelets levitated in an ion trap. *Physical Review B*, 96(3):035402, 2017.

[37] J. Millen, P. Z. G. Fonseca, T. Mavrogordatos, T. S. Monteiro, and P. F. Barker. Cavity cooling a single charged levitated nanosphere. *Physical Review Letters*, 114(12):123602, 2015.

[38] D. Goldwater, M. Paternostro, and P. F. Barker. Testing wave-function-collapse models using parametric heating of a trapped nanosphere. *Physical Review A*, 94(1):010104, 2016.

[39] N. P. Bullier, A. Pontin, and P. F. Barker. Super-resolution imaging of a low frequency levitated oscillator. *Review of Scientific Instruments*, 90(9):093201, 2019.

[40] N. P. Bullier, A. Pontin, and P. F. Barker. Characterisation of a charged particle levitated nano-oscillator. *Journal of Physics D: Applied Physics*, 53(17):175302, 2020.

[41] A. Pontin, N. P. Bullier, M. Toroš, and P. F. Barker. Ultranarrow-linewidth levitated nano-oscillator for testing dissipative wave-function collapse. *Physical Review Research*, 2(2):023349, 2020.

[42] T. W. Penny, A. Pontin, and P. F Barker. Performance and limits of feedback cooling methods for levitated oscillators: A direct comparison. *Physical Review A*, 104(2):023502, 2021.

[43] D. S. Bykov, P. Mestres, L. Dania, L. Schmöger, and T. E. Northup. Direct loading of nanoparticles under high vacuum into a paul trap for levitodynamical experiments. *Applied Physics Letters*, 115(3):034101, 2019.

[44] L. Dania, D. Bykov, P. Mestres, and T. E. Northup. Manipulating a charged nanoparticle in a paul trap for ion-assisted levitated optomechanics. In *Optical Trapping and Optical Micromanipulation XVI*, volume 11083, pages 205–210. SPIE, 2019.

[45] L. Dania, K. Heidegger, D. S. Bykov, G. Cerchiari, G. Araneda, and T. E. Northup. Position measurement of a levitated nanoparticle via interference with its mirror image. *Physical Review Letters*, 129(1):013601, 2022.

[46] D. S. Bykov, L. Dania, P. Mestres, and T. E. Northup. Laser cooling of secular motion of a nanoparticle levitated in a paul trap for ion-assisted optomechanics. In *Optical Trapping and Optical Micromanipulation XVI*, volume 11083, pages 78–83. SPIE, 2019.

[47] L. Martinetz, K. Hornberger, J. Millen, M. S. Kim, and B. A. Stickler. Quantum electromechanics with levitated nanoparticles. *npj Quantum Information*, 6(1):101, 2020.

[48] W. Paul and H. Steinwedel. Ein neues massenspektrometer ohne magnetfeld. *Zeitschrift für Naturforschung A*, 8(7):448–450, 1953.

[49] R. Blatt, P. Zoller, G. Holzmüller, and I. Siemers. Brownian motion of a parametric oscillator: A model for ion confinement in radio frequency traps. *Zeitschrift für Physik D Atoms, Molecules and Clusters*, 4:121–126, 1986.

[50] D. J. Berkeland, J. D. Miller, J. C. Bergquist, W. M. Itano, and D. J. Wineland. Minimization of ion micromotion in a paul trap. *Journal of Applied Physics*, 83(10):5025–5033, 1998.

[51] F. Diedrich, J. C. Bergquist, W. M. Itano, and D. J. Wineland. Laser cooling to the zero-point energy of motion. *Physical Review Letters*, 62(4):403, 1989.

[52] W. M. Itano, J. C. Bergquist, J. J. Bollinger, and D. J. Wineland. Cooling methods in ion traps. *Physica Scripta*, 1995(T59):106, 1995.

[53] D. G. Cory and T. F. Havel. Ion entanglement in quantum information processing. *Science*, 304(5676):1456–1457, 2004.

[54] I. Georgescu. Trapped ion quantum computing turns 25. *Nature Reviews Physics*, 2(6):278–278, 2020.

[55] T. Li, S. Kheifets, and M. G. Raizen. Millikelvin cooling of an optically trapped microsphere in vacuum. *Nature Physics*, 7(7):527–530, 2011.

[56] F. Monteiro, W. Li, G. Afek, C. Li, M. Mossman, and D. C. Moore. Force and acceleration sensing with optically levitated nanogram masses at microkelvin temperatures. *Physical Review A*, 101(5):053835, 2020.

[57] J. Gieseler, B. Deutsch, R. Quidant, and L. Novotny. Subkelvin parametric feedback cooling of a laser-trapped nanoparticle. *Physical Review Letters*, 109(10):103603, 2012.

[58] V. Jain, F. Tebbenjohanns, and L. Novotny. Microkelvin control of an optically levitated nanoparticle. In *Frontiers in Optics*, pages FF5B–2. Optica Publishing Group, 2016.

[59] F. Tebbenjohanns, M. Frimmer, A. Militaru, V. Jain, and L. Novotny. Cold damping of an optically levitated nanoparticle to microkelvin temperatures. *Physical Review Letters*, 122(22):223601, 2019.

[60] F. Tebbenjohanns, M. Frimmer, V. Jain, D. Windey, and L. Novotny. Motional sideband asymmetry of a nanoparticle optically levitated in free space. *Physical Review Letters*, 124(1):013603, 2020.

[61] L. Magrini, P. Rosenzweig, C. Bach, A. Deutschmann-Olek, S. G. Hofer, S. Hong, N. Kiesel, A. Kugi, and M. Aspelmeyer. Real-time optimal quantum control of mechanical motion at room temperature. *Nature*, 595(7867):373–377, 2021.

[62] J. D. Teufel, T. Donner, D. Li, J. W. Harlow, M. S. Allman, K. Cicak, A. J. Sirois, J. D. Whittaker, K. W. Lehnert, and R. W. Simmonds. Sideband cooling of micromechanical motion to the quantum ground state. *Nature*, 475(7356):359–363, 2011.

[63] P. Z. G. Fonseca, E. B. Aranas, J. Millen, T. S. Monteiro, and P. F. Barker. Nonlinear dynamics and strong cavity cooling of levitated nanoparticles. *Physical Review Letters*, 117(17):173602, 2016.

[64] U. Delić, M. Reisenbauer, D. Grass, N. Kiesel, V. Vuletić, and M. Aspelmeyer. Cavity cooling of a levitated nanosphere by coherent scattering. *Physical Review Letters*, 122(12):123602, 2019.

[65] A. W. Schell, G. P. Conangla, R. A. Rica, and R. Quidant. Levitation and optical interrogation of a feedback-cooled nitrogen vacancy center in a paul trap. In *European Quantum Electronics Conference*, page ea_3_2. Optica Publishing Group, 2019.

[66] G. P. Conangla, A. W. Schell, R. A. Rica, and R. Quidant. Motion control and optical interrogation of a levitating single nitrogen vacancy in vacuum. *Nano Letters*, 18(6):3956–3961, 2018.

[67] Y. Minowa, K. Kato, S. Ueno, T. W. Penny, A. Pontin, M. Ashida, and P. F. Barker. Imaging-based feedback cooling of a levitated nanoparticle. *Review of Scientific Instruments*, 93(7):075109, 2022.

[68] B. D'Urso, B. Odom, and G. Gabrielse. Feedback cooling of a one-electron oscillator. *Physical Review Letters*, 90(4):043001, 2003.

[69] B. D'Urso, R. Van Handel, B. Odom, D. Hanneke, and G. Gabrielse. Single-particle self-excited oscillator. *Physical Review Letters*, 94(11):113002, 2005.

[70] N. Guise, J. DiSciacca, and G. Gabrielse. Self-excitation and feedback cooling of an isolated proton. *Physical Review Letters*, 104(14):143001, 2010.

[71] R. E. March. An introduction to quadrupole ion trap mass spectrometry. *Journal of Mass Spectrometry*, 32(4):351–369, 1997.

[72] M. J Madsen, W. K. Hensinger, D. Stick, J. A. Rabchuk, and C. Monroe. Planar ion trap geometry for microfabrication. *Applied Physics B*, 78:639–651, 2004.

[73] M. D. Summers, D. R. Burnham, and D. McGloin. Trapping solid aerosols with optical tweezers: A comparison between gas and liquid phase optical traps. *Optics Express*, 16(11):7739–7747, 2008.

[74] J. B. Fenn, M. Mann, C. K. Meng, S. F. Wong, and C. M. Whitehouse. Electrospray ionization for mass spectrometry of large biomolecules. *Science*, 246(4926):64–71, 1989.

[75] Y. Cai, W. P. Peng, S. J. Kuo, Y. T. Lee, and H. C. Chang. Single-particle mass spectrometry of polystyrene microspheres and diamond nanocrystals. *Analytical Chemistry*, 74(1):232–238, 2002.

[76] A. Ashkin and J. M. Dziedzic. Optical levitation by radiation pressure. *Applied Physics Letters*, 19(8):283–285, 1971.

[77] Y. Arita, M. Mazilu, and K. Dholakia. Laser-induced rotation and cooling of a trapped microgyroscope in vacuum. *Nature Communications*, 4(1):2374, 2013.

[78] A. Khodaee, K. Dare, A. Johnson, U. Delić, and M. Aspelmeyer. Dry launching of silica nanoparticles in vacuum. *AIP Advances*, 12(12):125023, 2022.

[79] M. Nikkhou, Y. Hu, J. A. Sabin, and J. Millen. Direct and clean loading of nanoparticles into optical traps at millibar pressures. *Photonics*, 8(11):458, 2021.

[80] L. C. Andrews. *Special functions of mathematics for engineers*, volume 49. Spie Press, 1998.

[81] W. Cao, Y. Huang, K. C. Fan, and J. Zhang. A novel machine learning algorithm for large measurement range of quadrant photodetector. *Optik*, 227:165971, 2021.

[82] M. Drewsen and A. Brøner. Harmonic linear paul trap: Stability diagram and effective potentials. *Physical Review A*, 62(4):045401, 2000.

[83] Y. Ren, E. Benedetto, H. Borrill, Y. Savchuk, K. O'Flynn, M. Rashid, J. Millen, et al. Event-based imaging of levitated microparticles. *Applied Physics Letters*, 121(11), 2022.

[84] J. Millen, T. S. Monteiro, R. Pettit, and A. N. Vamivakas. Optomechanics with levitated particles. *Reports on Progress in Physics*, 83(2):026401, 2020.

[85] C. Gonzalez-Ballestero, M. Aspelmeyer, L. Novotny, R. Quidant, and O. Romero-Isart. Levitodynamics: Levitation and control of microscopic objects in vacuum. *Science*, 374(6564):eabg3027, 2021.

[86] J. Millen and B. A. Stickler. Quantum experiments with microscale particles. *Contemporary Physics*, 61(3):155–168, 2020.

[87] J. Millen and J. Gieseler. Single particle thermodynamics with levitated nanoparticles. *Thermodynamics in the Quantum Regime: Fundamental Aspects and New Directions*, pages 853–885, 2018.

[88] M. Rademacher, J. Millen, and Y. L. Li. Quantum sensing with nanoparticles for gravimetry: when bigger is better. *Advanced Optical Technologies*, 9(5):227–239, 2020.

[89] D. C. Moore and A. A. Geraci. Searching for new physics using optically levitated sensors. *Quantum Science and Technology*, 6(1):014008, 2021.

[90] V. Svak, J. Flajšmanová, L. Chvátal, M. Šiler, A. Jonáš, J. Ježek, S. H. Simpson, P. Zemánek, and O. Brzobohatỳ. Stochastic dynamics of optically bound matter levitated in vacuum. *Optica*, 8(2):220–229, 2021.

[91] J. Ahn, Z. Xu, J. Bang, Y. Deng, T. M. Hoang, Q. Han, R. Ma, and T. Li. Optically levitated nanodumbbell torsion balance and ghz nanomechanical rotor. *Physical Review Letters*, 121:033603, 2018.

[92] R. Reimann, M. Doderer, E. Hebestreit, R. Diehl, M. Frimmer, D. Windey, F. Tebbenjohanns, and L. Novotny. Ghz rotation of an optically trapped nanoparticle in vacuum. *Physical Review Letters*, 121:033602, 2018.

[93] S. Kheifets, A. Simha, K. Melin, T. Li, and M. G. Raizen. Observation of brownian motion in liquids at short times: instantaneous velocity and memory loss. *Science*, 343(6178):1493–1496, 2014.

[94] J. Millen, T. Deesuwan, P. Barker, and J. Anders. Nanoscale temperature measurements using non-equilibrium brownian dynamics of a levitated nanosphere. *Nature Nanotechnology*, 9(6):425–429, 2014.

[95] J. Rieser, M. A. Ciampini, H. Rudolph, N. Kiesel, K. Hornberger, B. A. Stickler, M. Aspelmeyer, and U. Delić. Tunable light-induced dipole-dipole interaction between optically levitated nanoparticles. *Science*, 377(6609):987–990, 2022.

[96] G. Afek, D. Carney, and D. C. Moore. Coherent scattering of low mass dark matter from optically trapped sensors. *Physical Review Letters*, 128:101301, 2022.

[97] H. Rudolph, U. Delić, M. Aspelmeyer, K. Hornberger, and B. A. Stickler. Force-gradient sensing and entanglement via feedback cooling of interacting nanoparticles. *Physical Review Letters*, 129(19):193602, 2022.

[98] G. Gallego, T. Delbruck, G. Orchard, C. Bartolozzi, B. Taba, A. Censi, S. Leutenegger, A. J. Davison, J. Conradt, K. Daniilidis, and D. Scaramuzza. Event-based vision: A survey. *IEEE Transactions on Pattern Analysis and Machine Intelligence*, 44(1):154–180, 2022.

[99] Prophesee. Event-based vision whitepaper. https://www.prophesee.ai/whitepaper-download, 2022.

[100] I. A. Martínez, É. Roldán, L. Dinis, and R. A. Rica. Colloidal heat engines: a review. *Soft matter*, 13(1):22–36, 2017.

[101] M. Wei and H. D. Ou-Yang. Thermal and non-thermal fluctuations of the mechanical properties in living cells. In *Optical Trapping and Optical Micromanipulation VII*, volume 7762, page 77621L. International Society for Optics and Photonics, 2010.

[102] I. A. Martinez, É. Roldán, L. Dinis, P. Mestres, J. M. R Parrondo, and R. A. Rica. Stochastic thermodynamics with a brownian particle in an optical trap (presentation recording). In *Optical Trapping and Optical Micromanipulation XII*, volume 9548, page 954816. International Society for Optics and Photonics, 2015.

[103] L. Rondin, J. Gieseler, F. Ricci, R. Quidant, C. Dellago, and L. Novotny. Direct measurement of kramers turnover with a levitated nanoparticle. *Nature Nanotechnology*, 12(12):1130–1133, 2017.

[104] Y. Jun, M. Gavrilov, and J. Bechhoefer. High-precision test of landauer's principle in a feedback trap. *Physical Review Letters*, 113(19):190601, 2014.

[105] T. M. Hoang, R. Pan, J. Ahn, J. Bang, H. T. Quan, and T. Li. Experimental test of the differential fluctuation theorem and a generalized jarzynski equality for arbitrary initial states. *Physical Review Letters*, 120(8):080602, 2018.

[106] S. Kotler, G. A. Peterson, E. Shojaee, F. Lecocq, K. Cicak, A. Kwiatkowski, S. Geller, S. Glancy, E. Knill, R. W. Simmonds, et al. Direct observation of deterministic macroscopic entanglement. *Science*, 372(6542):622–625, 2021.

[107] I. Brandão, D. Tandeitnik, and T. Guerreiro. Coherent scattering-mediated correlations between levitated nanospheres. *Quantum Science and Technology*, 6(4):045013, 2021.

[108] L. Mercier de Lépinay, C. F. Ockeloen-Korppi, M. J. Woolley, and M. A. Sillanpää. Quantum mechanics–free subsystem with mechanical oscillators. *Science*, 372(6542):625–629, 2021.

[109] T. F. Roque and J. A. Roversi. Quantum correlations between two oscillators connected by a time-dependent coupling. In *Latin America Optics and Photonics Conference*, pages LS2B–2. Optical Society of America, 2012.

[110] L. Qi, Y. Xing, S. Liu, S. Zhang, and H. Wang. Topological phase induced by distinguishing parameter regimes in a cavity optomechanical system with multiple mechanical resonators. *Physical Review A*, 101(5):052325, 2020.

[111] D. Carney, G. Krnjaic, D. C. Moore, C. A. Regal, G. Afek, S. Bhave, B. Brubaker, T. Corbitt, J. Cripe, N. Crisosto, et al. Mechanical quantum sensing in the search for dark matter. *Quantum Science and Technology*, 6(2):024002, 2021.

[112] R. Zhao, A. Manjavacas, F. J. G. de Abajo, and J. B. Pendry. Rotational quantum friction. *Physical Review Letters*, 109(12):123604, 2012.

[113] T. W. Penny, A. Pontin, and P. F. Barker. Sympathetic cooling and squeezing of two colevitated nanoparticles. *Physical Review Research*, 5(1):013070, 2023.

[114] Y. Arita, E. M. Wright, and K. Dholakia. Optical binding of two cooled micro-gyroscopes levitated in vacuum. *Optica*, 5(8):910–917, 2018.

[115] B. R. Slezak and B. D'Urso. A microsphere molecule: The interaction of two charged microspheres in a magneto-gravitational trap. *Applied Physics Letters*, 114(24):244102, 2019.

[116] J. Vijayan, Z. Zhang, J. Piotrowski, D. Windey, F. van der Laan, M. Frimmer, and L. Novotny. Scalable all-optical cold damping of levitated nanoparticles. *Nature Nanotechnology*, 18(1):49–54, 2023.

[117] P. Praveen, S. S. Iyengar, S. Bhattacharya, S. Ananthamurthy, et al. Two particle tracking and detection in a single gaussian beam optical trap. *Applied Optics*, 55(3):585–594, 2016.

[118] G. M. Gibson, J. Leach, S. Keen, A. J. Wright, and M. J. Padgett. Measuring the accuracy of particle position and force in optical tweezers using high-speed video microscopy. *Optics Express*, 16(19):14561–14570, 2008.

[119] D. Ott, S. Nader, S. Reihani, and L. B. Oddershede. Simultaneous three-dimensional tracking of individual signals from multi-trap optical tweezers using fast and accurate photodiode detection. *Optics Express*, 22(19):23661–23672, 2014.

[120] Z. Wang, Y. Ng, C. Scheerlinck, and R. Mahony. An asynchronous kalman filter for hybrid event cameras. In *Proceedings of the IEEE/CVF International Conference on Computer Vision*, pages 448–457, 2021.

[121] S. Afshar, A. P. Nicholson, A. Van Schaik, and G. Cohen. Event-based object detection and tracking for space situational awareness. *IEEE Sensors Journal*, 20(24):15117–15132, 2020.

[122] M. Frimmer, K. Luszcz, S. Ferreiro, V. Jain, E. Hebestreit, and L. Novotny. Controlling the net charge on a nanoparticle optically levitated in vacuum. *Physical Review A*, 95(6):061801, 2017.

[123] F. Ricci, M. T. Cuairan, G. P. Conangla, A. W. Schell, and R. Quidant. Accurate mass measurement of a levitated nanomechanical resonator for precision force-sensing. *Nano Letters*, 19(10):6711–6715, 2019.

[124] E. Hebestreit, R. Reimann, M. Frimmer, and L. Novotny. Measuring the internal temperature of a levitated nanoparticle in high vacuum. *Physical Review A*, 97(4):043803, 2018.

[125] I. Alda, J. Berthelot, R. A. Rica, and R. Quidant. Trapping and manipulation of individual nanoparticles in a planar paul trap. *Applied Physics Letters*, 109(16):163105, 2016.

[126] C. C. Rusconi, V. Pöchhacker, K. Kustura, J. I. Cirac, and O. Romero-Isart. Quantum spin stabilized magnetic levitation. *Physical Review Letters*, 119(16):167202, 2017.

[127] B. R. Slezak, C. W. Lewandowski, J. F. Hsu, and B. D'Urso. Cooling the motion of a silica microsphere in a magneto-gravitational trap in ultra-high vacuum. *New Journal of Physics*, 20(6):063028, 2018.

[128] M. C. O'Brien, S. Dunn, J. E. Downes, and J. Twamley. Magneto-mechanical trapping of micro-diamonds at low pressures. *Applied Physics Letters*, 114(5):053103, 2019.

[129] L. Martinetz, K. Hornberger, and B. A. Stickler. Gas-induced friction and diffusion of rigid rotors. *Physical Review E*, 97(5):052112, 2018.

[130] T. Li and M. G. Raizen. Brownian motion at short time scales. *Annalen der Physik*, 525(4):281–295, 2013.

[131] C. Timberlake, M. Toroš, D. Hempston, G. Winstone, M. Rashid, and H. Ulbricht. Static force characterization with fano anti-resonance in levitated optomechanics. *Applied Physics Letters*, 114(2):023104, 2019.

[132] G. Winstone, R. Bennett, M. Rademacher, M. Rashid, S. Buhmann, and H. Ulbricht. Direct measurement of the electrostatic image force of a levitated charged nanoparticle close to a surface. *Physical Review A*, 98(5):053831, 2018.

[133] E. Hebestreit, M. Frimmer, R. Reimann, and L. Novotny. Sensing static forces with free-falling nanoparticles. *Physical Review Letters*, 121(6):063602, 2018.

[134] O. Romero-Isart, A. C. Pflanzer, M. L. Juan, R. Quidant, N. Kiesel, M. Aspelmeyer, and J. I. Cirac. Optically levitating dielectrics in the quantum regime: Theory and protocols. *Physical Review A*, 83(1):013803, 2011.

[135] C. C Rusconi, M. Perdriat, G. Hétet, O. Romero-Isart, and B. A. Stickler. Spin-controlled quantum interference of levitated nanorotors. *Physical Review Letters*, 129(9):093605, 2022.

[136] J. Millen, T. Deesuwan, P. Barker, and J. Anders. Nanoscale temperature measurements using non-equilibrium brownian dynamics of a levitated nanosphere. *Nature Nanotechnology*, 9(6):425–429, 2014.

[137] D. Carney, H. Häffner, D. C. Moore, and J. M. Taylor. Trapped electrons and ions as particle detectors. *Physical Review Letters*, 127(6):061804, 2021.

[138] A. Datta and H. Miao. Signatures of the quantum nature of gravity in the differential motion of two masses. *Quantum Science and Technology*, 6(4):045014, 2021.

[139] B. E. King, C. S. Wood, C. J. Myatt, Q. A. Turchette, D. Leibfried, W. M. Itano, C. Monroe, and D. J. Wineland. Cooling the collective motion of trapped ions to initialize a quantum register. *Physical Review Letters*, 81(7):1525, 1998.

[140] A. Ashkin and J. M. Dziedzic. Optical levitation in high vacuum. *Applied Physics Letters*, 28(6):333–335, 1976.

[141] G. Ranjit, M. Cunningham, K. Casey, and A. A. Geraci. Zeptonewton force sensing with nanospheres in an optical lattice. *Physical Review A*, 93(5):053801, 2016.

[142] D. S. Bykov, L. Dania, F. Goschin, and T. E. Northup. 3d sympathetic cooling and detection of levitated nanoparticles. *Optica*, 10(4):438–442, 2023.

[143] J. Vovrosh, M. Rashid, D. Hempston, J. Bateman, M. Paternostro, and H. Ulbricht. Parametric feedback cooling of levitated optomechanics in a parabolic mirror trap. *JOSA B*, 34(7):1421–1428, 2017.

[144] A. Setter, M. Toroš, J. F. Ralph, and H. Ulbricht. Real-time kalman filter: Cooling of an optically levitated nanoparticle. *Physical Review A*, 97(3):033822, 2018.

[145] J. Gieseler, R. Quidant, C. Dellago, and L. Novotny. Dynamic relaxation of a levitated nanoparticle from a non-equilibrium steady state. *Nature Nanotechnology*, 9(5):358–364, 2014.

[146] B. C. Buchler, M. B. Gray, D. A. Shaddock, T. C. Ralph, and D. E. McClelland. Suppression of classic and quantum radiation pressure noise by electro-optic feedback. *Optics Letters*, 24(4):259–261, 1999.

[147] B. S. Sheard, M. B. Gray, B. J. J. Slagmolen, J. H. Chow, and D. E. McClelland. Experimental demonstration of in-loop intracavity intensity-noise suppression. *IEEE Journal of Quantum Electronics*, 41(3):434–440, 2005.

[148] P. Bushev, D. Rotter, A. Wilson, F. Dubin, C. Becher, J. Eschner, R. Blatt, V. Steixner, P. Rabl, and P. Zoller. Feedback cooling of a single trapped ion. *Physical Review Letters*, 96(4):043003, 2006.

[149] Redpitaya. Stemlab 125-14. https://redpitaya.com/stemlab-125-14/, 2023.

[150] A. K. Chauhan, O. Černotík, and R. Filip. Stationary gaussian entanglement between levitated nanoparticles. *New Journal of Physics*, 22(12):123021, 2020.

[151] D. Wineland, P. Ekstrom, and H. Dehmelt. Monoelectron oscillator. *Physical Review Letters*, 31(21):1279, 1973.

[152] H. Dehmelt, W. Nagourney, and J. Sandberg. Self-excited mono-ion oscillator. *Proceedings of the National Academy of Sciences*, 83(16):5761–5763, 1986.

[153] M. Brownnutt, G. Wilpers, P. Gill, R. C. Thompson, and A. G. Sinclair. Monolithic microfabricated ion trap chip design for scaleable quantum processors. *New Journal of Physics*, 8(10):232, 2006.

[154] G. Wilpers, P. See, P. Gill, and A. G. Sinclair. A monolithic array of three-dimensional ion traps fabricated with conventional semiconductor technology. *Nature Nanotechnology*, 7(9):572–576, 2012.

[155] K. Choonee, G. Wilpers, and A. G. Sinclair. Silicon microfabricated linear segmented ion traps for quantum technologies. In *2017 19th International Conference on Solid-State Sensors, Actuators and Microsystems (TRANSDUCERS)*, pages 615–618. IEEE, 2017.

Appendix A

Code of SIMION simulation

Simulation code for Macro-Paul trap

Code of generating trap structure

In SIMION environment, a geometry file (GEM) is used to define electrode geometries using unions and intersections of some basic shapes like a cylinder, a cuboid. Here is the .GEM file to generate the shapes of Macro-Paul trap in Figure 2.1.

```
pa_define(501,301,301,planar,none,e,, 0.05)
;x:500 grid*0.05 mm/grid=25mm
;y:300 grid*0.05 mm/grid=15mm
;z:300 grid*0.05 mm/grid=15mm

locate(23,7,3, 1, 90,45) {
    electrode(1) { fill {
    within      { cylinder(0,0,1, 1.5,1.5, 21) } }}

    electrode(2) { fill {
    within      { cylinder(0,7,1, 1.5,1.5, 21) } }}

    electrode(3) { fill {
    within      { cylinder(-7,0,1, 1.5,1.5, 21) }}}

    electrode(4) { fill {
    within      { cylinder(-7,7,1, 1.5,1.5, 21) }}}

    electrode(5) { fill {
    within      { cylinder(-3.5,3.5,1, 0.5,0.5, 10) }}}
```

```
    electrode(6) { fill {
    within      { cylinder(-3.5,3.5,-10, 0.5,0.5, 10) }}}

    electrode(7) { fill {
    within      { cylinder(-3.5,3.5,1, 2.5,2.5, 3) }
    notin_inside { cylinder(-3.5,3.5,1e6, 2,2, 2e6) }}}

    electrode(8) { fill {
    within      { cylinder(-3.5,3.5,-17, 2.5,2.5, 3) }
    notin_inside { cylinder(-3.5,3.5,1e6, 2,2, 2e6) }}} }

locate(23,7,7.95, 1, 90,45) {
    electrode(9) { fill {
    within      { revolve_zx(360){
   polyline(-17,2.5
   -17,2
   -12,1
   -12,1.5) }}}}

    electrode(10) { fill {
    within      { revolve_zx(360){
   polyline(-7,1.5
   -7,1
   -2,2
   -2,2.5) }}}} }
```

Code of setting trap voltages

Lua is a main programming language embedded in SIMION to set specific voltages to the electrodes of trap. Here is the .lua file to give the AC and DC voltages to the electrodes in Macro-Paul trap.

```
simion.workbench_program()

adjustable pe_update_each_usec  = 0.05  -- potential energy display
                                        -- update period (microsec)
                                        -- (for display purposes only)
```

```
local omega     -- frequency_hz (reexpressed in units of radians/usec)
local theta     -- phase_angle_deg (reexpressed in units of radians)
local last_pe_update = 0.0 -- last potential energy surface update time
    (usec)

function segment.fast_adjust()

      adjustable dcvolts=0
      adjustable rfvolts=750
      adjustable freqency_hz=1200
        theta = 0
        omega = freqency_hz * 2 * 3.14159 * 1E-6 -- frequency (rad/usec)

    -- Finally, apply adjustable voltages to rod electrodes.
    adj_elect01 = 0
    adj_elect02 = dcvolts + rfvolts * sin(theta + ion_time_of_flight *
        omega)
   adj_elect03 = dcvolts + rfvolts * sin(theta + ion_time_of_flight *
       omega)
   adj_elect04 = 0
   adj_elect05 = -4+0.5
   adj_elect06 = -4

end

--This is used to examine ion parameters after each time step
function segment.other_actions()
  -- Update potential energy surface display periodically.
  -- The performance overhead of this in non-PE views is only a few
      percent.
  -- NOTE: the value inside abs(...) can be negative when a new ion is
      flown.
  if abs(ion_time_of_flight - last_pe_update) >= pe_update_each_usec then
    last_pe_update = ion_time_of_flight
    sim_update_pe_surface = 1 -- Request a PE surface display update.
  end
end

-- SIMION segment called by SIMION to override time-step size on each
    time-step.
```

```
function segment.tstep_adjust()
-- Keep time step <= 0.1 usec.
    if ion_time_step > 0.1 then ion_time_step = 0.1 end
end

function line_potentials(x1,y1,z1, x2,y2,z2, n)
   local x1=13.5
   local y1=7
   local z1=7.75
   local n=8

   for j=0,n do

    local x,y,z = x1, y1, z1+0.05*j
    local v = simion.wb:epotential(x,y,z)
    local ex,ey,ez = simion.wb:efield(x,y,z)
    print(j+1, x,y,z, v)

  end
end
line_potentials()
```

Simulation code for Micro-Paul trap

Code of generating trap structure

Similar to the code for Macro-Paul trap, the .GEM file in Micro-Paul trap shown in Figure 2.5 is illustrated below.

```
pa_define(301,201,201,planar,none,e,, 0.05)
;x:300 grid*0.05 mm/grid=15mm
;y:200 grid*0.05 mm/grid=10mm
;z:200 grid*0.05 mm/grid=10mm
;locate(13,1.5,1, 1, 90,0)
locate(13,4.5,2, 1, 90,45)
; locate($(x0),$(y0),$(z0), 1, 90)
  {electrode(1) { fill {
    within      { cylinder(0,0,0.8, 0.5,0.5, 10) }
   ;cylinder radius: 0.5mm, length: 10mm }}
```

```
  electrode(2) { fill {
    within      { cylinder(0,2.3,0.8, 0.5,0.5, 10) }}}

  electrode(3) { fill {
    within      { cylinder(-2.3,0,0.8, 0.5,0.5, 10) }}}

    electrode(4) { fill {
    within      { cylinder(-2.3,2.3,0.8, 0.5,0.5, 10) }}}

   electrode(5) { fill {
    within      { cylinder(-1.15,1.15,0.8, 0.15,0.15, 4.6) }}}

   electrode(6) { fill {
    within      { cylinder(-1.15,1.15,-4.6, 0.15,0.15, 4.6) }}}

   ;z axis of electrodes 1-5 is decided by the endcap rod distance
   ;z axis of electrode 6 is decided by -(10-endcap_distance)/2
   ;the length of electrode 5 and 6 is (10-endcap_distance)/2
}
```

Code of setting trap voltages

The .lua file to set related voltages to the electrodes in Micro-Paul trap is expressed as below.

```
simion.workbench_program()

-- Variables adjustable during flight:

adjustable pe_update_each_usec   = 0.05  -- potential energy display
                                         -- update period (microsec)
                                         -- (for display purposes only)

local omega     -- frequency_hz (reexpressed in units of radians/usec)
local theta     -- phase_angle_deg (reexpressed in units of radians)
local last_pe_update = 0.0 -- last potential energy surface update time
    (usec)
```

```
function segment.fast_adjust()

    adjustable dcvolts=0
    adjustable rfvolts=400
    adjustable freqency_hz=1230
    adjustable endcap_volts=-12.0;
    theta = 0
    omega = freqency_hz * 2 * 3.14159 * 1E-6 -- frequency (rad/usec)

    -- Finally, apply adjustable voltages to rod electrodes.
    adj_elect01 = 0
    adj_elect02 = dcvolts + rfvolts * sin(theta + ion_time_of_flight *
        omega)
    adj_elect03 = dcvolts + rfvolts * sin(theta + ion_time_of_flight *
        omega)
    adj_elect04 = 0
    adj_elect05 = endcap_volts
    adj_elect06 = endcap_volts

end

--This is used to examine ion parameters after each time step
function segment.other_actions()
  -- Update potential energy surface display periodically.
  -- The performance overhead of this in non-PE views is only a few
      percent.
  -- NOTE: the value inside abs(...) can be negative when a new ion is
      flown.
  if abs(ion_time_of_flight - last_pe_update) >= pe_update_each_usec then
    last_pe_update = ion_time_of_flight
    sim_update_pe_surface = 1 -- Request a PE surface display update.
  end
end

-- SIMION segment called by SIMION to override time-step size on each
    time-step.
function segment.tstep_adjust()
-- Keep time step <= 0.1 usec.
    if ion_time_step > 0.1 then ion_time_step = 0.1 end
end
```

```
function line_potentials(x1,y1,z1, x2,y2,z2, n)
   local x1=8.8
   local y1=4.5
   local z1=3.65
   local n=120

   for j=0,n do

    local x,y,z = x1, y1, z1-n/2*0.05+0.05*j
    local v = simion.wb:epotential(x,y,z)
    local ex,ey,ez = simion.wb:efield(x,y,z)
    print(j+1, x,y,z, v)
  end
end

line_potentials()
```

Appendix B

Drawing of trap holder

Figure B.1 illustrates the detailed dimensions of designed trap holder and all the labelled sizes are with mm unit.

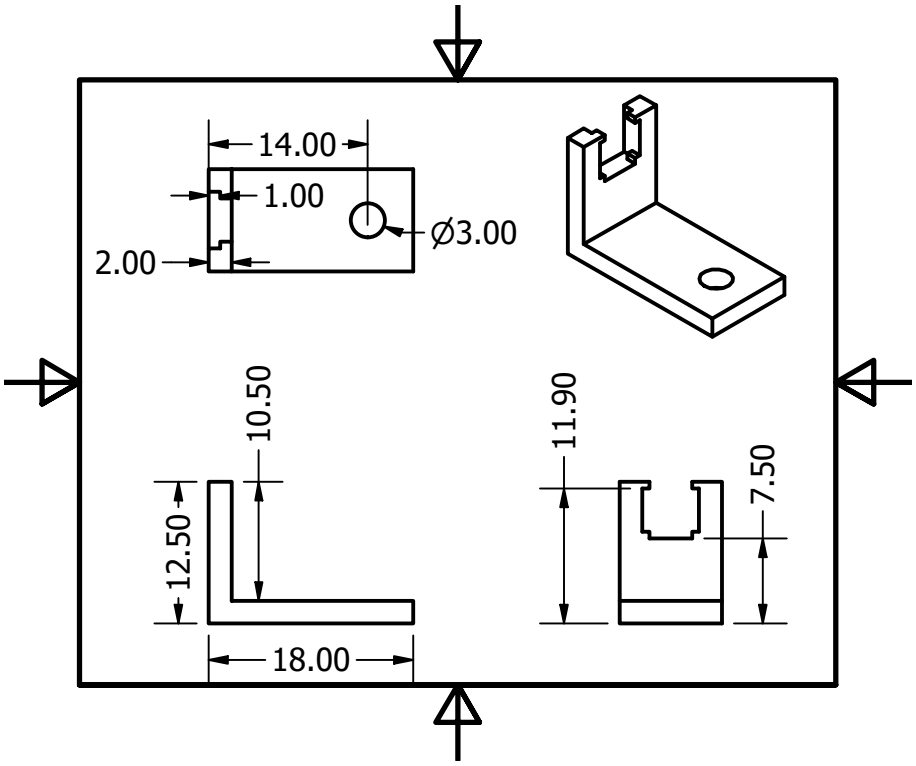

Fig. B.1 The drawing of trap holder. All the dimensions in this image are with mm unit.

Appendix C

Drawing of piece and piece holder

Figure C.1 illustrates the detailed dimensions of trap pieces and piece holders and all the labelled sizes are with mm unit.

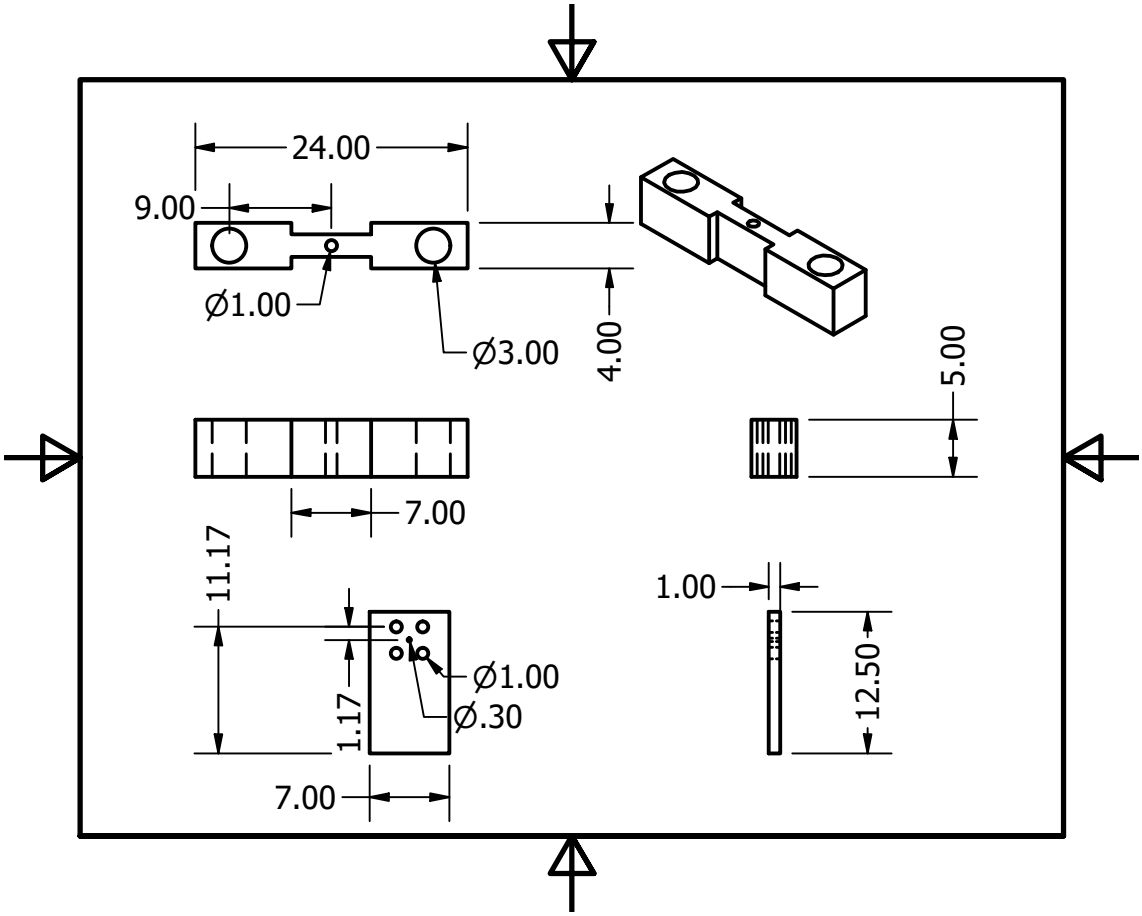

Fig. C.1 The drawing of the trap with large endcap separation. The trap is comprised of ceramic pieces and piece holders. The first two rows show the dimensions of the piece holders and the third row shows the dimension of the designed pieces. All of the labelled sizes are with mm unit.